On the dynamics of the Atlantic meridional overturning circulation in idealized models forced by differential heating and winds

by

Fabian Schloesser

A DISSERTATION SUBMITTED TO THE GRADUATE DIVISION OF THE UNIVERSITY OF HAWAI'I AT MĀNOA IN PARTIAL FULFILLMENT OF THE REQUIREMENTS FOR THE DEGREE OF DOCTOR OF PHILOSOPHY

IN

OCEANOGRAPHY

December 2011

Thesis Committee:

Axel Timmermann, Chairperson

Julian P. McCreary

Peter Müller

Eric Firing

Fei-Fei Jin

For Lanikai

Acknowledgements

I am grateful to my caring advisors Axel Timmermann and Jay McCreary, who guided me through my dissertation project. Furthermore, I benefitted from discussions with Ryo Furue, Peter Müller, Eric Firing and Fei-Fei Jin. Financial support was provided by the International Pacific Research Center at the University of Hawai‘i and the National Science Foundation.

Abstract

Historically, ocean models and solutions of different complexity have been developed to investigate the dynamics of basin-scale, deep, meridional overturning circulations (MOCs). In this study, we develop a three-dimensional theory for the descending branch of the MOC in solutions near the bottom of the hierarchy, forced only by a surface buoyancy flux and a zonal wind stress.

Our theory is based on analytical solutions for a variable-density, layer ocean model (VLOM). The results are validated by comparing the VLOM solutions to numerical solutions to an ocean general circulation model (MITgcm).

Key processes that determine the strength and structure of the model MOC are the following. The eastern-boundary upper-layer thickness is determined by a no-flow condition normal to the boundary, which implies a poleward deepening of the thermocline in response to the meridional surface density gradient. The baroclinic Rossby-wave speed in VLOM illustrates how the large-scale surface density gradient affects the propagation of Rossby waves, which adjust the interior-ocean layer thickness. In a narrow, northern region, the upper layer with a vertically uniform temperature is very thick, and Rossby waves are damped by mixing processes, which tend to restratify the water column.

In solutions without winds, the Rossby-wave damping is the main mechanism to generate a northward convergence of upper-layer flow, and to establish the sinking branch of the MOC. In solutions with winds, water also detrains in the interior subpolar gyre, as it is cooled on its way north, and is finally reaches the deep-ocean temperature.

We derive analytical expressions for MOC transports in VLOM that depend on the tropical thermocline depth, the meridional density gradient, the strength of the mixing and the wind forcing. These results recover and provide dynamical explanations for scaling laws that relate the strength of the MOC to the meridional pressure difference.

Acknowledgements v

Abstract vii

CHAPTER 1: Introduction 1

1.1 Background 2

1.1.1 Hierarchy of models and solutions 2

1.1.2 Box models 4

1.1.3 Zonally-averaged models 4

1.1.4 Three-dimensional models for the Thermohaline circulation 5

1.1.5 Idealized models forced by buoyancy flux and winds 9

1.2 Present research 12

CHAPTER 2: Models 17

2.1 Experimental design 17

2.1.1 Basin, boundary conditions, and density 17

2.1.2 Forcing 17

2.1.3 Initial states, spin up, and loss of stratification 20

2.2 VLOM 20

2.2.1 General variable-density, 2-layer model 20

2.2.2 Barotropic response 22

2.2.3 Equations for the baroclinic response 23

2.2.4 Across-interface velocities 25

2.2.5 Depth-dependent circulation 26

2.2.6 Baroclinic Rossby waves 27

2.3 MITgcm 29

2.3.1 Overview 29

2.3.2 Definitions of layer-thicknesses 30
2.3.3 Derivation and properties of the pressure function P_1 31

CHAPTER 3: VLOM solutions forced by differential heating 34

3.1 Equations of motion 34
3.2 Solution without overturning 35
3.2.1 Spin up 35
3.2.2 Steady state 41
3.2.3 Conclusions 41
3.3 Solutions with overturning 41
3.3.1 Spin up 41
3.3.2 Steady state 42
3.3.3 Comparison to similar solutions 46
3.4 Thermal-wind circulation 47
3.5 Overturning strength 48
3.5.1 Overturning transport, $\mathcal{M}_n$ 49
3.5.2 Limitations of the results 49

CHAPTER 4: MITgcm solutions forced by differential heating 52

4.1 Conceptual response without overturning 52
4.1.1 Thermocline adjustment and interior-ocean, steady-state response . . 53
4.1.2 Meridional boundary layers 54
4.1.3 Zonal boundary layers 57
4.2 Solutions with overturning 61
4.2.1 Spin-up 61
4.2.2 Steady-state solution 62
4.3 Northern boundary layer 69
4.3.1 Overview 69
4.3.2 Outer layer 70
4.3.3 Inner layer 71

4.3.4 Conclusions 72
4.4 Overturning strength 73
4.4.1 Definitions of $\mathcal{M}_n$ 73
4.4.2 Relation of $\mathcal{M}_n$ to H_s, $h_{\max}$ and previous MOC scalings 73

CHAPTER 5: VLOM solutions driven by differential heating and winds 77

5.1 Equations 77
5.2 Solution without mixing by w_d 79
5.2.1 Spin up 79
5.2.2 Steady-state response 82
5.3 Solution with mixing by w_d 94
5.4 Three-dimensional circulation 97
5.5 Overturning strength 98

CHAPTER 6: MITgcm solutions driven by differential heating and winds 106

6.1 Solution 106
6.1.1 Barotropic circulation 106
6.1.2 Eastern boundary 107
6.1.3 Interior ocean 108
6.1.4 Western boundary layer 112
6.1.5 Overturning circulation 113
6.2 Overturning strength 113

CHAPTER 7: VLOM solutions with an MOC closed by physical entrainment processes 117

7.1 The model 117
7.2 Solutions 120
7.3 Conclusions 124

CHAPTER 8: Summary and conclusions 126

8.1 Summary and discussion 126

8.2 Conclusions and outlook 136

Figure Page

1 Schematic illustration of the global overturning circulation. 2

2 Map of the North Atlantic overturning circulation. 3

3 Model domain and forcing. 19

4 Three-dimensional illustration of the VLOM spin-up in solutions without mixing and winds. 36

5 Zonal Rossby-wave speed in VLOM without wind forcing. 38

6 Three-dimensional illustration of the VLOM spin-up in solutions with mixing and without winds. 43

7 Map of upper layer thickness and transports in a VLOM solution without winds. 44

8 The three-dimensional velocity field in VLOM solutions without mixing and wind forcing. 48

9 Overturning transports as a function of tropical thermocline depth in solutions without winds. 50

10 Velocity field in a meridional Ekman layer. 55

11 Velocity field in a zonal Ekman layer. 58

12 Meridional sections of temperature and velocities in MITgcm solutions without wind forcing. 64

Figure Page

13 Zonal sections of temperature and meridional velocity in MITgcm solutions without wind forcing. 65

14 Map of upper layer thickness in MITgcm in a solution without wind forcing. . . 67

15 Meridional overturning streamfunctions in a MITgcm solution without wind forcing. 68

16 Schematic of the northern boundary layer in the MITgcm. 70

17 Mixing depth $h_{\max}$ in the MITgcm for the experiments with $\tau_o = 0$. 74

18 Map of h_1 and surface velocities in a MITgcm solutino with $H_s = 499\,\mathrm{m}$ and $\tau^x = 0$. 76

19 Barotropic Streamfunction in a VLOM solution with $\tau_o = 0.12\,\mathrm{N/m^2}$. 78

20 Rossby-wave characteristics in a VLOM solution with wind forcing. 81

21 Maps of layer thickness and transports in a VLOM solution with wind forcing. . 83

22 Latitudinal profiles of western-boundary-current transports. 93

23 Schematic of the boundaries of northern boundary layers in VLOM. 95

24 Meridional sections of three-dimensional velocities in a VLOM solution with wind forcing. 98

25 Overturning transports in VLOM as functions of tropical thermocline depth and the strength of the winds. 100

26 Deep-water formation rate and export from the subpolar ocean as a function of H_s and τ_o. 102

27 The barotropic streamfunction in an MITgcm solution with wind forcing. 107

Figure Page

28 Meridional sections of temperature and velocities in an MITgcm solution with wind forcing. 109

29 Zonal sections of temperature and meridional velocities in an MITgcm solution with winds. 110

30 Map of upper-layer thickness in an MITgcm solution with wind forcing. 112

31 Meridional overturning streamfunctions in an MITgcm solution with wind forcing. 114

32 Schematic illustration of the original Gnanadesikan model and the modified version used in this manuscript. 118

33 Transports of the MOC branches and tropical thermocline depth as function of τ_o in box-model solutions. 121

34 Schematics of the circulation in 2-layer model solutions focussing on the descending branch of the MOC. 137

CHAPTER 1

Introduction

The Atlantic Meridional Overturning Circulation (AMOC) is part of the global overturning circulation, also called the global conveyor belt (Figure 1). In the surface branch, where water is in relatively close contact with the atmosphere, cold and dense water masses are formed at high latitudes in currents that flow into regions with strong heat loss from the ocean to the atmosphere. Subsequently, the water sinks and joins the subsurface branch providing the cold and dense water that fills all deep ocean basins. Below the thermocline, which separates the two branches, water is shielded from the direct influence of the atmospheric forcing, and its properties are modified only slowly by mixing processes, until it finally crosses the thermocline to rejoin the surface branch. In the northern hemisphere, deep water formation occurs primarily in the Labrador Sea and the Nordic Seas (Figure 2), which motivates the special interest in the AMOC.

The conveyor belt and its North Atlantic branch are also key elements in the global climate system, as they provide one of the primary pathways by which the ocean transports heat poleward. The maximum heat transport in the North Atlantic, which is mostly associated with the AMOC, is about 1.2 $\pm$ 0.3 PW (Hall and Bryden, 1982; Ganachaud and Wunsch, 2000; Trenberth and Caron, 2001). Climate-proxy data and modeling studies link changes in the AMOC to rapid transitions and climate change in the past (*e.g.,* Okazaki et al., 2010, and references therein).

Given the importance of the AMOC, many observational and theoretical studies have been undertaken to estimate its strength and structure and to understand its underlying

dynamics. Despite this effort, the understanding of the processes that drive the AMOC is still incomplete. One reason for this lack is certainly the sheer complexity of the problem: Although buoyancy forcing is an essential ingredient in order to generate a meridional overturning circulation (MOC), the AMOC is also known to be influenced by winds, basin geometry, bottom topography, and small-scale processes (*e.g.*, Vallis, 2006; Spall and Pickart, 2001; Nakano and Suginohara, 2002).

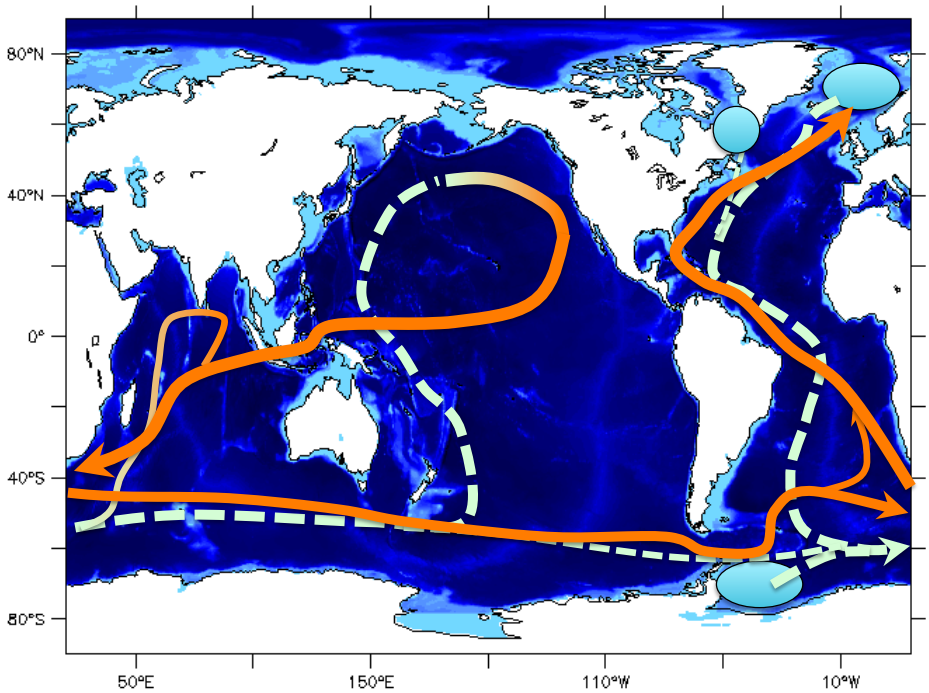

Figure 1: Schematic illustration of the global circulation system with its surface (orange curves) and subsurface branch (dashed curves). Cyan, oval shapes indicate regions where deep-water formation occurs. (This figure was kindly provided by Axel Timmermann.)

1.1 Background

1.1.1 Hierarchy of models and solutions: Given this complexity, developing hierarchies of solutions and models for the AMOC has emerged as a useful approach. The hierarchy of solutions begins with the dynamically simplest case of the so called thermohaline circulation (THC), which corresponds to the circulation that develops in models driven by buoyancy forcing only. In more complex solutions, other processes like wind forcing

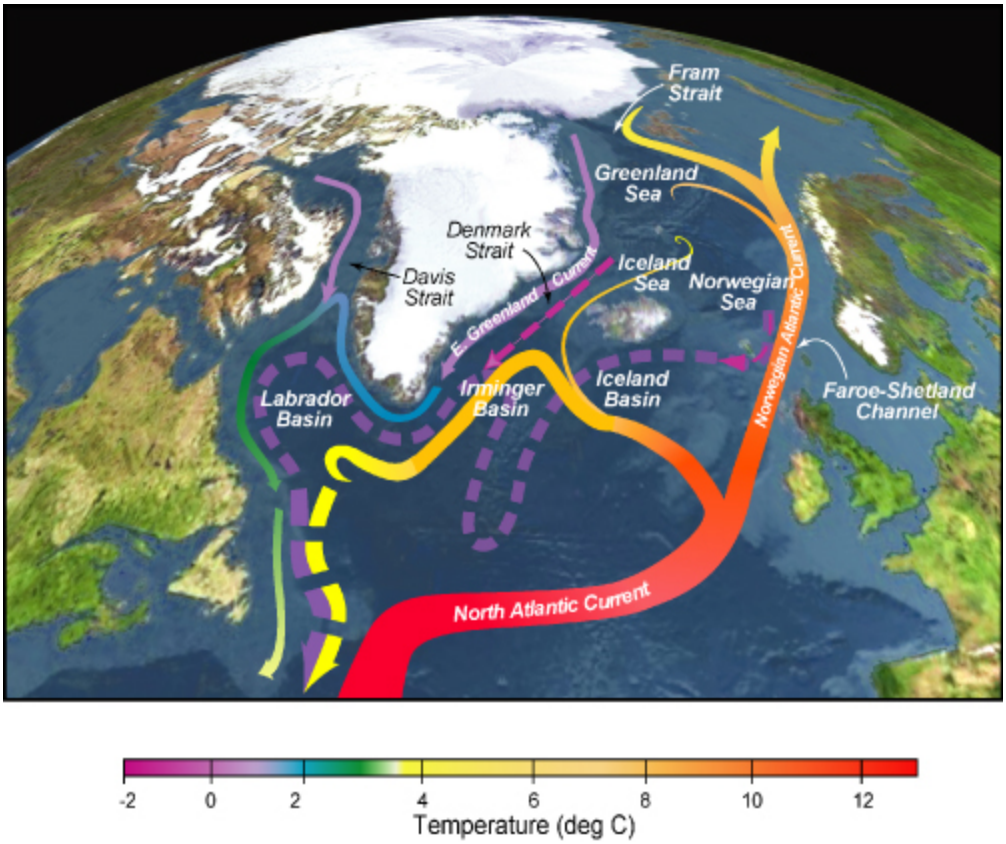

Figure 2: Map of the subpolar North Atlantic and the Nordic Seas and schematic of the surface (solid curves) and subsurface branch (dashed curves) of the AMOC in these areas. Figure from Curry and Mauritzen (2005).

and topography are added in an orderly manner. Models for the AMOC vary in dynamical sophistication from simple box models (*e.g.*, Stommel, 1961; Rooth, 1982; Welander, 1986; Rahmstorf, 1996; Scott et al., 1999; Gnanadesikan, 1999) to two-dimensional, zonally-averaged models (*e.g.*, Marotzke et al., 1988; Wright and Stocker, 1991; Wright et al., 1995, 1998) to intermediate systems (*e.g.*, Stommel and Arons, 1960; Luyten and Stommel, 1986; Kawase, 1987; Huang and Flierl, 1987; Pedlosky and Spall, 2005) to state-of-the-art, ocean general circulation models (OGCMs) (*e.g.*, Bryan and Cox, 1967; Bryan, 1987; Colin de Verdière, 1988; Suginohara and Aoki, 1991; Winton, 1996; Marotzke, 1997; Park and Bryan, 2000). It has proven invaluable to contrast these solutions and models, the simpler ones often providing the dynamical "language" needed to discuss and understand the more complex or

even realistic ones (Held, 2005).

Reviewing the full hierarchy of models and solutions for the AMOC is beyond the scope of this introduction, but a brief summary of studies and concepts that have been particularly influential on the research presented within this manuscript is given below. A more extensive discussions of AMOC literature can be found in review papers, *e.g.,* in Kuhlbrodt et al. (2007).

1.1.2 Box models: Box models are based on conservation equations for energy, mass and/or tracers in two or more homogenous reservoirs. The model introduced by Stommel (1961) consists of two boxes, one representing the Equatorial and the other one the North Atlantic. The average temperature and salinity in each reservoir is forced by a freshwater flux and temperature relaxation, and in steady state, these fluxes are balanced by advection of the model MOC. The MOC transport in this model is frictionally controlled, so that the meridional transport depends on the (meridional) density difference between the two reservoirs. Although being dynamically limited, this model has been very influential on many following studies, especially its property to allow for multiple equilibria. The model was also enhanced in subsequent studies, *e.g.,* by Rooth (1982) and Welander (1986) by adding a third box representing the southern ocean.

Another type of box model, described in Gnanadesikan (1999), is based on scaling laws in OGCMs. In that model, various transports between a reservoir above the thermocline at lower latitudes and a second reservoir, which includes the ocean below the thermocline and at high latitudes, are related to the thermocline thickness H_s. Density remains constant in each reservoir, and the model adjusts H_s to balance the mass transports $\mathcal{V}_n \propto H_s^2$ in the North Atlantic, $\mathcal{V}_s$ in the southern ocean, and $\mathcal{W}_{mix} \propto H_s^{-1}$ across the bottom of the thermocline in an equilibrium state. A schematic and equations for that model are shown in Chapter 7. While the Stommel kind of box model focuses on the role of buoyancy forcing in constraining the MOC, the Gnanadesikan type of model describes the relation of the AMOC and the thermocline depth.

1.1.3 Zonally-averaged models: Two-dimensional models to study the MOC have

been developed by averaging the three-dimensional equations of motions zonally across the ocean basin. In contrast to the box models, the zonally averaged models can resolve the spatial structure of a MOC streamfunction in the y-z plane, but are much less computationally expensive than three-dimensional circulation models. The latter has been especially important for long-term (*e.g.*, paleo) climate simulations, although the need for such models was reduced with the increase of computational capacities in recent years. A main problem of zonally-averaged models is that the zonally-averaged momentum equations depend on the pressure difference at the eastern and western boundaries, which cannot directly be determined from the averaged variables, and hence require a closure. In the closure proposed by Marotzke et al. (1988) the Coriolis term is simply ignored in the meridional momentum equation, which eliminates the zonal momentum balance (and hence the need for parameterizing the zonal pressure difference) from the model. As a result, meridional transports are balanced by friction and proportional to the meridional pressure gradient as in the Stommel (1961) model. In contrast, the meridional flow is assumed to be geostrophic in the model of Wright and Stocker (1991). As the zonal pressure difference is assumed to be proportional to the meridional pressure gradient, however, that closure gives essentially the same result. Wright et al. (1995) separated the domain into an inviscid interior ocean and a frictional, western boundary layer and then found a closure based on vorticity dynamics. This approach is dynamically more appealing then the previous ones, as the pressure terms are eliminated in the vorticity equation, so that a parameterization of the zonal pressures difference is not required. On the other hand, this model crucially depends on an externally-specified, meridional transport at a reference latitude, which essentially requires the strength of the MOC to be known there.

1.1.4 Three-dimensional models for the Thermohaline circulation: The Thermohaline circulation (THC) in a rectangular basin without topography and forced only by a surface buoyancy flux, $Q(y)$, which increases surface density poleward, has been explored in numerous OGCM studies (*e.g.*, Bryan, 1987; Colin de Verdière, 1988; Suginohara and Aoki, 1991; Marotzke, 1997; Sumata and Kubokawa, 2001). Indeed, much of the understanding of the dynamics at work in more complex AMOC solutions is inferred from processes present

in this simpler solution at the bottom of the hierarchy.

In such solutions, the upper-ocean circulation consists of eastward, geostrophic flow across the basin in the latitude band of the surface density gradient, a northward, western-boundary current that supplies most of the water for the eastward flow, and a basin-scale anticyclonic gyre. The deep-ocean circulation mirrors that in the upper ocean, a consequence of the lack of wind forcing and, hence, a barotropic response. The two flow fields are joined by sinking in the northeastern corner of the basin and by upwelling in the interior ocean and along the western boundary, forming a closed, meridional overturning circulation (MOC). Another noteworthy aspect is that the thermocline deepens poleward in the latitude band of the forcing across much of the basin.

Despite its relative simplicity, some aspects of the THC still remain unresolved. On the other hand, solutions to related, dynamically simpler systems have provided insights into various aspects.

To model the deep circulation, Stommel and Arons (1960) considered a subsurface layer forced by an externally prescribed mass source in the northwestern corner of the basin and a compensating sink due to a spatially uniform upwelling of deep water into the upper layer, and the resulting flow had a deep cyclonic circulation like that in the OGCM solutions, with the deep meridional transports given by the Sverdrup relation $\beta V = -fw$. Kawase (1987) extended the Stommel and Arons (1960) model, replacing their uniform upwelling with Newtonian cooling, $w = -\gamma\,(h_2 - H_2)$, a representation of internal diffusion that relaxes the layer thickness h_2 back to its initial state H_2 with a time scale γ^{-1}. The steady-state response differed markedly depending on γ: For weak γ, the flow field resembled that of Stommel and Arons (1960), whereas for sufficiently large γ the upwelling all occurred in a western-boundary current and there was no interior flow. Kawase (1987) and Johnson and Marshall (2002, 2004) also discussed the time-dependent response to a switched-on mass source in the north-western corner of the basin: When the model is started, Kelvin waves quickly radiate southwards along the western boundary, adjusting the coastal layer thickness until the western-boundary-current transport balances the mass source. At the equator, the signal crosses the basin to the east, whereupon Kelvin waves propagate polewards and adjust the eastern-boundary layer thickness on both sides of the equator. In addition, slower,

westward propagating Rossby-waves are emitted from the eastern boundary, which adjust the interior ocean layer thickness for the Sverdrup relation to hold. When Rossby or Kelvin waves arrive at the western boundary, the latter by propagating along the poleward boundary of the basin, they alter the flow into the western boundary layer and trigger a new cycle of wave response. These adjustments continue until the circulation is closed in a steady state. The two different states for large and small γ described above are consistent with these adjustments, as a sufficiently large γ strongly damps western-boundary Kelvin waves before they reach the equator, whereas a small γ primarily damps slower Rossby waves.

To model the surface circulation, Pedlosky and Spall (2005) used a 2-layer model in which buoyancy forcing had the form $-\gamma\,(h_1 - h_1^*)$, which relaxes layer-thickness h_1 to a prescribed thickness $h_1^*(y)$ with a background value H_1 in the tropics and that thins poleward. Similar to the THC in OGCMs, the steady-state response has an eastward surface flow across the basin in the latitude band where $h_{1y}^* < 0$. Along the eastern boundary, Kelvin-wave adjustments act to keep h_1 close to H_1. Rossby waves attempt to carry the coastal value westward but are damped by the buoyancy forcing, thereby detraining water into the deep ocean and providing the downwelling branch of the model MOC. A strength of this solution is that it focuses attention on the importance of dynamical processes (Kelvin-wave adjustments and Rossby-wave damping) in establishing the zonal pressure gradient that drives the northward surface branch of the MOC. Limitations are the poleward thinning of h_1 in contrast to the marked deepening of the thermocline in OGCM solutions, and that it is not clear to what processes their buoyancy forcing (damping) corresponds in the real ocean or OGCMs.

As Rossby waves propagate the eastern-boundary density structure into the interior ocean (*e.g.,* Marotzke, 1997), its dynamical importance has been recognized, and it has been explored in several OGCM studies. Since the eastward thermal-wind shear associated with the poleward, surface-density gradient converges at the eastern boundary, water sinks and hence deepens the thermocline towards the north (Winton, 1996; Ru, 2000; Sumata and Kubokawa, 2001). Sumata and Kubokawa (2001) found that the bottom of a homogenous mixed layer deepens poleward along the eastern boundary via Kelvin-wave adjustments so that the depth-integrated, zonal, thermal wind vanishes within that layer. The eastern-boundary sinking occurs in narrow, viscous boundary layers (Winton, 1996). Park (2006)

explored how the meridional flow within these boundary layers depends on resolution and viscosity, and found that the strength of the flow proportional to resolution and inversely proportional to viscosity. Cessi and Wolfe (2009) investigated the eastern-boundary density structure in eddy-resolving models, and suggested that vertical density advection is balanced by zonal eddy fluxes of buoyancy in an eastern boundary layer in these models.

The overturning transport in the OGCM solutions, typically measured by the maximum of the overturning streamfunction $\psi(y, z)$, is generally in good agreement with scaling arguments. These arguments predict that the overturning transport $\mathcal{M}$ depends on the vertical-diffusion[1] coefficient κ and the meridional density difference $\Delta\rho$ like $\mathcal{M} \sim \kappa^{2/3}\Delta\rho^{1/3}$ (*e.g.*, Robinson and Stommel, 1959; Bryan, 1987; Marotzke, 1997; Park and Bryan, 2000; Vallis, 2006). The arguments are based on a scaling for diffusive upwelling $\mathcal{W}_{mix}$ and one for a meridional transport $\mathcal{V}$, and that $\mathcal{W}_{mix} = \mathcal{V} = \mathcal{M}$ in steady state. To obtain the scaling for $\mathcal{W}_{mix}$, the temperature equation is reduced to the balance of vertical diffusion and advection. Assuming that the thermocline thickness H_s is the relevant depth scale for these terms gives $\mathcal{W}_{mix} \propto \kappa H_s^{-1}$. One of the limitations of this scaling is that it assumes constant diffusivity, which has been shown to vary over orders of magnitude in the ocean, with relatively high values being found over rough topography (Polzin et al., 1995). Observations and theoretical considerations further suggest that vertical eddy diffusivity depends on stratification (Gargett and Holloway, 1984; Gargett, 1984), and Nilsson et al. (2003) showed that the application of stratification-dependent diffusion models leads to different scalings for the MOC. The scaling for the meridional transport $\mathcal{V}$ is derived by assuming that the large-scale transport is geostrophic, and hence it depends on the pressure difference between the eastern and western boundaries. Furthermore, it is assumed that the zonal pressure difference is proportional to the meridional one, which yields

$$\mathcal{V} = C\frac{g\Delta\rho}{2f\rho_o}H_s^2, \tag{1}$$

with the gravitational acceleration g, a reference density ρ_o , some Coriolis parameter f and the non-dimensional proportionality constant C. Relation (1) can be justified dynamically when the meridional transport is balanced by friction (*e.g.*, Stommel, 1961; Welander, 1986;

[1]The same argument also holds for diapycnal instead of vertical diffusion (*e.g.,* Zhang et al., 1999).

Wright and Stocker, 1991, compare Section 1.1.3); in that case, C is proportional to the frictional parameter. Straub (1996) pointed out, however, that this relation does not hold in the Stommel-Arons model, and Greatbatch and Lu (2003) found that it holds in the Kawase model only when the damping is strong.

1.1.5 Idealized models forced by buoyancy flux and winds: The incorporation of wind forcing into the models for the THC constitutes a key step towards more complex and realistic solutions in the hierarchy. The dynamics of such solutions have been explored in numerous, idealized OGCM studies (*e.g.*, Bryan and Cox, 1968; Bryan, 1987; McDermott, 1996; Tsujino and Suginohara, 1999; Sumata and Kubokawa, 2001; Spall and Pickart, 2001; Klinger et al., 2004).

In contrast to solutions for the THC, the depth-integrated flow does not vanish in solutions with wind forcing, and westerly winds typically generate an anticyclonic, subtropical gyre to the south and a cyclonic, subpolar gyre to the north of the latitude, where the westerlies reach their maximum strength (Sverdrup, 1947). The gyres are closed by western boundary currents (Stommel, 1948; Munk, 1950). It has been noted that the gyre circulation interacts with the MOC by modifying the pathway of the MOC surface branch: In the subpolar gyre, where the barotropic western boundary current is directed southward, the poleward surface flow separates from the western boundary and is shifted into the interior, where it is part of the northward gyre circulation (*e.g.*, Bryan, 1987; Colin de Verdière, 1989).

Density advection within the subpolar gyre allows for the downwelling regions to be shifted away from the northeastern corner towards the west, which is more consistent with deep water formation in the Labrador Sea. This process is particularly efficient in the presence of strong eastern and northern boundary currents, as in the solutions with a continental slope reported by Spall and Pickart (2001).

Wyrtki (1961) and Toggweiler and Samuels (1995) noted that wind forcing generates upwelling in the southern ocean, where westerly winds drive a northward Ekman transport. As there is no zonal boundary in the latitude band containing the Drake Passage, an upper-ocean, meridional geostrophic flow cannot be established to compensate for the Ekman flow. Furthermore, Tsujino and Suginohara (1999) found that Ekman suction in a subpolar gyre

enhances the upwelling even in a closed basin, although not as efficiently as in the case with open zonal boundaries, as noted by Klinger et al. (2004). Because of these additional upwellings, the strength of overturning no longer follows the relatively simple scalings for the THC. A scaling that accounts for the additional upwelling in the southern ocean is proposed by Gnanadesikan (1999). According to that model, the system still equilibrates by adjusting the thermocline thickness H_s, however, and the strength of overturning in the northern basin is proportional to H_s^2 as in (1). Furthermore, it has been proposed that the advective-diffusive balance changes in the presence of strong, wind-driven vertical motion and currents. In that case, diffusive mixing is primarily balanced by horizontal advection in an internal boundary layer at the bottom of the upper layer that contains wind-driven flow (*e.g.,* Robinson and Stommel, 1959; Samelson and Vallis, 1997; Vallis, 2006). As a result, scaling arguments for solutions where the upwelling branch is dominated by such processes suggest that the strength of overturning is proportional to $\kappa^{1/2}$ rather than to $\kappa^{2/3}$ as in the case without winds. Finally, the increased complexity of the wind-forced solutions manifests itself not only in the strength but also in the structure of the overturning circulation: in addition to the primary, deep overturning cell, shallower, subtropical and subpolar overturning cells (STCs and SPCs) are present in the upper 500 m of the ocean (*e.g.*, Bryan, 1991).

As for the THC solutions, layer models emerged to provide dynamical explanations for various aspects of the wind and buoyancy forced solutions. Luyten et al. (1983) developed an inviscid model for the wind-driven ventilated thermocline. It consists of constant density layers, some of which outcrop in the subtropical gyre. At outcropping lines, the southward flowing water of the next deeper layer is subducted, and since only the upper-most layer is directly forced by the winds, planetary vorticity is conserved along streamlines in the layers below. Solutions typically have three regions, a ventilated region, and two unventilated regions, one at the eastern boundary, and one in the western part of the basin. The unventilated region at the eastern boundary is also called the shadow zone. It arises because geostrophic contours in subsurface layers are blocked by the eastern boundary, and hence the flow has to vanish along these lines. The western unventilated region is caused by a reversal of the Rossby wave speed, which can become eastward in regions with strong eastward barotropic flow (*e.g.,* Rhines and Young, 1982; Rhines, 1986). The subsurface flow

does not vanish in this western region, the solution there is largely affected by a boundary condition set by the western boundary current, however, which is not part of the model of Luyten et al. (1983). Such boundary conditions were derived and their affect on the solutions discussed in subsequent papers, *e.g.,* in Ireley and Young (1983) and Radko and Marshall (2010). McCreary and Lu (1994) extended the solutions of Luyten et al. (1983), by closing the circulation in $2\frac{1}{2}$-layer models, and explored the dynamics of the shallow, subtropical overturning cell (STC). They find that the tropical upwelling of subtropical water is remotely forced, *i.e.*, the strength of the STC is determined by the rate of subduction in the subtropical ocean, where the gyre circulation has a flow component in the direction of the surface-temperature gradient. Although the details of the circulation in the subtropical ocean are possibly not affecting the large-scale MOC at first order, the concepts developed in the studies above have also been applied to study the dynamics of the subpolar ocean.

The circulation in the subtropical and subpolar gyre in 2-layer models are discussed in the papers of Luyten and Stommel (1986), Huang (1986) Huang and Flierl (1987) and Nonaka et al. (2006). Using a model that does not allow for mass exchange in between the layers and hence conserves the volume in each layer, Huang (1986) and Huang and Flierl (1987) found that the model can be in subcritical and supercritical states, depending on the strength of the winds. In subcritical states, corresponding to weaker wind forcing, the deep layer is quiescent and the Sverdrup flow is entirely contained in the upper layer. With stronger forcing, however, the model adjusts to a supercritical state, where the layer interface outcrops in the western part of the subpolar gyre (for very strong winds, this region can even extend into the subtropical gyre), and the model reduces to a 1-layer system to the west of the outcropping line. There is also a northward interior boundary current, along the outcropping line, so that this model provides a possible mechanism to explain the separation of the Gulf Stream.

Nonaka et al. (2006) discussed a slightly different 2-layer model. Their model transfers mass from the deep into the upper layer to arrest the upper-layer thickness h_1 at a prescribed, minimum mixed-layer thickness $h_{\min}$, as dynamics attempts to shoal h_1 further in the outcropping region, that appears similarly as in Huang (1986) and Huang and Flierl (1987). This balance of mixed-layer entrainment and Ekman suction provides a dynamical

explanation for the enhanced upwelling and meridional overturning in Tsujino and Suginohara (1999). The model of Nonaka et al. (2006) also allows for a detrainment in a northern sponge layer, which is proportional to the (constant) eastern-boundary layer thickness h_e. As a result, h_e adjusts, so that entrainment and detrainment are balanced in the equilibrium solutions, rather than by conserving mass in each layer. Another result of a thin upper layer remaining on top of the deep layer and containing the Ekman flow in the outcropping region is that no boundary current along the outcropping region is needed to close the circulation.

Luyten and Stommel (1986) prescribed a detrainment velocity $w_s(y)$ to simulate surface cooling in the subpolar gyre, and to explore the dynamics of a circulation driven by buoyancy forcing and winds. Two different regimes are found in the solutions, depending on whether Rossby wave characteristics originate from the eastern or western boundary. In the regime near the eastern boundary, the flow is a linear superposition of the purely wind-driven solution with the Sverdrup flow being contained in the upper layer, and a purely buoyancy driven flow as in Pedlosky and Spall (2005). As the wind-driven geostrophic flow spreads over both layers in the western regime, the solution is more complex there. A strength of this model is that it focuses attention on the importance of wind and buoyancy forcing in driving the flow in the subpolar gyre. A limitation is, however, that it is not clear if the velocity across the layer interface, w_s, really represents the effect of a surface cooling, or what processes w_s corresponds to otherwise.

1.2 Present research

The purpose of the present study is to address unresolved dynamical questions regarding the dynamics of the AMOC in idealized solutions forced only by a buoyancy flux Q and solutions forced by Q and a zonal wind stress τ^x. A more specific goal is to understand the dynamical linkages among the tropical thermocline thickness H_s, Q, τ^x, $\mathcal{M}_n$ and $\mathcal{M}$, where $\mathcal{M}_n$ is defined is the formation rate of deep water and $\mathcal{M}$ as the net export of deep water out of the subpolar ocean.

In the first part of this manuscript, where a hierarchy of ocean models only forced by Q is considered, the following questions are addressed: What processes cause the thermally-

driven, across-basin flow to converge into the northeastern corner of the basin, downwell there, and return southward at depth? What processes maintain the pressure difference between the eastern and western boundaries that drives the MOC? Why does the thermocline thicken towards the pole? What is the effect of the surface-density gradient on the Rossby-wave speed? What processes damp Rossby waves near the cooling regions, to generate a northward flow convergence? How does the strength of Rossby-wave damping impact the strength of the MOC?

In a second part, where zonal wind forcing is included, questions are: How does the wind forcing modify the flow field and the dynamical picture derived from the solutions without winds? How is the horizontal circulation in the wind-driven gyres linked with the MOC, and how does it affect its strength? How is the deep-water formation related to the deep-water export from the subpolar ocean?

Finally, in a shorter, third part, the insight gained from the first two parts is used to address the questions, how the westerly winds over northern ocean basins affect the MOC. Specific questions are: How does H_s adjust to changes in the strength of the westerlies τ_o, and how does the strength of the overturning depend on τ_o?

To address these issues, solutions are obtained and analyzed using two types of models: a 2-layer version of a variable-density, layer ocean model (VLOM) and an ocean general circulation model (MITgcm). One advantage of VLOM is that it allows temperature to vary horizontally within layers, allowing it to be forced by Q rather than by a layer-thickness relaxation, as in the models of Pedlosky and Spall (2005), Luyten and Stommel (1986) and Nonaka et al. (2006). Another advantage is that solutions to simplified versions of VLOM can be obtained analytically, thereby allowing key processes to be readily isolated and studied. Finally, VLOM solutions are able to simulate many of the basic properties of the idealized MITgcm solutions discussed throughout this manuscript, including the poleward deepening of the thermocline and thermal-wind circulation; it therefore provides a powerful means for visualizing and interpreting the more complex MITgcm solutions. The advantage of the MITgcm is that it more accurately represents processes omitted or parameterized in VLOM. In particular, entrainment and detrainment processes parameterized in VLOM can be interpreted in terms of more familiar OGCM-mixing processes in MITgcm.

The systems considered in this manuscript differ considerably from the real oceans. For simplicity, salinity is kept constant, and surface density advection is heavily suppressed by using strong buoyancy forcing in both VLOM and MITgcm. The effect of salinity on density is dynamically most important in cold regions, where the effect of temperature on density is small, and the important impact of salinity and advection on the MOC has been recognized (*e.g.*, Stommel, 1961; Bryan, 1986; Marotzke and Willebrand, 1991; Winton, 1996; McManus et al., 2004; Curry and Mauritzen, 2005). The focus of this study is, however, to explore how *a given surface density field* affects the adjustment of the thermocline. A limitation of this approach is then that the question of how advection and the MOC feed back on the surface density field cannot be addressed. Since this simplification is necessary to allow for analytical solutions in VLOM, the feedback problem is left for later studies, hoping that the findings of the present study will help to understand the more comprehensive problem.

As in most prior studies discussed above, our numerical solutions are not eddy resolving. An underlying assumption of this study, then, is that large-scale, first-order MOC dynamics do not depend on the precise specification of small-scale processes, and that understanding the dynamics in non-eddying models is useful, if not necessary, to understand the effect of eddies on the circulation.

To reduce the complexity of the system and to limit the computational cost for a suite of numerical MITgcm solutions, all VLOM and MITgcm solutions are derived on a single hemispheric basin. This is a mismatch to the nature of the global MOC, which extends over all ocean basins. To partly compensate for this limitation, processes in other basins are included in parameterized form.

In most solutions, these processes are included in form of a sponge layer that prescribes a zonally uniform density field at the southern boundary in VLOM and MITgcm. A limitation of these VLOM and MITgcm solutions is that the tropical density structure cannot respond to adjustments further north, *i.e.*, southward-propagating, baroclinic Kelvin waves at the western boundary that are known to impact the tropical thermocline thickness (*e.g.*, Kawase, 1987) are quickly damped once they reach the sponge layer. As a result, questions like "How sensitive is the MOC transport $\mathcal{M}$ to a change in the strength of the zonal winds?" cannot directly be addressed, as the readjustment of the thermocline thickness H_s is surely a key part

of the ocean response (see Section 1.1.4). The advantage of introducing H_s as a boundary condition is, however, that the sensitivity of $\mathcal{M}(H_s)$, and the underlying dynamics, can be tested for a wide range of H_s without distorting the physics in the model domain (e.g., using *very* unrealistic values for diffusivity). To overcome limitations of this approach, an extended version of the VLOM solutions is discussed later, where H_s is not prescribed. In these solutions H_s adjusts to balance all entrainment and detrainment transports as in the model of Gnanadesikan (1999).

Key results of the analytical and numerical investigation are the following. As in the Sumata and Kubokawa (2001) study, Kelvin-wave adjustment deepens the mixed layer along the eastern boundary and determines its depth as a function of the tropical thermocline thickness H_s, and the mixed-layer temperature.

In (nearly) inviscid VLOM solutions forced only by the buoyancy flux Q, the eastern-boundary stratification is carried across the basin by Rossby waves, and subsequently solutions adjust to a steady state without an MOC. A similar, conceptual solution exists for the MITgcm. A strong-overturning state, where the deep ocean is filled with the coldest water in the system, develops only when Rossby waves are damped by mixing processes in a region where the surface temperature is close to its coldest value. As a result, the meridional pressure gradient drives an eastward, upper-layer flow that converges into the northeastern corner of the basin, and the thermocline thickness along the western boundary adjusts, so that a northward western boundary current can feed the interior flow. Consequently, the strength of the northeastern convergence and deep-water formations $\mathcal{M}_n$ depend on H_s and the strength of the Rossby-wave damping.

When models are forced by Q and zonal winds τ^x, an MOC develops even in (nearly) inviscid solutions, because relatively warm and light upper-layer water converges into the cooling region within the northward-directed, interior Sverdrup flow in the subpolar gyre. When winds are sufficiently strong (or H_s is small), a region emerges in the subpolar ocean near the western boundary, where the upper-layer thickness is reduced to a minimum, and the divergence of the Ekman flow is balanced by mixed layer entrainment. As a result, the geostrophic part of the Sverdrup flow extends over the whole water column inside this outcropping region, whereas the gyre flow is entirely contained within the upper layer otherwise.

Because of the entrainment within the outcropping region, and because it determines how the meridional Sverdrup flow is distributed over the upper and lower layers, the extent of this region also affects the strength and structure of the MOC. In VLOM, there exists a maximal, northward, upper-layer transport $\tilde{\mathcal{V}}_1(y)$ that can be maintained the model. The transport $\tilde{\mathcal{V}}_1(y)$ depends on H_s and τ^x, and has a minimum near the boundary of the two gyres y_W, where the Ekman transport is large. When the strength of the MOC exceeds $\tilde{\mathcal{V}}_1$ at any latitude, western-boundary-layer-entrainment occurs and reduces the MOC back to $\tilde{\mathcal{V}}_1$. This process occurs most notably at y_W, and when it is active, it essentially decouples the export of deep water from the subpolar ocean from the deep-water formation rate.

The manuscript is organized as follows. Chapter 2 describes the models and the experimental design. VLOM and MITgcm solutions forced only by differential heating Q are reported in Chapters 3 and 4. Solutions forced by Q and wind stress τ^x are discussed in Chapters 5 and 6 for both models. In Chapter 7, we discuss solutions to an extended version of VLOM without a sponge layer at the southern boundary of the domain. Chapter 8 provides a summary and discussion.

CHAPTER 2

Models

This chapter provides a description of the experimental design for the solutions derived in Chapters 3–6, a description of the two ocean models VLOM and MITgcm, and derivations of some useful model properties.

2.1 Experimental design

2.1.1 Basin, boundary conditions, and density: The model domain is a rectangular basin that represents the North Atlantic and extends meridionally from $y_s = 0°$ to $y_n = 60°$N, zonally from $x_w = 0°$E to $x_e = 40°$E (see left panel of Figure 3), and has a flat bottom at a depth $D = 4000\,\mathrm{m}$. Closed, no-slip conditions are applied at basin boundaries. For simplicity, salinity is kept constant and density is assumed to depend only on temperature according to

$$\rho = \rho_o(1 - \alpha T), \tag{2}$$

where $\rho_o = 1028\,\mathrm{kg/m^3}$ is a background density and $\alpha = 0.00015\,°\mathrm{C}^{-1}$ is the coefficient of thermal expansion. Thus, there is a one-to-one correspondence between density and temperature, and the two variables can be viewed as being interchangeable. In this regard, subscripts and superscripts are used consistently for the two variables, for example, so that T_1, T_s, T^* implicitly define the corresponding densities $\rho_1 \equiv \rho(T_1)$, $\rho_s \equiv \rho(T_s)$, and $\rho^* \equiv \rho(T^*)$.

2.1.2 Forcing: In all particular solutions presented in this manuscript, the models are forced by a heat (buoyancy) flux of the form

$$Q(x,y) = -\frac{T - T^*(y)}{\delta t}\theta(z + z_0), \tag{3}$$

where δt is a relaxation time that measures the strength of the heating, $\theta(\xi)$ is a step function ($\theta = 1$ for $\xi \geq 0$ and is zero otherwise). The relaxation temperature is

$$T^*(y) = \begin{cases} T_s, & y \leq y_1, \\ T_s + (T_n - T_s)\,\dfrac{y - y_1}{L}, & y_1 < y \leq y_2, \\ T_n, & y > y_2, \end{cases} \tag{4}$$

(see middle panel of Figure 3) with a maximum temperature in the southern part of the basin of $T_s = 23°\mathrm{C}$, and a northern minimum temperature of $T_n = 3°\mathrm{C}$. The latitudes delimiting the region with a surface temperature gradient are $y_1 = 30°\mathrm{N}$ in the south and $y_2 = 50°\mathrm{N}$ in the north, and $L = y_2 - y_1$. For VLOM, $z_0 = -h_1$, where h_1 is the thickness of layer 1 so that Q acts throughout layer 1, and $\delta t \to 0$, ensuring that the layer-1 temperature $T_1 = T^*(y)$. For MITgcm, $z_0 = -h_{\min} = -100\,\mathrm{m}$, so that the heating is confined to the upper 100 m. Since $\delta t = 3$ days, surface temperature advection is heavily suppressed, and the surface temperatures remain close to T^* in all MITgcm solutions. In order to separate the dynamics of MOC sinking from effects of the northern boundary, $T^*(y)$ is kept constant between y_2 and y_n (compare middle panel of Figure 3).

At the southern boundary, a sponge layer is attached south of y_s' in all solutions. In VLOM, where the limit $y_s' \to y_s$ is considered, the upper-layer thickness is prescribed, $h_1(y \leq y_s') = H_s$, at the southern boundary. In MITgcm, the sponge layer extends to $y_s' = 8°\mathrm{N}$, and a heat flux of the form

$$Q_D = \frac{\tilde{T} - T}{t_{sp}}\,\theta(y_s' - y) \tag{5}$$

is applied to relax temperatures towards $\tilde{T}(z)$. The temperature profile $\tilde{T}(z)$ is given by

$$\tilde{T}(z) = T_n + (T_s - T_n)\exp\frac{z + h_{min}}{\Delta H_s}\,\theta(-z - h_{\min}) + T_s\,\theta(z + h_{\min}), \tag{6}$$

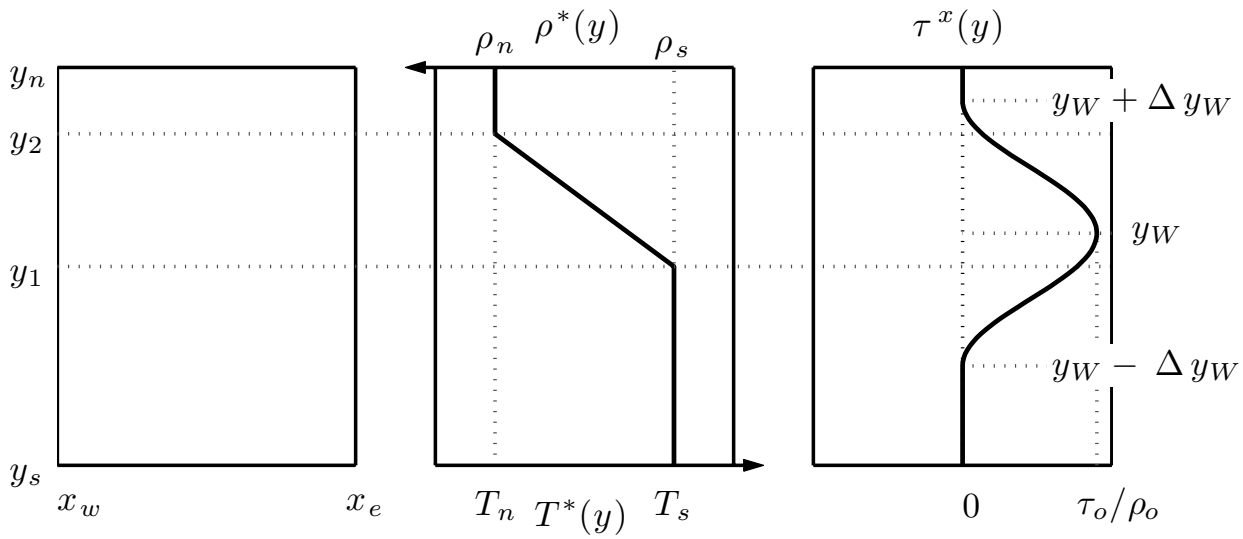

Figure 3: Schematic of the model domain (left panel), the relaxation temperature (4) in Q and corresponding density ρ^* (middle panel), and the zonal wind stress (8) in the right panel.

and decreases exponentially below a "mixed layer" of thickness $h_{\min}$, where temperatures are constant. The length scale ΔH_s increases from 100 to 300 m in 50 m increments in different numerical experiments. The relaxation time scale decays away from the southern boundary according to

$$t_{sp} = t_{sp0}\left[\cos\left(\pi\frac{y}{y_s' - y_s}\right) + 1\right], \tag{7}$$

where $t_{sp0} = 3$ days. With these parameter choices, $T(y_s) \approx \tilde{T}$ at all times, and baroclinic waves are strongly damped in the sponge layer. As a result, baroclinic, western-boundary Kelvin waves *cannot* feed back on the easterly, tropical thermocline depth H_s because they are completely absorbed before the reach the eastern boundary (see the discussion on the wave adjustment in the solutions of Kawase, 1987, in Section 1.1.4).

In Chapters 5 and 6 the models are forced by idealized, westerly winds of the form

$$\tau^x = \frac{1}{2}\frac{\tau_o}{\rho_o}\left[\cos\left(\frac{\pi}{\Delta y_W}(y_W - y)\right) + 1\right]\theta(\Delta y_W - |y - y_W|), \tag{8}$$

(compare right panel of Figure 3) where $y_W = 35°$N is the latitude where the westerlies reach their maximum, separating the subtropical and subpolar gyres. The lateral extent of

both gyres is $\Delta y_W = 20°$. The amplitude τ_o is a free parameter in VLOM, and numerical MITgcm solutions are obtained using values for τ_o of 0.07, 0.12 and $0.17\,\mathrm{N/m^2}$.

2.1.3 Initial states, spin up, and loss of stratification: For VLOM, the initial state is a state of rest with $h_1 = H_s$, $h_2 = D - H_s$, $T_1 = T^*$, and $T_2 = T_n$. For MITgcm, the initial state is a state of rest with $T = T_n$. Numerical solutions are spun up a period of 1000 years with acceleration in the temperature equation (Bryan, 1984), by which time they have adjusted close to equilibrium. The MITgcm solutions shown in Chapters 4 and 6 are averaged over the final 10 years of integration. Note that initially the models are unstratified in the region $y \geq y_2$, that is, the temperatures above and below $z = -h_{\mathrm{min}}$ are the same. This property also holds for the equilibrium solutions (exactly for VLOM and approximately for MITgcm).

2.2 VLOM

In this section, a simplified set of equations is derived for the baroclinic response in a variable-density, 2-layer model (VLOM), which is then solved in Sections 3 and 5. After reviewing more general equations for a variable-density, 2-layer model (*e.g.,* Jensen, 1998), the barotropic response is briefly discussed. Then, the barotropic solution is used to eliminate the sea-surface slope from the layer equations, assuming that the barotropic flow is in a quasi steady state. Since the barotropic solution includes additional physics in the western-boundary layer (horizontal viscosity) than in the interior ocean, different equations have to be derived for the baroclinic response in the two regions as well. Finally, we discuss the z-dependent flow within the upper layer of VLOM (*e.g.,* thermal wind), and characteristics of the baroclinic, Rossby-wave adjustment.

2.2.1 General variable-density, 2-layer model: The VLOM is a 2-layer system in which the layer temperatures T_i are allowed to vary horizontally. In contrast to constant-density, layer models, where layers are separated by an isopycnal surface, the layer thickness in the variable-density layer models is defined via the depth-integrated continuity equation in each layer, which also depends on prescribed entrainment/detrainment rules across the layer

interface. The VLOM can reduce to a one-layer system, either if the upper layer extends to the bottom ($h_1 = D$) so that the deep layer vanishes ($h_2 = 0$), or if $T_1 = T_2$ in which case the upper layer vanishes. A simple convection scheme prevents the statically unstable situation $T_1 < T_2$. Under certain circumstances, water is allowed to cross the layer interface as an entrainment/detrainment velocity w_1 (see Section 2.2.4).

A general set of equations for a variable-temperature layer model is

$$\boldsymbol{V}_{it} + f\boldsymbol{k} \times \boldsymbol{V}_i = -\langle \boldsymbol{\nabla} p_i \rangle + \delta_{i1}\boldsymbol{\tau} + \nu_h \boldsymbol{\nabla}^2 \boldsymbol{V}_i, \tag{9a}$$

$$h_{it} + \boldsymbol{\nabla} \cdot \boldsymbol{V}_i = w_i - w_{i-1}, \tag{9b}$$

$$T_{it} + \bar{\boldsymbol{v}}_i \cdot \boldsymbol{\nabla} T_i + w_1 (T_1 - T_2)\, \theta\, (w_i - w_{i-1}) = Q/h_1 \delta_{i1} + \kappa \boldsymbol{\nabla}^2 T_i, \tag{9c}$$

where subscript $i = 1, 2$ is a layer index, $\boldsymbol{V}_i = (h_i \bar{u}_i, h_i \bar{v}_i)$ are the depth-integrated layer transports per unit width, $\bar{\boldsymbol{v}}_i = (\bar{u}_i, \bar{v}_i)$ are the depth-averaged velocities, and w_i is the across-interface velocity at the bottom of layer i; there is no flow across the ocean surface or the ocean bottom so that $w_0 = w_2 = 0$. The horizontal gradient is denoted by $\boldsymbol{\nabla}$, the depth-integrated value of a variable by $\langle ... \rangle$. Vector $\boldsymbol{k}$ is a unit vector in the z-direction, and δ is the Kronecker delta symbol ($\delta_{11} = 1$ and $\delta_{21} = 0$). Variable $\boldsymbol{\tau}$ is the surface wind stress (bottom stress is ignored), and since only zonal wind stress $\tau^x(y)$ is considered in this manuscript, $\boldsymbol{\tau} = (\tau^x, 0)$. Finally, the pressure terms are the depth-integrated values of the pressure gradients in each layer,

$$\langle \boldsymbol{\nabla} p_1 \rangle = \frac{g h_1}{\rho_o} \left[\rho_1 \boldsymbol{\nabla} (h_1 + h_2) + \frac{h_1}{2} \boldsymbol{\nabla} \rho_1 \right], \tag{10a}$$

$$\langle \boldsymbol{\nabla} p_2 \rangle = \frac{g h_2}{\rho_o} \left[\rho_2 \boldsymbol{\nabla} (h_1 + h_2) - \rho_{21} \boldsymbol{\nabla} h_1 + h_1 \boldsymbol{\nabla} \rho_1 + \frac{h_2}{2} \boldsymbol{\nabla} \rho_2 \right], \tag{10b}$$

with $\rho_1 = \rho_o (1 - \alpha T_i)$ and $\rho_{21} = \rho_2 - \rho_1$.

Equations (9) differ from the most general, 2-layer model in that the advection and entrainment/detrainment terms are dropped from the momentum equations. A derivation of the equations for n-layer, variable-temperature, layer models is provided in Jensen (1998). The above equations also reduce to those for a 1-layer model when $h_1 = 0$ or $h_2 = 0$. Note that the wind stress has to be applied on the second layer, however, if layer 1 vanishes for (9) to be valid everywhere in the model domain.

2.2.2 Barotropic response: Throughout this manuscript, it is assumed that the barotropic flow is in a quasi-steady state. Since barotropic waves are much faster than baroclinic ones, this approximation appears to be reasonable for the purpose of studying the baroclinic response. Here, we derive equations for the barotropic response, as well as expressions for the constraints they impose on the baroclinic equations.

The equations for the steady state barotropic response are obtained by adding the equations for both layers, omitting all derivatives with respect to time. The sum of (9a) and (9b) then gives equations for the horizontal barotropic transports and preservation of volume,

$$f\boldsymbol{k}\times\boldsymbol{V} = -\boldsymbol{\nabla}P + \boldsymbol{\tau} + [\nu_h\boldsymbol{\nabla}^2\boldsymbol{V}], \qquad \boldsymbol{\nabla}\cdot\boldsymbol{V} = 0, \tag{11}$$

where $\boldsymbol{V} = \boldsymbol{V}_1 + \boldsymbol{V}_2$ and

$$\boldsymbol{\nabla}P = \langle\boldsymbol{\nabla}p_1\rangle + \langle\boldsymbol{\nabla}p_2\rangle = \frac{g}{2\rho_o}\boldsymbol{\nabla}\left(\rho_1 h^2 + \rho_{21}h_2^2\right), \tag{12}$$

with $h = h_1 + h_2$. Since $\boldsymbol{\nabla}P$ is a perfect differential, equations (11) give the familiar equation for the barotropic streamfunction,

$$\boldsymbol{k}\cdot\boldsymbol{\nabla}\Psi\times\boldsymbol{\nabla}f = \boldsymbol{\nabla}\times\boldsymbol{\tau} + \left[\nu_h\boldsymbol{\nabla}^4\Psi,\right] \tag{13}$$

where $U = -\Psi_y$ and $V = \Psi_x$. The viscous terms are enclosed in brackets, because they are considered only formally to allow for a western-boundary layer.

In the interior ocean, where viscosity is neglected, the steady state solution to (13) is the Sverdrup (1947) transport,

$$\Psi = \frac{1}{\beta}\tau_y^x(x_e - x) \qquad \text{or} \qquad V = -\frac{1}{\beta}\tau_y^x \quad \text{and} \quad U = -\frac{1}{\beta}\tau_{yy}^x(x_e - x), \tag{14}$$

where the boundary condition $U(x_e) = 0$ [or $\Psi(x_e) = 0$] is applied to integrate (13). With Ψ known, $\boldsymbol{\nabla}h$ is in general given by

$$g\boldsymbol{\nabla}h = -\frac{g}{2\rho_o}h\boldsymbol{\nabla}\rho_1 - \frac{1}{2D}\boldsymbol{\nabla}\left(g'h_2^2\right) + \frac{1}{D}\left(\boldsymbol{\tau} + f\boldsymbol{\nabla}\Psi\right), \tag{15}$$

which is derived by substitution of (12) into the inviscid version of (11), using the approximation $h_1 + h_2 \approx D$, and defining the reduced gravity coefficient $g' = g\left(\rho_2 - \rho_1\right)/\rho_2$.

At the western boundary, the barotropic solution is closed in a boundary layer. To conserve volume, its meridional transport $\mathcal{V}_w(y)$ has to be opposite to the zonally-integrated interior flow. Assuming that the boundary layer extends zonally from the western boundary x_w to a longitude x_w^+, integration of the interior flow (14) from x_e to x_w^+ yields

$$\mathcal{V}_w = \frac{1}{\beta}\tau_y^x(x_e - x_w^+). \tag{16}$$

Because the alongshore component of the boundary current is much larger than the flow normal to the boundary, viscosity is negligible in the zonal component of (11). In addition, the typical, meridional-boundary-layer assumption is made that that y-derivatives are negligible in the Laplacian operators. The boundary layer then takes the well-known form of a Munk (1950) layer with the width scale $L_{\text{Munk}} \sim (\nu_h/\beta)^{\frac{1}{3}}$. In this study, additional assumptions are made so that only the transports across the boundary layer are needed (see Chapters 3 and 5) not its precise structure. The method introduces a small, (negligible) error in the solutions, but has the advantage that solutions do not depend on the parameterization of mixing processes in the western boundary layer.

The zonal momentum equation in (11) without viscosity can be integrated zonally from x_w to any $x \leq x_w^+$ to get

$$-f\Psi = -P(x) + P(x_W) + \tau^x(x - x_w). \tag{17}$$

In the limit that $\nu_h \to 0$ it follows that $L_{\text{Munk}} \to 0$, so that the last term of (17) is negligible within the boundary layer, and hence the alongshore component of the boundary current is (nearly) geostrophic. Taking an x-derivative of (17) and using (12) then gives an equation for the zonal gradient in sea surface height,

$$gh_x = -\frac{gh}{2\rho_o}\rho_{1x} - \frac{h_2^2}{2h}g'_x - \frac{h_2}{h}g'h_{2x} + \frac{f}{h}V = -\frac{gh}{2\rho_o}\rho_{1x} - \frac{h_2^2}{2D}g'_x + \frac{h_2}{D}g'h_{1x} + \frac{f}{D}V, \tag{18}$$

where $h_1 + h_2 \approx D$ was applied in the second step. As discussed above, V is left unspecified in (18), as the we do not solve for the structure of the boundary layer. Equation (18) is used in Chapters 3 and 5 to estimate w_1 within the boundary layer.

2.2.3 Equations for the baroclinic response: To allow for analytical solutions for the baroclinic response in VLOM, it is necessary to simplify equations (9) further. The

simplified set of equations solved in Sections 3 and 5 is

$$f\boldsymbol{k} \times \boldsymbol{V}_i = -\langle \boldsymbol{\nabla} p_i \rangle + \delta_{i1}\boldsymbol{\tau} + \left[\nu_h \boldsymbol{\nabla}^2 \boldsymbol{V}_i\right], \tag{19a}$$

$$h_{it} + \boldsymbol{\nabla} \cdot \boldsymbol{V}_i = w_i - w_{i-1}, \tag{19b}$$

$$T_1 = T^* \qquad T_2 = T_n. \tag{19c}$$

In (19a), $\boldsymbol{V}_{1t}$ is dropped from (9a), which filters out gravity waves and allows only long-wavelength Rossby waves (The "large-scale geostrophic assumption" is discussed in more detail by Hasselmann, 1982; Maier-Reimer and Hasselmann, 1987; Maier-Reimer et al., 1993). As for the barotropic flow, the viscosity terms are retained only formally in the analytic model to allow for boundary currents, which is indicated by enclosing them in brackets. The layer temperatures are prescribed, formally by taking the limit $\delta t \to 0$ in the buoyancy flux (3), which sets the upper-layer temperature equal to the relaxation temperature T^*, and by dropping temperature advection across the layer interface from (9c), so that the deep layer temperature remains at its initial value T_n.

Assuming that the barotropic mode adjusts instantaneously, it is then possible to separate the baroclinic from the barotropic response, by eliminating the gradient of sea surface height from the pressure terms, using equations (15) in the interior and (18) in the western boundary layer. For the interior ocean, inserting (15) into (10a) gives

$$\begin{aligned}\langle \boldsymbol{\nabla} p_1 \rangle &= \frac{gh_1}{\rho_o}\left[-\frac{1}{2}h\boldsymbol{\nabla}\rho_1 - \frac{1}{2D}\boldsymbol{\nabla}\left(\rho_{21}h_2^2\right) + \frac{h_1}{2}\boldsymbol{\nabla}\rho_1\right] + \frac{h_1}{D}\left[\boldsymbol{\tau} + f\boldsymbol{\nabla}\Psi\right] \\ &= \frac{D-h_1}{D}\boldsymbol{\nabla}\left[\frac{1}{2}g'h_1^2\right] - \frac{gh_1}{2\rho_o}(D-h_1)\boldsymbol{\nabla}\rho_2 + \frac{h_1}{D}\left[\boldsymbol{\tau} + f\boldsymbol{\nabla}\Psi\right]\end{aligned} \tag{20}$$

where terms of order $(\rho_{21}/\rho)^2$ are neglected. Since $T_2 = T_n$ is constant in the solutions presented in this manuscript, the second term in (20) vanishes and the interior-ocean pressure terms reduce to

$$\langle \boldsymbol{\nabla} p_1 \rangle = \frac{D-h_1}{D}\boldsymbol{\nabla}\left[\frac{1}{2}g'h_1^2\right] + \frac{h_1}{D}\left[\boldsymbol{\tau} + f\boldsymbol{\nabla}\Psi\right] \tag{21a}$$

$$\langle \boldsymbol{\nabla} p_2 \rangle = -\frac{D-h_1}{D}\boldsymbol{\nabla}\left[\frac{1}{2}g'h_1^2 - (\boldsymbol{\tau} + f\boldsymbol{\nabla}\Psi)\right], \tag{21b}$$

where $\langle \boldsymbol{\nabla} p_2 \rangle$ follows from (12) and (15).

For the western-boundary layer, substitution of (18) into (10a) gives equations for the zonal pressure terms there,

$$\langle p_{1x} \rangle = \frac{D - h_1}{D} \left(\frac{1}{2} g' h_1^2 \right)_x + \frac{h_1}{D} f V, \tag{22a}$$

$$\langle p_{2x} \rangle = -\frac{D - h_1}{D} \left(\frac{1}{2} g' h_1^2 \right)_x + \frac{D - h_1}{D} f V, \tag{22b}$$

where the second-layer pressure term follows from V being geostrophic. Since no attempt is made to derive the detailed structure of the solution within the boundary layer, the alongshore pressure terms in the boundary layer are not used in this manuscript.

2.2.4 Across-interface velocities : Diapycnal processes are parameterized by the across-interface velocity, $w_1 = w_m + w_s + w_c + w_d$, which basically defines the character of the layer. Its components are given by

$$w_m = \frac{h_{\min} - h_1}{t_m} \, \theta(h_{\min} - h_1), \tag{23a}$$

$$w_s = \frac{H_s - h_1}{t_{sp}} \, \theta(y_s' - y), \tag{23b}$$

$$w_c = -V_1 \, \delta(y - y_2) \, \theta(V_1), \tag{23c}$$

$$w_d = -\frac{h_1 - h_{\max}}{t_d} \, \theta(h_1 - h_{\max}), \tag{23d}$$

each part simulating the effects of a specific process in MITgcm. Velocity $w_m \geq 0$ simulates entrainment into a surface "mixed layer" of thickness $h_{\min}$. In order to derive analytical solutions for VLOM, only the limit of the time scale $t_m \to 0$ is considered, which essentially limits the upper layer thickness h_1 to values larger and equal to $h_{\min}$; w_m is then calculated as the divergence of the flow when $h_1 = h_{\min}$ and is zero otherwise.

The sponge layer in VLOM is formally implemented by the velocity w_s. In the limit $t_{sp} \to 0$, considered in the present manuscript, w_s ensures that $h_1(y \leq y_s') = H_s$ at all times. Although the upper layer ceases to exist north of y_2, the upper-layer flow across y_2 does not necessarily vanish. Consequently, w_c is a detrainment velocity if $V_1(y_2) > 0$, and water that flows northward across y_2 is immediately cooled towards T_n and joins layer 2. In case of a

southward flow across y_2, Q acts to form a thin, upper layer, corresponding to the minimum mixed-layer thickness $h_{\min}$; as a result, most of the water that crosses y_2 is subducted, with only a small part of the flow being entrained via w_m. We note that a more general form of (23c) is $w_c = \boldsymbol{V}_1 \cdot \boldsymbol{n}\ \delta(y - y_2)\, \theta(\boldsymbol{V}_1 \cdot \boldsymbol{n})$, where $\boldsymbol{n}$ is the normal vector to y_2, pointing into the homogenous part of the ocean, a generalization that allows for a curved $y_2 = y_2(x)$.

Finally, velocity $w_d \leq 0$ represents detrainment, which occurs whenever dynamics attempts to make h_1 thicker than a maximum thickness $h_{\max}$; it represents processes in MITgcm that tend to stratify the water column (see Section 4.3). The time scale t_d is assumed to be slow compared to Kelvin-wave adjustments, but fast enough to efficiently damp Rossby waves before they can cross the basin. In Sections 3 and 5, solutions with $w_d = 0$ are reported first before the effect of non-zero w_d is discussed. A seemingly unpleasant property of the parameterization w_d is that subducted water instantaneously changes its temperature to T_2 as it moves from layer 1 to layer 2 so that heat is not conserved. Nevertheless, as argued in Section 4.3, w_d reasonably parameterizes Rossby-wave damping in a boundary layer that channels water to the north of y_2, where it is cooled to T_n.

2.2.5 Depth-dependent circulation: Although all solutions for VLOM are derived in terms of depth-integrated layer transports, it is possible to derive a z-dependent flow field $\boldsymbol{v}_i(z)$ within the layers. Since $\boldsymbol{v}_i(z)$ does not feed back onto the VLOM equations, because density advection of the shear velocities is neglected and layer temperatures T_i are depth-independent per definition, $\boldsymbol{v}_i$ is a conceptual extension of VLOM rather than an integral part of the model (*i.e.*, the depth-integrated part of the flow does not depend on the shear part). This extension is useful for two reasons. First, it allows for a better comparison of the horizontal circulation in VLOM and MITgcm, as MITgcm solutions are derived in velocities rather than layer transports. Second, it allows to address the question where water sinks in the VLOM solutions [Recall that w_1, in contrast, gives a (diapycnal) transport across the layer interface.].

The velocities $\boldsymbol{v}_i(z)$ are derived as follows. Wind stress is applied as a body force on an Ekman layer of thickness $h_{EK} \to 0$ at the top of the upper layer. For simplicity, $\boldsymbol{v}_1(z)$ are assumed to be geostrophic below the Ekman layer, and hence they are only valid in

the interior ocean, where viscosity is negligible. Although T^* varies only in the meridional direction in the solutions discussed in this manuscript, we allow for T_1 to be a function of both x and y, so that

$$u_1 = \frac{U_{1g}}{h_1} - \frac{g'_y}{f}(z + \frac{h_1}{2}), \qquad v_1 = \frac{V_{1g}}{h_1} + \frac{g'_x}{f}(z + \frac{h_1}{2}) - \frac{\tau^x}{f}\delta(z), \tag{24a}$$

where $\boldsymbol{V}_{1g} = (U_{1g}, V_{1g})$ denotes the geostrophic upper-layer transport. The second terms correspond to the shear part of the thermal wind, and they do not contribute the layer transports, and the third term in the equation for v_1 is the Ekman flow. With the boundary condition $w(z = 0) = 0$, the interior, steady-state, vertical velocity at $z \geq -h_1$ can then be derived by integration of the continuity equation,

$$w = w_{ek}\left(1 + \frac{z}{h_1}\right) - w_1\frac{z}{h_1} + \left(\frac{\boldsymbol{V}_{1g}}{h_1} \cdot \boldsymbol{\nabla}\, h_1\right)\frac{z}{h_1} + \frac{g'_y h_{1x} - g'_x h_{1y}}{2f}z + \frac{\beta g'_x}{2f^2}\left(z^2 + h_1 z\right), \tag{24b}$$

where the Ekman-pumping velocity

$$w_{ek} = -\left(\frac{\tau^x}{f}\right)_y = -\frac{\beta}{f}\left(\frac{\tau^x_y}{\beta} - \frac{\tau^x}{f}\right) = \frac{\beta}{f}\left(\frac{\tau^x}{f} + V\right) \tag{25}$$

was used. In the second layer, where T_2 is constant in all solutions, there is no thermal-wind shear and no Ekman transport (except for the region at $y > y_2$, where the upper layer vanishes), so that $\boldsymbol{v}_2 = \bar{\boldsymbol{v}}_2$ at $y \leq y_2$. At the boundaries where the velocities must vanish, $\boldsymbol{v}_i = 0$, but (24a) does not, geostrophy has to break down. The alongshore pressure gradients can then be balanced and water sinks or rises to close the circulation in boundary layers such as horizontal Ekman layers discussed in Section 4.1.2.

2.2.6 Baroclinic Rossby waves: This section is devoted to the derivation and discussion of the baroclinic Rossby-wave speed in VLOM. Rossby-wave adjustment plays an important role in all solutions presented in this manuscript, and many aspects of the solutions arise because Rossby-wave propagation is affected by the horizontal density gradient in the surface layer and the winds. For this discussion, the winds are assumed to be zonal and to depend only on y whereas the upper-layer temperature (and hence g') are allowed to vary both zonally and meridionally.

Substitution of (19a) into (19b) and using (21a) and (25) yields

$$h_{1t} + \boldsymbol{c}_r \cdot \boldsymbol{\nabla}\, h_1 = \frac{D - h_1}{D}\left(\frac{\beta h_1^2}{2f}g'_x - w_{ek}\right) + w_1, \tag{26}$$

where

$$\boldsymbol{c}_r = \left(-\beta\frac{D-h_1}{D}\frac{g'h_1}{f^2} + \frac{h_1^2 g'_y}{2Df} + \frac{U}{D}\right)\boldsymbol{i} + \left[-\frac{h_1^2 g'_x}{2Df} + \frac{1}{D}\left(\frac{\tau^x}{f} + V\right)\right]\boldsymbol{j}, \tag{27}$$

is the baroclinic Rossby-wave speed[2], and $\boldsymbol{i}$ and $\boldsymbol{j}$ are the unit vectors in the x and y directions, respectively. Without the terms depending on the density gradients, $\boldsymbol{c}_r$ is identical to the wave speed discussed in Rhines (1986).

The zonal wave speed c_r^x in (27) has three terms. The first one corresponds to the wave speed in a linear model and is always directed westwards. The second term depends on the upper-layer, meridional density gradient. In absence of topography, this density gradient does not enter the barotropic vorticity balance, and hence barotropic waves adjust the sea-surface slope such that a depth-independent velocity compensates for the density driven flow in the upper layer. The second term is equivalent to this depth-independent velocity, which then doppler-shifts the baroclinic waves. In this manuscript, this wave-speed component is always westward as the surface density increases polewards ($g'_y < 0$). The third term is the depth-averaged, zonal velocity. In the solutions presented in this manuscript, U is given by (14), the barotropic Sverdrup flow in the subtropical and subpolar gyres.

Note that U is *eastward* in the northern part of the subtropical and the southern part of the subpolar gyre. In this region, it is possible for U to be so large that c_r^x reverses sign to become positive. This reversal is dynamically important, because solutions for VLOM are generally derived by integrating along Rossby wave characteristics from the eastern boundary, where the boundary condition is determined by Kelvin-wave dynamics (see Chapters 3 and 5). This methodology fails, however, in regions that are not filled with eastern-boundary, Rossby-wave characteristics, and a different approach has to be taken. In this case, regions with eastward Rossby-wave speed can be filled by Rossby-wave characteristics connected to the western, rather than eastern, boundary; consequently, the boundary condition for the characteristic integration is determined by the physics of the western-boundary layer

[2]Formally, the wave speed is derived from (26) by decomposing h_1 into a slowly varying mean $\bar{h}_1$ and a fast-varying, small-amplitude ($\bar{h}_1 \gg |H_1|$) wave part of the form $h'_1 = H_1 \exp \imath(kx + ly - \omega t)$ with the zonal (meridional) wave number k (l), and the angular frequency ω. We neglect terms of order H_1^2, and then follow the WKBJ method (*e.g.*, Bender and Orszag, 1978) by omtting derivatives of $\bar{h}_1$ in the first order equation, which then solved for ω is the dispersion relation. The group speed is the gradient of ω in wave-number space, that is $\boldsymbol{c}_r = (\omega_k, \omega_l)$. Because of the right hand side of (26), the dispersion relation also has a imaginary part, which describes the change in h_1 along Rossby-wave characteristics.

(Ireley and Young, 1983; Radko and Marshall, 2010), which then directly affects the interior solution.

The meridional velocity component c_r^y has a term depending on the zonal, surface-density gradient and another one corresponding to the depth-averaged geostrophic flow. In solutions without a zonal density gradient, it follows that c_r^y is zero outside the wind-driven gyres, and is northward (southward) to the north (south) of y_r, where y_r is the latitude where the Sverdrup and Ekman transports add up to zero (and hence $w_{ek} = 0$), that is, at the latitude where

$$\frac{\tau_y^x}{\beta} - \frac{\tau^x}{f} = 0, \qquad @ \; y = y_r. \tag{28}$$

According to (8), y_r occurs in the northern part of the subtropical gyre, where the Ekman transport is directed southward and the Sverdrup transport northward.

The terms on the right-hand side of (26) describe the change in layer thickness along a Rossby wave characteristic. The first term, proportional to g'_x indicates that in case the other terms vanish, h_1 adjusts to cancel the zonal, depth integrated pressure-gradient in the layers. The Ekman-pumping velocity w_{ek}, thickens h_1 along characteristics to the south of y_r and thins h_1 to the north of y_r. Finally, h_1 is also influenced by w_1. Entrainment processes ($w_1 > 0$) tend to thicken the layer along characteristics, whereas detrainment processes have the opposite effect.

2.3 MITgcm

2.3.1 Overview: MITgcm is a numerical-modeling toolbox designed at the Massachusetts Institute of Technology to solve different sets of equations describing the atmosphere and the ocean, and climate (Hill and Marshall, 1995; Marshall et al., 1997). In the present study, it is configured to solve a finite-volume form of the standard hydrostatic, Boussinesq, primitive equations on spherical coordinates with a free surface. It uses a flux-limiting third order direct space-time method scheme for the advection of tracers.

The C-grid has 36 vertical levels with a uniform resolution of 20 m in the upper 400 m, gradually decreasing to 540 m near the bottom, and its horizontal resolution is 0.5°×0.5°. The parameterization of horizontal mixing is Laplacian, with coefficients $\nu_h = 2\times10^4\,\mathrm{m^2\,s^{-1}}$

for viscosity and $\kappa_h = 10^2\ \mathrm{m^2\,s^{-1}}$ for diffusion. Neither isopycnal diffusion (Redi, 1982; Cox, 1987) nor thickness diffusion (Gent and McWilliams, 1990) are used. Coefficients of vertical viscosity and diffusivity are both $10^{-5}\,\mathrm{m^2\,s^{-1}}$. In addition, a simple, convective-adjustment scheme removes unstable stratification by vertically mixing density (temperature).

2.3.2 Definitions of layer-thicknesses:

To compare MITgcm and VLOM solutions, it is useful to define a measure for an upper-layer thickness in MITgcm that can be compared to h_1 in VLOM. Because the vertical structure in MITgcm solutions is more complex than that in VLOM, several definitions of upper-layer thicknesses are possible. Three useful choices are listed below:

Mixed-layer thickness, $\boldsymbol{h_m}$: The mixed layer is in direct contact with the atmospheric forcing, and it is defined as that part of the ocean where the temperature is close to the surface temperature, that is,

$$h_m = \int_D^\eta \theta\left[T - T(z=0) + \Delta T_m\right]\, dz. \tag{29}$$

In analytical solutions, $\Delta T_m \to 0$ and $\Delta T_m = 0.1^\circ$ in numerical solutions. Because of the strong buoyancy forcing Q, the surface temperature $T(z=0) \approx T^*$, and h_m cannot become (much) thinner than $h_{\min}$. The mixed-layer thickness can thicken considerably, however, in cooling regions, or where the horizontal flow converges and water sinks.

Upper-layer thickness by water-mass properties $\boldsymbol{h_{\hat{T}}}$: Another upper-layer thickness, $h_{\hat{T}}$, is defined by the depth of the $\hat{T}$-isotherm,

$$h_{\hat{T}} = \int_D^0 \theta(T - \hat{T})\, dz. \tag{30}$$

This definition is also useful, because subsurface flow tends to be along isotherms in the limit of no mixing, so that the flow across isotherms is a good measure of mixing processes. Throughout this manuscript, the horizontal depth-integrated flow above an isotherm is defined as $\boldsymbol{V}_{\hat{T}}$, and the flow across an isotherm $w_{\hat{T}}$ (e.g., $\boldsymbol{V}_{3.2}$ and $w_{3.2}$ in case of the 3.2°-isotherm). Note that $w_{\hat{T}} = \boldsymbol{\nabla} \cdot \boldsymbol{V}_{\hat{T}}$ in steady state solutions.

Upper-layer thickness by dynamics, h_1: A measure for upper-layer thickness that is dynamically related to h_1 in VLOM is

$$h_1 = \left(2 \int_{-D}^{0} \int_{-D}^{z} \frac{\rho_n - \rho}{\rho_n - \rho^*} \, dz' \, dz \right)^{1/2}, \tag{31}$$

as derived next. Corresponding horizontal transports $\boldsymbol{V}_1$ and their convergence w_1 can be defined by using the VLOM Equations (19) and (21), and $g' = g\alpha \, [T(z=0) - T_n]$. As we shall see, V_1 is then a good indicator for the direction and strength of the interior, upper-ocean flow (see Chapters 4 and 6). Thickness h_1 is only defined in regions where $\rho^* > \rho_n$, that is (approximately) south of y_2 in the (numerical) solutions presented in this manuscript. How h_1 is related to the surface layer pressure, and some other properties of that measure, are discussed below.

Note that all three definitions of upper-layer thickness (as well as corresponding, upper-layer transports) converge in the limit that the ocean has a density structure like that of a 2-layer model, that is, a vertically homogenous, upper layer overlying a deep ocean with uniform temperature T_n; the exception is that $h_{\hat{T}}$ ceases to exist north of the isotherm's outcropping line.

2.3.3 Derivation and properties of the pressure function P_1: In this section, we derive a function $P_1(x, y)$ for the depth-integrated pressure in the surface layer, which is closely related to h_1 as defined in (31). Then, we discuss some properties of P_1 and h_1, which are useful to relate h_1 in MITgcm and in VLOM throughout the manuscript.

We start with the hydrostatic equation

$$p_z = -\frac{g}{\rho_n} \rho, \tag{32}$$

where ρ_n is the density of the heaviest water in the system that fills the ocean at depth. Using the surface boundary condition $p(\eta) = 0$, (32) can be integrated vertically to give

$$p = \frac{g}{\rho_n} \int_{z}^{\eta} \rho \, dz'. \tag{33}$$

The bottom pressure $p_D \equiv p(D)$ can then be decomposed into

$$p_D = \frac{g}{\rho_n} \int_{-D}^{\eta} \rho \, dz = \frac{g}{\rho_n} \int_{-D}^{0} \rho_n \, dz - \frac{g}{\rho_n} \int_{-D}^{0} (\rho_n - \rho) dz + \frac{g}{\rho_n} \int_{0}^{\eta} \rho \, dz. \tag{34}$$

Taking the limit that the ocean is indefinitely deep ($D \to \infty$) and assuming that the horizontal pressure gradient vanishes at depth ($\boldsymbol{\nabla} p_D = 0$), as in a classical $1\frac{1}{2}$-layer model, it follows that

$$\int_0^{\eta} \rho \, dz = \int_{-D}^{0} (\rho_n - \rho) dz. \tag{35}$$

Decomposition of (33) as in (34) and substitution of (35) then gives

$$p = \frac{g}{\rho_n} \int_z^0 \rho_n \, dz' + \frac{g}{\rho_n} \int_{-D}^{z} (\rho_n - \rho) dz. \tag{36}$$

Since the first term in (36) is a constant, it contributes only to the static pressure and so can be safely neglected. Integrating the second term over the water column, yields

$$P_1 = \frac{g}{\rho_n} \int_{-D}^{0} p \, dz = \frac{g}{\rho_n} \int_{-D}^{0} \int_{-D}^{z} (\rho_n - \rho) \, dz' \, dz. \tag{37}$$

Defining a reduced-gravity variable to be $g' = g \left[\rho_n - \rho(z = 0)\right] / \rho_n$, and assuming that the depth-integrated pressure has the form $P_1 = \frac{1}{2} g' h_1^2$ as it does in a reduced-gravity model, the upper-layer thickness is then given by (31).

As a consistency check, a desirable property is that if the density has a layer-like structure, so that

$$\rho = \rho_n - (\rho_n - \rho^*) \theta(z + \tilde{h}_1), \tag{38}$$

then the layer thickness provided by (31) is $\tilde{h}_1$. This property is demonstrated by direct substitution of (38) into (31),

$$\frac{1}{2} h_1^2 = \int_{-D}^{0} (z + \tilde{h}_1) \, \theta(z + \tilde{h}_1) \, dz = \frac{1}{2} \tilde{h}_1^2, \tag{39}$$

which shows that (31) gives the "correct" layer depth.

As discussed in later chapters, the boundary condition, $P_{1y} = 0$, is established by Kelvin-wave adjustments along the eastern boundary. In an OGCM with horizontally uniform density $\rho_A(z)$ below a mixed layer of thickness $h_m(x, y)$ and a vertically uniform density $\rho^*(x, y)$ within the mixed layer, this boundary condition means that h_m is adjusted to satisfy the relationship,

$$h_{my} = \frac{h_m}{2} \frac{\rho_y^*}{\rho_A(-h_m) - \rho^*}, \tag{40}$$

as derived in Sumata and Kubokawa (2001). To see this property, take the y-derivative of (37) to get

$$\begin{aligned}\frac{\rho_n}{g}P_{1y} &= \left[\int_{-D}^{-h_m}\int_{-D}^{z}(\rho_n-\rho_A)dz'\,dz + \int_{-h_m}^{0}\int_{-D}^{-h_m}(\rho_n-\rho_A)dz'\,dz + \int_{-h_m}^{0}\int_{-h_m}^{z}(\rho_n-\rho^*)dz'dz\right]_y \\ &= -h_{my}h_m(\rho_n-\rho_A(-h_m)) + \int_{-h_m}^{0}\left(h_{my}(\rho_n-\rho^*) - \int_{-h_m}^{z}\rho_y^* dz'\right)dz \\ &= h_{my}h_m(\rho_A(-h_m)-\rho^*) - \rho_y^*\frac{h_m^2}{2}, \end{aligned} \tag{41}$$

and (40) follows directly from setting $P_{1y}=0$ in (41).

Consider solutions that satisfy the boundary condition $P_{1y}=0$ and in which the mixed layer extends to the ocean bottom ($h_m=D$) at the eastern boundary north of some latitude y'. It follows that *i)* the upper layer extends to the bottom ($h_1=D$) at the same latitude as the mixed layer and *ii)* that y' is determined by

$$g'(y') = g'(y_s)\frac{h_1^2(y_s)}{D^2}, \tag{42}$$

if the surface density along the eastern boundary and the vertical density profile at some y_s are known and density is horizontally uniform below the mixed layer. Since $\rho_A(z<-h_m)>\rho^*$ at every latitude, it follows directly from (31) that $h_1<D$ if $h_m<D$ and $h_1=D$ if $h_m=D$, which proves *i)*. Conclusion *ii)* follows immediately because $P_1=\frac{1}{2}g'h_1^2$ is constant along the eastern boundary to the south of y'.

Finally, substitution of (6) into (31) gives

$$H_s = \left[2\int_{-D}^{0}\int_{-D}^{z}\exp\frac{z+h_{\min}}{\Delta H_s}\,dz'\,dz\right]^{1/2} = \left((h_{\min}+\Delta H_s)^2+\Delta H_s^2\right)^{1/2}, \tag{43}$$

where $\exp(-D/\Delta H_s)\ll 1$ is used in the second step. Equation (43) relates the density profile within the sponge layer (6) to H_s in VLOM.

CHAPTER 3

VLOM solutions forced by differential heating

In this chapter, we discuss the VLOM response to buoyancy forcing Q without winds. After reviewing the governing equations (Section 3.1), we first report an inviscid solution ($w_d = 0$) that does not have an MOC (Section 3.2), and then a viscid one ($w_d \neq 0$) that does have an MOC (Section 3.3). We proceed by examining the upper-layer, depth-dependent flow in these solutions (Section 3.4), and conclude with a discussion about the strength of the MOC (Section 3.5). For simplicity, Cartesian coordinates and the equatorial β-plane approximation ($f = \beta y$) are used in all derivations; however, solutions are evaluated in spherical coordinates, so that they are as comparable as possible to the MITgcm solutions reported in Chapter 4. Finally, for notational convenience variables are written as functions of space only, even though they are time dependent in the spin up.

3.1 Equations of motion

Since there is no wind forcing for the solutions discussed in this chapter, equations (19) for the upper layer reduce to

$$-fV_1 + \frac{D - h_1}{2D}\left(g' h_1^2\right)_x = \left[\nu_h \boldsymbol{\nabla}^2 U_1\right], \tag{44a}$$

$$fU_1 + \frac{D - h_1}{2D}\left(g' h_1^2\right)_y = \left[\nu_h \boldsymbol{\nabla}^2 V_1\right], \tag{44b}$$

$$h_{1t} + \boldsymbol{\nabla} \cdot \boldsymbol{V}_1 = w_1, \tag{44c}$$

where $g' = g\alpha\,(T_1 - T_2) = g\alpha\,(T^* - T_n)$. The barotropic flow vanishes in the solutions without winds, and hence the deep-layer flow mirrors the upper-layer circulation ($\boldsymbol{V}_2 = -\boldsymbol{V}_1$), and the terms for the depth-integrated pressure gradients in the interior ocean (21) and in the western boundary layer (22) are identical.

3.2 Solution without overturning

In this section, we consider the response to (44) when $w_d = 0$ and viscosity is significant only in the western boundary layer. With these restrictions, the model can adjust to a state where $w_1 = 0$ everywhere. This solution describes the most basic response to a surface-temperature gradient in VLOM, and is useful to compare to the more complex situations in later chapters.

3.2.1 Spin up : The baroclinic model spin up can be conceptually subdivided into four stages: An initial response, a fast Kelvin-wave response, the slower Rossby-wave adjustment and a final adjustment in the western boundary layer. All four stages are schematically illustrated in Figure 4.

3.2.1.1 Initial response: The surface temperature is given by $T_1 = T^*(y)$ (Eq. 4 and Fig. 3), and the upper-layer thickness is initially given by $h_1 = H_s$. Consequently, there is a meridional pressure gradient in layer 1 proportional to $g'_y = g\alpha T^*_y$, and the response across the interior ocean is therefore

$$U_1 = -\frac{D - H_s}{2Df} g'_y H_s^2, \quad V_1 = 0, \quad h_1 = H_s. \tag{45}$$

Note that $U_1 = 0$ south of y_1 because $g'_y = 0$ there. Figure 4 (top-left panel) illustrates this stage of the adjustment, showing an eastward current across the basin in layer 1 overlying a compensating westward flow in layer 2 (Stage 1). Along the eastern boundary there is a convergence of layer-1 water due to U_1 that tends to deepen h_1. Conversely, along the western boundary U_1 drains layer-1 water from the coast, a process that lifts up the layer interface.

3.2.1.2 Eastern boundary: At the same time, slower baroclinic adjustments begin that eventually ensure that all flow vanishes. Along the eastern boundary ($x = x_e$),

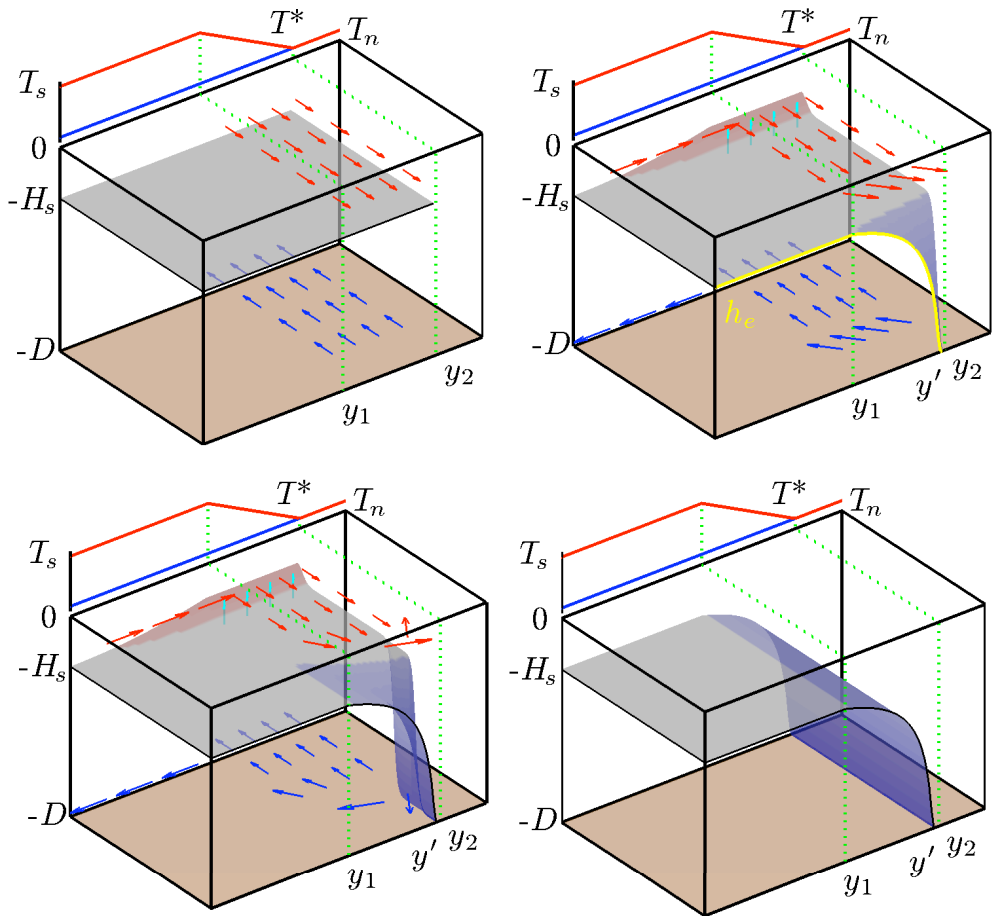

Figure 4: Schematic plot of the spin-up of the no-MOC solution for VLOM without winds, illustrating the response during the initial adjustment (Stage 1; top-left), just after the eastern-coastal adjustment (Stage 2; top-right), during the Rossby-wave adjustment (Stage 3; bottom-left), and the final, steady steady-state (Stage 4; bottom-right).

Kelvin waves radiate northward, and after their passage[3] the coastal layer thickness, $h_e(y) \equiv h_1(x_e, y)$, adjusts to ensure that there is no flow into the coast. Setting $U_1(x_e, y) = 0$ and ignoring viscosity in (44b) implies that

$$(g' h_e^2)_y = 0 \qquad \text{or} \qquad h_1 = D. \tag{46}$$

Since $h_e(y_s) = H_s$ is prescribed in the southern sponge layer, the eastern-boundary-layer

[3]Note that the time derivatives in equations (44) are neglected, which essentially sets the Kelvin-wave speed to infinity. Hence this adjustment occurs instantaneously.

thickness adjusts to

$$h_e(y) = \begin{cases} H_s \left(\dfrac{g'_s}{g'}\right)^{1/2} & y \leq y', \\ D & y \geq y' \end{cases} \tag{47}$$

where $g'_s = g'(y_s)$ and y' is defined as the latitude where the layer interface first reaches the bottom, that is, by the relation $H_s \left[g'_s/g'(y')\right]^{1/2} = D$. It is remarkable that a similar balance holds for the mixed-layer thickness in continuously stratified models (Sumata and Kubokawa, 2001, Section 4 of this manuscript); furthermore, (47) also holds exactly for the measure of upper-layer thickness h_1 in an OGCM defined in Section 2.3. Furthermore, this eastern-boundary structure provides the cornerstone for all other solutions discussed in this thesis.

North of y', the model ocean consists of only one layer at $x = x_e$ and the sea surface slope adjusts in order to cancel U_1. Note that although the approximation $h_1 + h_2 = D$ is implicit in the equations for the baroclinic motion, the sea-surface slope is still, up to the dominant order, correctly described by (15).

Figure 4 (top-right panel) schematically illustrates the response at this stage of the adjustment, that is, shortly after the passage of Kelvin waves along the eastern boundary (Stage 2). Along the coast $h_1 = h_e$, whereas more than a Rossby radius of deformation offshore the ocean remains in state (45). As a result, the inflow in layer 1 is channeled into a northward, geostrophic, coastal current in layer 1 and a compensating, southward flow in layer 2. It is notable that both currents vanish at $y \geq y_2$ where $g' = 0$, and hence $w_c = 0$.

3.2.1.3 Interior ocean: The eastern-coastal response (47) does not remain trapped to the coast, but rather propagates westward via baroclinic Rossby waves with the zonal wave speed

$$c_r^x = -\beta \frac{D - h_1}{D} \frac{g' h_1}{f^2} + \frac{h_1^2 g'_y}{2Df}, \tag{48}$$

as derived in Section 2.2.6 (Eq. 27). The second term on the right-hand side ensures that the baroclinic Rossby-wave adjustment is completed within a finite period for all $y \leq y_2$, as it is negative and remains finite even as $g' \to 0$ at y_2 (compare Fig. 5). Interestingly, $|c_r^x|$

even increases by an order of magnitude near y_2, due to the thickening of h_1 according to (47).

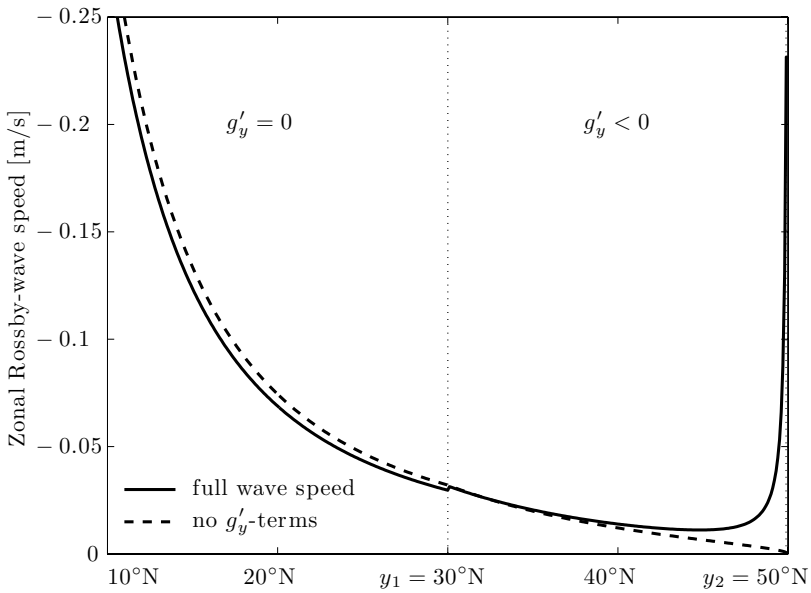

Figure 5: Zonal Rossby-wave speed c_r^x (solid curve) in VLOM without winds, given by (48) with an upper layer thickness as given by (47) and $H_s = 300\,\mathrm{m}$. For comparison, the Rossby-wave speed in a $1\frac{1}{2}$-layer model is also shown (dashed line), derived by taking the limit $D \to \infty$ in (48), which gives only the first term in (48) with $(D - h_1/D) = 1$. The unit for both velocities is m/s.

Since $w_1 = 0$ ($w_d = 0$ by assumption and $h_1 > h_{\min}$), (26) then implies that h_e propagates unchanged across the basin as an interfacial front. Figure 4 (bottom-left panel) illustrates this Rossby-wave adjustment (Stage 3). West of the front, the ocean is in the state (45) with $h_1 = H_s$; everywhere east of it, h_1 is adjusted to h_e and there the ocean is in a state of no motion ($\boldsymbol{V}_1 = 0$).

3.2.1.4 Western boundary: Consider the response very near the western boundary at an intermediate time (after Stage 2) before the Rossby-wave front from the eastern boundary arrives. Eastward U_1 drains water from the coast and lifts up the layer interface. At the same time, southward-propagating Kelvin waves, and the damping of eastward-propagating, short-wavelength Rossby waves, set up a northward western-boundary current to feed the eastward flow (Gill, 1982). That boundary current eventually extends southward into the sponge layer at y_s, where the circulation is closed by transferring water from the

deep layer into the surface layer via w_s. Since all baroclinic waves are completely damped by the strong relaxation of h_1 to H_s, no signal propagates eastward along the equator, and hence there is no feedback onto the eastern-boundary layer thickness.

At intermediate times, the western-boundary circulation adjusts to a temporary equilibrium state. In the following, solutions are derived for this intermediate state. Specifically, we obtain the coastal, upper-layer thickness $h_w(y) \equiv h_1(x_w)$, the western-boundary-current transport $\mathcal{V}_{1w}(y) \equiv \int_{x_w}^{x_w^+} V_1\, dx$, and the zonally integrated boundary-layer entrainment at each latitude, $W_m(y) \equiv \int_{x_w}^{x_w^+} w_m(x,y)\, dx$, where x_w^+ is a longitude just east of the boundary layer. (Going through this somewhat lengthy exercise is useful, as it provides a relatively simple example for the methodology that is also applied to obtain western-boundary-layer solutions in later chapters, where the situation is more complex.) As we shall see, the offshore U_1 attempts to thin h_w even further than $h_{\min}$ for certain values of H_s, so that W_m is needed to ensure that $h_w \not< h_{\min}$, and hence U_1 is partially fed by local western-boundary entrainment[4]. In the limit $H_s \to h_{\min}$ all water is entrained locally, and no western-boundary current develops, otherwise the boundary current extends into the sponge layer at y_s, where the circulation is closed via w_s.

At the western boundary, imposing the boundary condition $U_1(x_w) = 0$ does not result in the same equation for coastal layer thickness as at the eastern boundary, because the alongshore pressure gradient does not vanish but is rather balanced by the viscous term $\nu_h V_{1xx}$ due to western-boundary current. Instead, that boundary condition is used to integrate (44c) across the boundary layer, to get

$$\mathcal{V}_{1wy} + U_{1w}^+ = W_m, \tag{49}$$

where $U_{1w}^+(y) \equiv U_1(x_w^+)$ is provided by (45). The alongshore component of the western-boundary current $\mathcal{V}_{1w}$ is assumed to be geostrophic, so that the zonal integration of the pressure term in (44a) gives an equation relating $\mathcal{V}_{1w}$ to h_w,

$$\mathcal{V}_{1w}(y) \equiv \int_{x_w}^{x_w^+} V_1(x,y)\, dx = \frac{g'}{2f}\left[h_w^{+2} - h_w^2 - \frac{2}{3D}(h_w^{+3} - h_w^3)\right], \tag{50}$$

[4]It is assumed that h_1 has its minimum at x_w throughout the boundary layer, so that w_m is only active if $h_w = h_{\min}$. This assumption allows $\mathcal{V}_{1w}$ and h_w to be obtained without solving for the detailed structure of the boundary layer. The assumption is reasonable in steady state, as the boundary layer resembles a Munk layer and and the upper-layer transport is directed to the north.

where $h_w^+(y) \equiv h_1(x_w^+, y) = H_s$ is given by (45). Substitution of (50) and (45) into (49) yields

$$-\frac{g'_y}{2f}\left[h_w^2 - \frac{H_s^3}{3D} - \frac{2h_w^3}{3D}\right] - \frac{g'}{f}h_w\left(1 - \frac{h_w}{D}\right)h_{wy} - \frac{\beta g'}{2f^2}\left[H_s^2 - h_w^2 - \frac{2}{3D}(H_s^3 - h_w^3)\right] = W_m, \tag{51}$$

where $W_m \neq 0$ only if $h_w = h_{\min}$.

Consider the solution to (51) at $y = y_2$. Since the second and third terms on the left-hand side of (51) vanish at y_2 where $g' = 0$, $W_m(y_2) > 0$ only if the first term is positive when $h_w = h_{\min}$, that is, if $H_s < \hat{H}$ where

$$\hat{H} \equiv \left(3Dh_{\min}^2 - 2h_{\min}^3\right)^{\frac{1}{3}}. \tag{52}$$

Assume that H_s is less than $\hat{H}$ so that $W_m(y_2) > 0$. Then, how far south does the region where $W_m(y_2) > 0$ extend? In that region, $h_{wy} = 0$ since $h_w = h_{\min}$ and so the second term on the left-hand side of (51) vanishes. Because the third term on the left-hand side grows faster than the first, the left-hand side goes to zero at some latitude y_e. South of y_e, the entrainment vanishes [$W_m(y) = 0$], and (51) is balanced by adjusting h_{wy}.

In summary, there are two cases, in which (49) is integrated in different ways:

Case 1: If $H_s < \hat{H}$ there is boundary entrainment. North of y_e, $h_w = h_{\min}$, $\mathcal{V}_{1w}$ can be directly evaluated using (50), and W_m is given by (51). South of y_e, $W_m = 0$, so that $\mathcal{V}_{1w}$ is obtained by integrating (49) southward from y_e, using $\mathcal{V}_{1w}(y_e)$ as a boundary condition. Finally, h_w can be calculated by inverting (50).

Case 2: If $H_s \geq \hat{H}$, no entrainment occurs ($W_m = 0$), $\mathcal{V}_{1w}$ is obtained by integrating (49) southward from y_2. Since $g'(y_2) = 0$, the northern boundary condition is $\mathcal{V}_{1w}(y_2) = 0$. The coastal layer thickness is calculated by back-solving (50) for h_w.

3.2.1.5 Final adjustment: When the eastern-boundary Rossby-wave front finally arrives at the western boundary, h_w^+ deepens to (47), and U_{1w}^+ is canceled out, which was draining water from the western-boundary region. With $U_{1w}^+ = 0$, the western-boundary-current transport also vanishes (compare Eq. 49), and it follows from (50) that $h_w = h_w^+ = h_e$

after the Rossby-wave front has crossed the basin at all latitudes (Figure 4, bottom-right panel; Stage 4).

3.2.2 Steady state: In steady state, then, the upper-layer thickness has adjusted to (47), and the depth-averaged flow has vanished throughout the entire basin. Thus, the steady-state circulation does not have an MOC. An explanation for why the model *has* to adjust to a no-MOC state is as follows: Necessary ingredients for establishing an MOC are processes that transfer water from one layer into the other in *both* directions. Since w_d is excluded, water can only be detrained in the northern basin by w_c. The interior flow and the meridional component of western-boundary current, however, are geostrophic by definition. Since $g'(y_2) = V_2(y_2) = 0$, $w_c = 0$ as well. Consequently, the MOC cannot be closed in the north, regardless of the circulation farther to the south.

3.2.3 Conclusions: The existence of this no-MOC solution suggests the possibility that a poleward, surface-density gradient need not drive any diapycnal overturning at all! Indeed, if the real ocean can reach this state, there is no relationship between the meridional pressure difference and MOC strength. This property, of course, contradicts numerous results from similar, idealized modeling studies using OGCMs, which do generate diapycnal overturning cells (see Section 1). One or more of the processes neglected in obtaining this no-MOC solution is thus essential for establishing the overturning.

3.3 Solutions with overturning

When mixing (w_d) is included in w_1, VLOM adjusts to a solution with an MOC. Velocity w_d requires layer-1 water to detrain into layer 2, which in steady state has to be balanced by entrainment into layer 1 via w_s or w_m, thereby generating the descending and ascending branches of the model MOC.

3.3.1 Spin up: The spin-up of the MOC solution follows essentially the same steps as that for the no-MOC solution described in Section 3.2.1. Figure 6 shows a schematic of the stages of the spin-up. The initial response (Stage 1) and Kelvin-wave adjustment (Stage 2) for the present solution are identical to those for the no-MOC solution: State (45)

is established across the interior ocean (Stage 1); then, coastal Kelvin waves adjust h_e to (47), and a temporary boundary current and/or local detrainment develop at the western boundary, as described in Section 3.2.1.4 (Stage 2).

Subsequently, the response in the interior ocean is altered from the no-MOC spin-up, because the eastern-boundary Rossby waves that adjust the interior ocean are damped by w_d near y_2 (Stage 3). Specifically, the interior response is determined by (26) with $w_1 = w_d$, that is,

$$h_{1t} + c_r h_{1x} = w_d = -\frac{h_1 - h_{\max}}{t_d}\theta(h_1 - h_{\max}), \tag{53}$$

where the Rossby-wave speed is given by (48). According to (53), there exists a region where $h_1 < h_{\max}$ (Region 1), where Rossby waves can still cross the basin undamped to deepen h_1 to h_e. That region lies south of a y'', which is defined by $h_e(y'') = h_{\max}$. In the region, $y'' < y \leq y_2$ (Region 2), $h_1 > h_{\max}$ and hence w_d is active. After the passage of the eastern-boundary Rossby wave, h_1 is adjusted to the steady-state balance

$$h_{1x} = -\frac{h_1 - h_{\max}}{c_r t_d}, \tag{54}$$

in which h_1 rises monotonically to the west since $c_r < 0$. Due to this Rossby-wave damping, an eastward, interior flow remains after the passage of the Rossby-wave front in Region 2, so that $U_{1w}^{+}(y \geq y'') \neq 0$. As a result, the western-boundary current is not canceled out in the final stage (Stage 4).

3.3.2 Steady state:

South of y'' (Region 1), $h_1 = h_e$ given by (47) in the steady state, so that $U_1 = V_1 = 0$ and there is no across-layer transport ($w_1 = 0$). In contrast, north of y'' (Region 2) h_1 shoals away from the eastern boundary according to (54).

The exact solution to (54) that satisfies the boundary condition $h_1(x_e) = h_e$ is

$$\frac{1}{2}\left[\frac{\beta g'}{Df^2} + \frac{g'_y}{2Df}\right]\left(h_e^2 - h_1^2\right) + \left[-\frac{\beta g'}{f^2}\left(1 - \frac{h_{\max}}{D}\right) + \frac{g'_y h_{\max}}{2Df}\right]\left[(h_e - h_1) + h_{\max}\ln\frac{h_e - h_{\max}}{h_1 - h_{\max}}\right] = -\frac{x_e - x}{t_d}, \tag{55}$$

an implicit equation that has to be solved iteratively for $h_1(x)$. Since h_1 is known in the interior ocean so are the (geostrophic) transports, U_1 and V_1, and the across-interface velocity

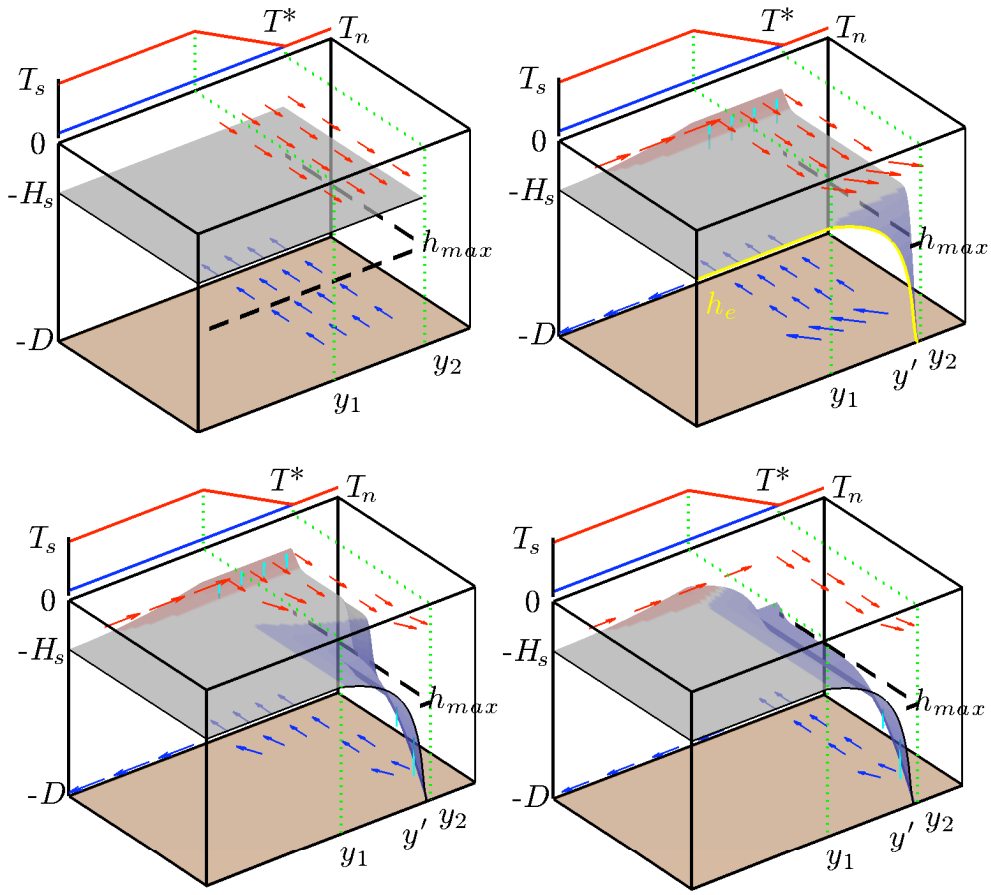

Figure 6: Schematic plot of the spin-up of the VLOM solution with mixing (w_d) and without winds illustrating the response during the initial adjustment (Stage 1; top-left), just after the eastern-coastal adjustment (Stage 2; top-right), during the Rossby-wave adjustment (Stage 3; bottom-left), and the final, steady steady-state (Stage 4; bottom-right).

w_1. In Region 2, they are

$$U_1 = -\frac{D-h_1}{2fD}\left(g'h_1^2\right)_y, \quad V_1 = \frac{D-h_1}{2fD}\left(g'h_1^2\right)_x, \quad w_1 = -\frac{h_1-h_{\max}}{t_d}, \qquad y > y'', \quad (56)$$

where h_1 is given by (55). A solution with $H_s = 300$ m, $h_{\max} = 800$ m, and $t_d = 100$ days, is plotted in Figure 7. It shows that h_1 rapidly approaches $h_{\max}$ near the eastern boundary in Region 2, where the resulting zonal pressure gradient drives a northward, converging (recall that w_d is proportional to $h_1 - h_{\max}$) flow. As h_1 is then close to $h_{\max}$ farther away from the boundary, the eastward transports are near constant and non-diverging in the interior of the basin.

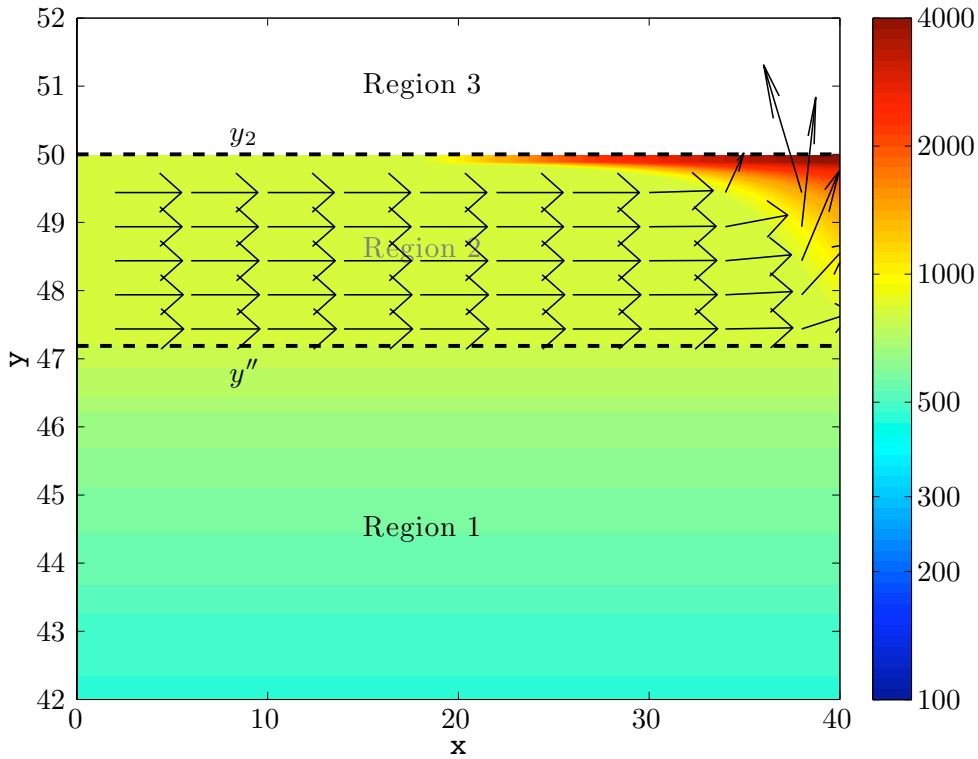

Figure 7: Horizontal map of interior ocean layer-1 thickness h_1 (shading) and horizontal transports $\boldsymbol{V}_1$ (vectors) for VLOM solution without winds with $H_s = 300\,\mathrm{m}$, $h_{\max} = 800\,\mathrm{m}$ and $t_d = 100\,\mathrm{days}$.

As (55) is relatively difficult to interpret due to its complex structure, an approximation to (55),

$$h_1 = h_{\max} + (h_e - h_{\max}) \exp \frac{x_e - x}{c_r t_d}, \tag{57}$$

is also given, which neglects variations in wave speed due to the shoaling of h_1 ($c_{rx} = 0$). It illustrates the dependency of the Rossby-wave decay scale on c_r and the damping timescale t_d, showing that $t_d \ll L_x/c_r$, where L_x is the width of the basin, in order for h_1 to be damped to $h_{\max}$ within the basin. In that case, $h_{\max}$ is effectively the value of h_1 at x_w^+, which constitutes the boundary of Region 2 and the western boundary layer. That is,

$$h_w^+ = h_{\max} \qquad \text{as} \qquad y_w'' \le y \le y_2, \tag{58}$$

where y_w'' is the latitude where y'' intersects with x_w^+. Relation (58) is assumed to hold in all the solutions presented in this manuscript, even for the solutions with winds in Section 5.3,

because it allows for a simple form of U_{1w}^{+} as well as a convenient measure for the strength of Rossby wave damping, $h_{\max}$. In the present solution, using (58) yields

$$U_{1w}^{+} = \frac{g_y'}{2f} h_{\max}^2 \frac{D - h_{\max}}{D} \qquad \text{as } y'' \leq y \leq y_2, \tag{59}$$

and the zonally integrated northward transport in Region 2 (excluding the flow in the western boundary current) is

$$\mathcal{V}_{1in} = \int_{x_w^+}^{x_e} V_1 \, dx = \frac{g'}{2f} \left[h_e^2 - h_{\max}^2 - \frac{2}{3D}(h_e^3 - h_{\max}^3) \right]. \tag{60}$$

Note that $w_c = 0$, because $V_1(y_2)$ and $\mathcal{V}_{1in}(y_2)$ are both proportional to $g'(y_2) = 0$. In steady state, the total amount of detrainment in Region 2 is given by

$$\mathcal{W}_d \equiv \iint_{\mathcal{A}_2} w_1 \, dA = -\oint_{R_2} \boldsymbol{V}_1 \cdot \boldsymbol{d\ell} = -\int_{y_w''}^{y_2} U_{1w}^{+} \, dy = -\frac{g_s'}{2\bar{f}} H_s^2 \underbrace{\left(1 - \frac{h_{\max}}{D}\right)}_{\equiv C_{\max}}, \tag{61}$$

where $\mathcal{A}_2$ is the area of Region 2, R_2 is the perimeter of Region 2, and $\boldsymbol{d\ell}$ denotes a differential arc length pointing in an anticlockwise direction around Region 2. The change from the second-to-third term in (61) follows from mass conservation and the divergence theorem of vector calculus. The change from the third-to-fourth term follows because the flows across the southern boundary y'', the northern boundary y_2, and the eastern boundary x_e all vanish. The final step follows from (59) and the relation $g'(y'')h_{\max}^2 = g_s' H_s^2$, which follows from the definition of y'' and (47). The variable $\bar{f}$ is an average of the Coriolis parameter along the eastern boundary of Region 2, defined by $\bar{f}^{-1} = [1/g'(y_w'')] \int_{y_w''}^{y_2} \left(g_y'/f \right) \, dy$. Finally, the nondimensional parameter $C_{\max}$ is defined to underscore the similarity of (61) and (1).

When the eastern-boundary Rossby waves reach the western-boundary region (x_w^+), they only cancel U_{1w}^{+} south of y'', where h_w^+ is adjusted to h_e. North of y'', however, $h_w^+ = h_{\max}$ (see equation 58), so that U_{1w}^{+} is given by (59) and the western-boundary current is not canceled out in the final state. The solution of the steady-state western-boundary layer is determined by the same physics as the temporary solution, and can be solved analogous to Section (3.2.1.4), as follows:

Case $\boldsymbol{h}_{\max} \geq \hat{\boldsymbol{H}}$: In the final state, there is no western-boundary entrainment near y_2 if $h_{\max} > \hat{H}$ (see equation 52). In that case, V_{1w} is obtained by integrating (49) southward

from y_2 with $V_{1w}(y_2) = 0$ and $W_m = 0$. South of y'', where $U_{1w}^+ = 0$, the western boundary current remains constant and its value is given by (61). Equation (50) can be solved for $h_w(y)$.

In contrast to the intermediate western-boundary-current solution, there can be a second entrainment region just north of y_1, because $h_w^+(y < y'') = h_e(y)$ shoals towards the south and $\mathcal{V}_{1w}$ depends on the difference of h_w^+ and h_w. Thus, h_w also tends to decrease towards y_1, and western-boundary adjustment processes attempt to lift up h_w even higher than $z = -h_{\min}$ if $\mathcal{V}_{1w}(y'')$, given by (61), is greater than the maximum western-boundary-current transport that can be maintained by the model at any latitude

$$\tilde{V}_{1w} = \frac{g'}{2f}\left[h_e^2 - h_{\min}^2 - \frac{2}{3D}(h_e^3 - h_{\min}^3)\right], \tag{62}$$

which is given by (50) with h_w taking its minimum value $h_{\min}$. Within the entrainment region, that (if it exists) extends southward to y_1, it follows then that $h_w = h_{\min}$ and $\mathcal{V}_{1w}$ is given by (62). $W_m = 0$ to the south of y_1, so that $\mathcal{V}_{1w} = \mathcal{V}_{1w}(y_1)$, and h_w is determined as before.

Case $\boldsymbol{h}_{\max} < \hat{\boldsymbol{H}}$: In this case, the solution starts as in the $H_s > \hat{H}$ case described in Section (3.2.1.4) and then continues south of y_e as described above with $\mathcal{V}_{1w} = \mathcal{V}_{1w}(y_e)$.

Following these steps, $\mathcal{V}_{1w}(y)$ and $h_1(y)$ can be determined at each latitude. As in the temporary western boundary layer solution, the circulation is finally closed by upwelling via w_s near y_s, so that the solution is complete.

3.3.3 Comparison to similar solutions: The development of an MOC upon the inclusion of w_d into VLOM suggests that the underlying mixing processes and the resulting Rossby-wave damping in Region 2 are key processes to generate an upper-layer flow convergence into the regions where deep water is formed. In the present study, it is argued that Region 2 simulates a boundary layer adjacent to y_2 in MITgcm (see Chapter 4.3). One might argue from a more technical point of view, however, that the mixing-parameterization (w_d) introduces a boundary layer along the eastern boundary, because w_d acts along zonal Rossby-wave characteristics. Such boundary layers have been explored in previous studies:

In the study of Pedlosky and Spall (2005), the relaxation of layer thickness primarily represents surface cooling in the interior ocean (see Section 1.1.4). Their results are similar to the solution presented above, because deep water is also formed essentially by surface cooling. A difference is, however, that surface cooling is not directly related to interior-ocean Rossby-wave damping in the VLOM solution, as the water is cooled to temperature near T_n in the western boundary current before it turns eastward in Region 2. Consequently, a comparatively small surface heat-flux is associated with the final water-mass transformation near the eastern boundary.

Cessi and Wolfe (2009) consider a boundary layer where density is mixed by eddies as the eastward surface flow converges, and hence water sinks, near the eastern boundary. These processes are not considered in VLOM, where the eastern-boundary density structure adjusts such that the depth-integrated flow vanishes (Equation 47), and hence an implicit assumption is that water sinks isothermally in an eastern boundary layer (see next section).

3.4 Thermal-wind circulation

The preceding solutions can be extended to include the shear part of the thermal-wind flow in layer 1, which does not vanish in steady state. In the interior ocean, the shear flow is given by the term in (24) proportional to $(z + h_1/2)$. In solutions with $w_d = 0$, where $h_1 = h_e$ is valid across the entire ocean basin (and in solutions with $w_d \neq 0$ at the eastern boundary), the depth-averaged part of the flow vanishes, but the shear part does not vanish in (24), as shown in the left panel of Figure 8. Since the eastern-boundary condition is $u_1(x_e, z) = 0$, however, water has to sink isothermally to close the thermal-wind circulation in regions where $g'_y < 0$. Since the flow within the layer is assumed to be geostrophic, there is no physics that can set a scale for a finite-width boundary layer, in which the vertical motion occurs. Thus the vertical velocity $w \to \infty$ at the boundaries, and it is clear that planetary geostrophy has to break down in a more realistic model to allow for an eastern boundary layer.

Even without specifying the structure of that boundary layer, however, the vertical transports/width, $W_e(y, z)$, follow from continuity (that is, if the divergence of the alongshore flow

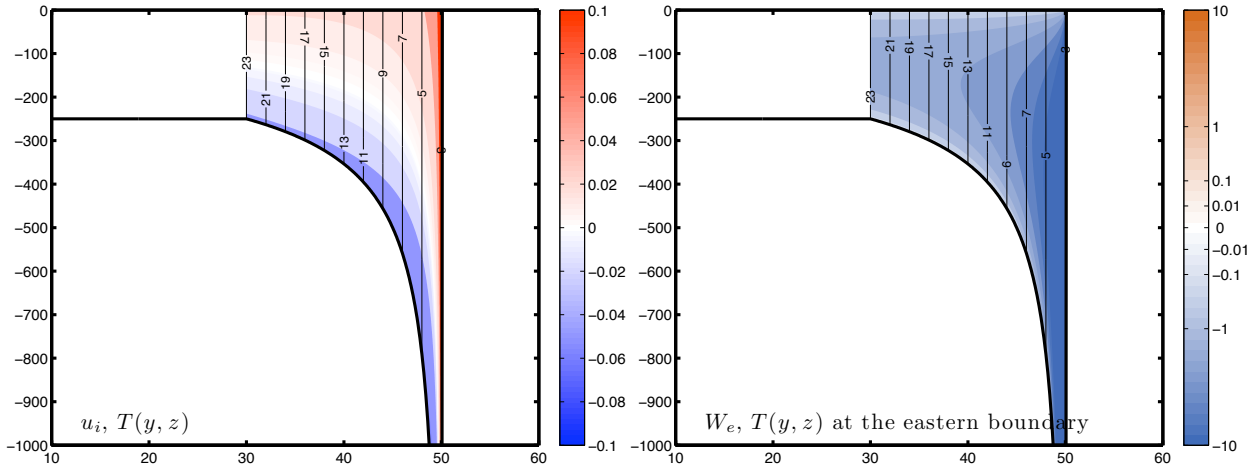

Figure 8: Meridional section of depth-dependent, zonal velocities in the interior ocean (shading, left panel) and eastern boundary sinking transport/width W_e (shading, right panel), for the VLOM solution without winds and with $H_s = 250\,\mathrm{m}$, $D = 4000\,\mathrm{m}$ and $w_d = 0$. Contours indicate temperature.

in the boundary layer is neglected), and are well defined and finite. An example is shown in the right panel of Figure 8. The maximum sinking transport/width at the eastern boundary occurs at a depth of $z = -h_e/2$ and is given by

$$W_e(y) \equiv \int_{x_e-\Delta x}^{x_e} w(-h_e/2)\,dx = -\int_{-h_e/2}^{0} u_1(x_e-\Delta x)\,dz = \frac{g'_y}{8f}h_e^2, \qquad @\ z = -\frac{h_e}{2}, \quad (63)$$

where the distance Δx is assumed to be large enough so that $x_e - \Delta x$ is to the west of the eastern boundary layer. It is noteworthy that (63) corresponds exactly to the eastern-boundary sinking found in OGCMs, as described by Spall and Pickart (2001). Since it is identical in the solutions with and without an MOC, it follows that the sinking is not directly related to the diapycnal overturning circulation. On the other hand, in the MITgcm solutions, the thermal-wind sinking does affect the eastern-boundary density structure, as we shall see in Section 4.

3.5 Overturning strength

In this section, we first derive a measure for the strength of the MOC in VLOM forced by buoyancy forcing only, $\mathcal{M}_n$, and report its sensitivity to model parameters. We conclude with a discussion of limitations of our definition of $\mathcal{M}_n$.

3.5.1 Overturning transport, $\mathcal{M}_n$: As a measure for the strength of overturning, $\mathcal{M}_n$ is defined to be the integral of all the water that crosses the layer interface from layer 1 into layer 2 in the northern part of the basin via w_c and w_d, that is,

$$\mathcal{M}_n \equiv -\mathcal{W}_d - \mathcal{W}_c, \tag{64}$$

where $\mathcal{W}_c = \int_{x_w}^{x_e} \int_{y_s}^{y_n} w_c \, dy \, dx = -\int_{x_w}^{x_e} V_1(y_2) \, \theta \left[V_1(y_2)\right] \, dx$ and $\mathcal{W}_d$ is defined in (61). Since $\mathcal{W}_c = 0$ for all solutions discussed in this Chapter, (64) reduces to $\mathcal{M}_n = -\mathcal{W}_d$. Furthermore, because the western-boundary entrainment via w_m vanishes or is small for most solutions (see Sections 3.2.1.4 and 3.3), most water entrains in the southern sponge layer at $y \leq y'_s$, and so $\mathcal{M}_n$ is indeed a good measure for the overall overturning strength throughout the basin.

Black curves in Figure 9 plot $\mathcal{M}_n$ vs. H_s for constant $C_{\max}(h_{\max})$. According to (61), $\mathcal{M}_n$ $(= -\mathcal{W}_d)$ then depends linearly on H_s^2 to first order, as does the MOC scaling for OGCMs (1). Since $\bar{f}$ also (slightly) depends on H_s, the exact relation is more complex than quadratic, as indicated by the thin line (very close to the thicker solid line) in Figure 9 where $f(y_2)$ instead of $\bar{f}$ is used to compute an approximation for $\mathcal{M}_n$.

The red curve in Figure 9 indicates $\mathcal{M}_n(H_s)$, when y'' (and hence the width of the boundary layer $L_{bl} = y_2 - y''$) is kept constant, and $h_{\max}$ is set to $h_e(y'')$, that is

$$h_{\max}(H_s) = \sqrt{\frac{g'_s}{g'(y'')}} H_s, \qquad \text{as } y'' < y', \tag{65}$$

where (47) was used. The difference between the red (constant L_{bl}) and black (constant $h_{\max}$) curves illustrates that $\mathcal{M}_n$ also depends on the strength of the Rossby-wave damping. Since it is not clear at that point, what processes w_d represents precisely, any assumption on $h_{\max}$ or L_{bl} is somewhat arbitrary, and the red and black curves both represent equally valid VLOM results. As we shall see in Chapter 4, however, assuming L_{bl} to be constant appears to be a reasonable choice to model northern boundary processes in the MITgcm.

3.5.2 Limitations of the results: A limitation of the present solutions is that the buoyancy forcing is so strong (*i.e.*, $\delta t \to 0$), that temperature advection does not feed back on the meridional temperature difference, and thus the strength of the MOC, as has been found

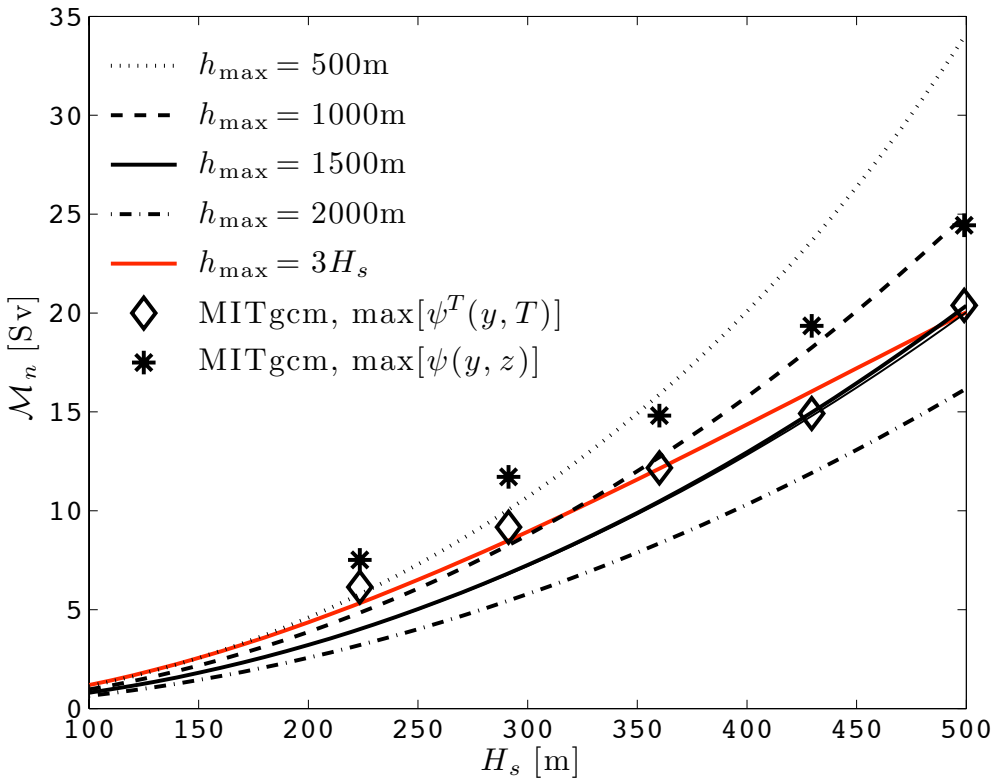

Figure 9: Curves of $\mathcal{M}_n(H_s)$ for VLOM solutions without winds. The black, thick curves correspond to different but constant values of $h_{\max}$, namely 500 m (··), 1000 m (–) and 1500 m (-) 2000 m (-·), whereas the thin solid line (almost indistinguishable from the thick solid line) corresponds to $\mathcal{M}_n(H_s)$ with $h_{\max} = 1500$ m, where $f(y_2)$ is used in (61) instead of $\bar{f}$. The red curve shows $\mathcal{M}_n(H_s)$, with $h_{\max} = 3H_s$, which corresponds to a fixed boundary layer width of 200 km. Also included are data points from several MITgcm solutions without winds, where diamonds correspond to the maxima of $\phi^T(y,T)$, and stars to the maxima of $\phi(y,z)$.

to be important in previous studies (*e.g.,* Stommel, 1961; Park and Bryan, 2000). Exploring these processes in detail is beyond the scope of this manuscript. A noteworthy property of the steady-state solutions, however, is that they are only sensitive to $T_1(x,y)$, and not to the processes by which T_1 is determined. It follows that even if surface temperature advection were thermodynamically important in VLOM, and the meridional density difference was given by $\tilde{\rho}_n - \tilde{\rho}_s$, where $\tilde{\rho}_s$ ($\tilde{\rho}_n$) was the warmest (coldest) water actually formed at the surface, and the deep ocean was filled up with water of the density $\tilde{\rho}_n$, a relation similar to (61) would still hold with a modified (smaller) $\tilde{g}'_s = g(\tilde{\rho}_n - \tilde{\rho}_s)/\tilde{\rho}_n$.

Another implicit assumption in the VLOM equations and the derivation of $\mathcal{M}_n$ is that

the deep ocean is filled by the coldest surface water formed in the basin. This assumption is sensible when the MOC extends into Region 3, where that water is formed in VLOM. As shown in the solutions in this chapter, however, the geostrophic flow cannot extend to the north of y_2 ($w_c = 0$ for all solutions), which somewhat constraints the participation of the coldest surface water in the MOC. On the other hand, most water detrains close to y_2 at temperatures not much warmer than $T_n = 3°$C in VLOM. For the solution shown in Figure 7 with $\mathcal{M}_n = 9.5$ Sv, 5.7 Sv are detrained at temperatures $< 3.2°$C and the average temperature of detrained water is 3.28°C for example, so that the deep ocean is not heated much. But still one can argue that the processes parameterized by w_d have to include either temperature mixing or advection by a non-geostrophic flow, to prevent the deep ocean from heating up.

Although the solutions discussed in this chapter are limited to the case where the surface temperature zonally uniform, they can be easily extended to allow for the surface temperature to be variable in the zonal direction as well. Equation (47) then determines the layer thickness along the eastern and northern wall, and interior layer thickness is derived by integrating the steady-state version of (26) along Rossby-wave characteristics. It follows from the right-hand side of (26) that h_1 still adjusts to (47) in the interior ocean where $w_d = 0$, so that the detrainment and flow into Region 2, where $w_d < 0$ can be computed by an integral similar to (61). It follows that $\mathcal{M}_n$ differs then only by the value of $\bar{f}$, if T^* reaches T_n anywhere at the eastern or northern boundary.

CHAPTER 4

MITgcm solutions forced by differential heating

Following the organization of Chapter 3, solutions to MITgcm are reported first without an MOC (Section 4.1) and then with one (Section 4.2). The former is a conceptual solution to a reduced set of equations and the latter a numerical solution with full physics. The dynamics of a northern boundary layer, where water detrains in the solution with an MOC similar as in VLOM, is discussed in Section 4.3, and the strength of the model MOC and its sensitivity to the thermocline thickness in Section 4.4. Throughout, similarities and differences are noted between the MITgcm solutions and their VLOM counterparts.

4.1 Conceptual response without overturning

Consider an idealized version of the MITgcm in which the momentum-advection and mixing terms are dropped, except for weak viscosity ($\nu_h \to 0$) to allow for viscous boundary layers. Furthermore, assume that $\delta t \to 0$ in Q so that $T = T^*$ for $z \geq h_{\min}$, and that the model is initialized with a layer-like density structure such that $\rho(z) = \tilde{\rho} = \rho^*$ at $z \geq -h_{\min}$, and $\rho(z) = \rho_n$ below, both in the sponge layer as well as the interior ocean. Since the barotropic mode adjusts quickly, the momentum equations are essentially given by (24). Geostrophy has to break down at the boundaries where (24) does not vanish, and the circulation is closed in viscous boundary layers. As temperature advection within these

boundary layers can feedback on the density field (a process that is not included in VLOM), solutions can potentially be different from their VLOM counterparts.

It is impossible to obtain analytic solutions that allow for temperature advection in the boundary layers. So, the solution is derived as follows: First, the spin-up and steady-state responses are discussed in the interior ocean assuming that $\nu_h = 0$. Then, solutions for the viscous boundary layers in the final state are reported, first for meridional and then for zonal boundary layers. Each boundary layer solution is followed up by a discussion of the impact of temperature advection and potential feedback mechanisms.

4.1.1 Thermocline adjustment and interior-ocean, steady-state response: With these model restrictions, the spin-up stages are theoretically the same as those illustrated in Figure 4, except including thermal-wind shear. Since the idealized MITgcm neglects vertical diffusion, the density jump in between the layers remains throughout the spin-up, so that the terms "layer" and "layer interface" can be used to describe the density field in the following discussion.

4.1.1.1 Interior response: After the barotropic waves have canceled the depth-integrated transport (Stage 1), the layer-1 ($z \geq -h_{\min}$) response in the interior ocean is given by (24) with $h_1 = h_{\min}$, that is

$$u = \frac{g\rho_y^*}{f\rho_n}(z + h_{\min}) - \frac{g\rho_y^*}{2f\rho_n}\frac{h_{\min}^2}{D}, \quad v = w = 0, \quad T = T^*(y), \qquad z \geq -h_{\min}. \tag{66}$$

According to (66), the layer-1 zonal flow consists of an eastward current proportional to $(z + h_{\min})$ due to the thermal wind plus a westward, depth-independent current due to the compensating barotropic response; as a result, there is weak westward flow near the bottom of the layer in layer 1, but the net layer-1 transport is eastward. The layer-2 ($z < -h_{\min}$) flow is (66) without the z-dependent (thermal-wind) part of u and with $T = T_n$. As in VLOM, the convergence of warm, upper-layer water generates downwelling at the eastern boundary. The western-boundary divergence brings cool water to the surface, where it is immediately warmed to T^* by Q; as a result, the layer interface remains at $z = -h_{\min}$, and essentially layer-2 water is entrained into layer 1, as is done by w_m in VLOM.

Subsequently, the thickening of h_1 at the eastern boundary is arrested by the arrival of

coastal Kelvin waves from the south (Stage 2); they adjust $h_1(x_e, y)$ to $h_e(y)$ defined in (47) with $H_s = h_{\min}$, thereby ensuring that the depth-integrated, geostrophic flow into the coast vanishes. Rossby waves then carry h_e across the basin (Stage 3), and when they reach the western boundary, the ocean is adjusted to steady state (Stage 4).

In the interior ocean, the steady-state solution in layer 1 is

$$u = \frac{g\rho_y^*}{f\rho_n}\,(z + \frac{1}{2}h_e), \quad v = w = 0, \quad T = T^*(y), \qquad z \geq -h_e, \tag{67}$$

and the layer-2 response is a state of rest with $T = T_n$. Note that, in contrast to (66) the thermal wind now has equal eastward and westward branches. As discussed next, these branches are joined isothermally by downwelling (upwelling) within a meridional Ekman layer at the eastern (western) boundary.

4.1.2 Meridional boundary layers:

To obtain a solution for the flow field in a meridional Ekman layer, where density advection is neglected, we consider the steady-state response to equations

$$-fv = \nu_h u_{xx}, \tag{68a}$$

$$fu = \frac{g\rho_y^*}{\rho_n}\left(z + \frac{h_e}{2}\right) + \nu_h v_{xx}, \tag{68b}$$

$$u_x + w_z = 0, \tag{68c}$$

where derivatives with respect to y are dropped, a simplification that assumes the width of the layer is much less than the length scale of alongshore variations. The pressure terms are absent from (68) because the density field is assumed to have adjusted to the eastern-boundary structure (47), so that the flow in the interior ocean consists only of a zonal, upper-layer, thermal-wind shear.

For notational convenience, let the eastern boundary of the basin be located at $x = 0$, then solutions to (68) are subject to the boundary conditions

$$u = v = 0 \quad \text{at} \quad x = 0. \tag{69}$$

The solution to (68a) and (68b) that satisfies (69) is

$$u = \frac{g\rho_y^*}{f\rho_n}\left(z + \frac{h_e}{2}\right)\left(1 - e^{-\gamma|x|}\cos\gamma x\right)\,\theta(-x), \tag{70a}$$

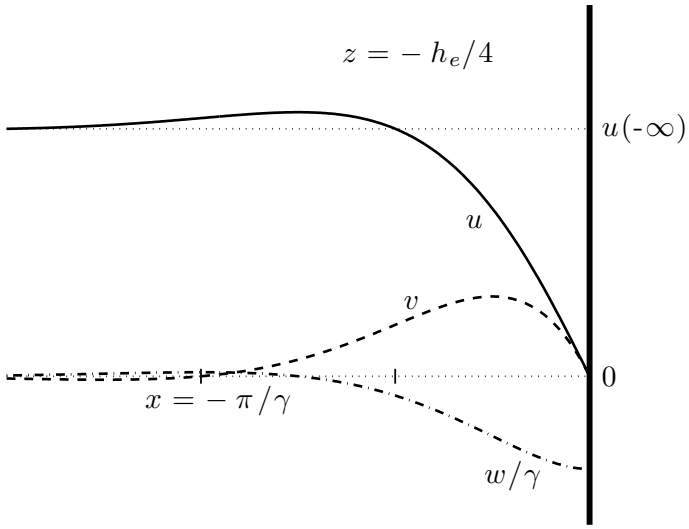

Figure 10: Velocities (70) in the meridional Ekman layer at the eastern boundary $x_e = 0$ and $z = -h_e/4$. The x axis and vertical velocity are scaled by a factor γ^{-1}.

$$v = -\frac{\nu_h}{f} u_{xx} = \frac{g\rho_y^*}{f\rho_n}\left(z + \frac{h_e}{2}\right) e^{-\gamma|x|} \sin\gamma|x|\, \theta(-x), \tag{70b}$$

and using (68c) gives

$$w = \gamma \frac{g\rho_y^*}{2\rho_n f} z\,(z + h_e)\, e^{-\gamma|x|}\,(-\cos\gamma x + \sin\gamma x)\;\theta(-x), \tag{70c}$$

where $\gamma = \sqrt{f/(2\nu_h)}$. The solution consists of an x-independent, zonal current in the interior ocean plus a meridional Ekman layer (compare Figure 10). The Ekman layer decays and oscillates away from boundaries with a width scale $L_E = \sqrt{2\nu_h/f}$, which for typical model parameters is very narrow (with $\nu_h = 2\times10^4$ m^2/s and $f = 10^{-4}$ s^{-1}, $L_E = 20$ km). It provides the vertical flow that joins the interior zonal currents.

At a western boundary, the solution corresponding to (70) can be obtained by substitution of $\tilde{x} = -x$ and $\tilde{y} = -y$. Solutions (70) as illustrated in Figure 10 are then valid for the western boundary as well, with u and w having the opposite direction as at the eastern boundary.

The preceding interior as well as the boundary-layer solutions ignore temperature advection. This neglect is reasonable for the interior response, since its flow field never crosses isopycnals, but there is an across-isopycnal flow in the boundary layers. What, then, is the impact of temperature advection on them?

Consider the impact on the eastern-boundary layer. Since the upper-layer density field varies only meridionally and w vanishes at the bottom of layer 1, the zonal and vertical density advection terms are initially identically zero, so here only the impact of v is considered.

The meridional current v (70b) associated with the Ekman layer has its maximum amplitude occurring at $|x| = (\pi/4)\, L_E$. At this longitude, its value is about half (0.46) times that of the interior zonal flow, so that the current advects warmer water in the upper half of the layer to the north and colder water in the bottom half to the south. On the other hand, the transport of the boundary current,

$$V = \int_{-\infty}^{0} v\, dx = \sqrt{\frac{2\nu_h}{f}} \left(z + \frac{h_e}{2} \right) \frac{g\rho_y^*}{\rho_n f}, \tag{71}$$

is proportional to $\sqrt{\nu_h}$, so that the alongshore transport vanishes in the limit $\nu_h \to 0$. The vertical velocities (70c) are proportional to $\sqrt{\nu_h}^{-1}$, in contrast, so that the vertical transport/width is independent of ν_h (compare Equation 63). As the downwelling then keeps $\rho(z)$ near the surface value ρ^* throughout the upper layer as $\nu_h \to 0$, the solution is arguably stable at the eastern boundary.

Along the western boundary, the v (70b) field is the same as at the eastern boundary, and temperature advection associated with v effectively cools the bottom half of the layer. In contrast, w is directed upward. As a result, vertical advection does not counteract the cooling, but amplifies initial temperature perturbations by advecting relatively cool water from the bottom of the layer towards the surface.

Wave-adjustment processes are also different at the eastern and western boundaries. At the eastern boundary, Kelvin waves propagate northward. They adjust the layer thickness along the boundary to eliminate the alongshore gradient in depth-integrated, upper-layer pressure, with the southern layer thickness H_s serving as boundary condition (compare Equations 41 and 47). At the western boundary, on the other hand, Kelvin waves propagate towards the equator. As no baroclinic waves exist in the northern, homogenous ocean, a boundary condition analogue to H_s is not well specified. Furthermore, western-boundary-layer dynamics allow for geostrophic, alongshore boundary currents, so that Kelvin waves no longer need to cancel out the depth-integrated, upper-layer pressure gradient, once a zonal density difference is established. This alongshore current provides a further, important, pos-

itive feedback mechanism, as its transport, and hence the strength of meridional advection, are proportional to the zonal pressure gradient and independent of ν_h.

For these reasons, the no-MOC solution is much more likely to be unstable at the western than at the eastern boundary. This is in agreement with the results of numerical spin-down experiments discussed in Schloesser et al. (2011). In these experiments the density and velocity fields are initialized to the no-MOC solution. When the model is started, the no-MOC solution collapses much faster at the western boundary than everywhere else.

4.1.3 Zonal boundary layers:

Zonal viscous boundary layers are present in the solution at y_2, for example, because in (67) the thermal-wind velocities are finite the south and zero to the north of y_2. As for the meridional Ekman layer, we neglect temperature advection to derive the flow field in the zonal Ekman layer.

Consider the steady-state response to the x-independent set of equations

$$-fv = \nu_h u_{yy}, \tag{72a}$$

$$fu = -\frac{g\rho_y^*}{\rho_n}\left(z + \frac{D}{2}\right) + \nu_h v_{yy}, \tag{72b}$$

$$v_y + w_z = 0, \tag{72c}$$

where the thermal-wind shear in layer 1 extends to the bottom at $y \leq y_2$, and vanishes for $y > y_2$ because $\rho_y^* = 0$.

It is convenient to find solutions separately in the regions, $y > y_2$ and $y < y_2$, and to set $y_2 = 0$. Then, solutions to (72) are sought that are bounded as $y \to \pm\infty$ and that satisfy the matching conditions

$$u,\ u_y,\ v,\ \text{and } v_y \text{ are continuous at } y = 0. \tag{73}$$

With the restriction that f is constant, valid because the Ekman layer is so narrow, the solution to (72a) and (72b) is

$$u = -\frac{g\rho_y^*}{2f\rho_n}\left(z + \frac{D}{2}\right)\left[2\,\theta(-y) \mp e^{-\gamma|y|}\cos\alpha y\right], \qquad y \lesseqgtr 0, \tag{74a}$$

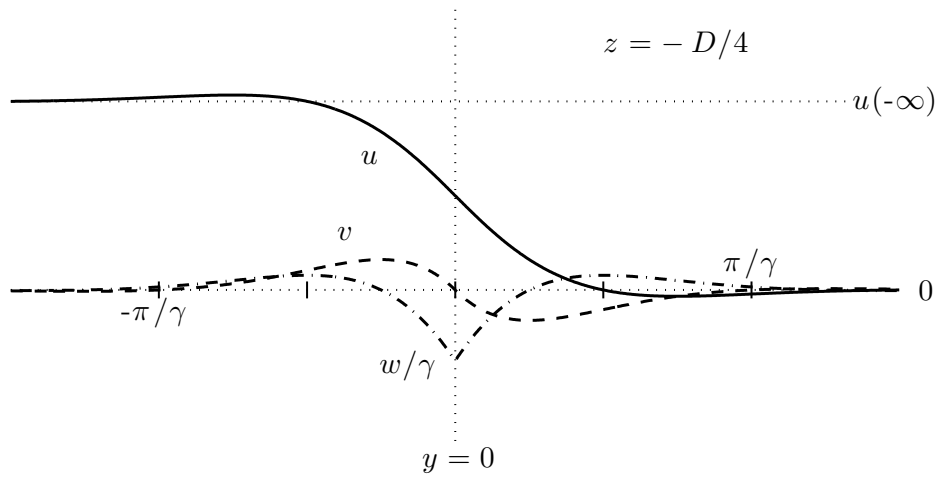

Figure 11: Velocities (74) in the zonal Ekman layer at $y_2 = 0$ and $z = -D/4$. The y axis and vertical velocity are scaled by a factor γ^{-1}.

$$v = -\frac{g\rho_y^*}{2f\rho_n}\left(z + \frac{D}{2}\right)e^{-\gamma|y|}\sin\gamma y, \tag{74b}$$

and then (72c) gives

$$w = \gamma\frac{g\rho_y^*}{2f\rho_n}z\left(z + \frac{D}{2}\right)e^{-\gamma|y|}\left(-\sin\gamma\,|y| + \cos\gamma y\right). \tag{74c}$$

The solution has two parts: a y-independent, zonal, thermal-wind-shear flow for $y \leq 0$; and a y-dependent, zonal Ekman layer (compare Figure 11). Velocities w and v form two, primary, counter-rotating cells, with downwelling and upwelling branches that attain their maximum values at $y = 0$ and $y = \pm\,\pi/(2\gamma)$, respectively. There are also secondary cells for larger $|y|$, but much weaker because of the exponential decay of amplitude.

In the boundary-layer solution presented above, temperature is constant in the x and z-directions, and for $y > y_2$. It follows that only temperature advection by v in (74b) initially perturbs the temperature field for $y < y_2$. As for the meridional Ekman layer, v is finite, but oscillates and decays with the width-scale L_E. In the primary cell with the largest amplitude ($y_2 - \pi L_E < y < y_2$), v is northward in the upper and southward in the lower half of the water column. Hence meridional advection erodes the temperature field of the no-MOC solution near y_2, that is $T(z) = T^*$, by stratifying the bottom half of layer 1. Once the temperature field is eroded near y_2, the resulting meridional, baroclinic pressure gradient drives a narrow, eastward, geostrophic, upper-layer flow. Then, viscosity starts to

erode the no-MOC solution farther away from y_2 by smoothing and widening the initially narrow current. In the following, we investigate how that widening is arrested by Rossby-wave adjustment, and derive the width scale for the zonal Munk layer, in which these two processes are balanced.

For simplicity, the problem is formulated in a $1\frac{1}{2}$-layer model, which includes important physical processes in an idealized way. The set of equations for the $1\frac{1}{2}$-layer model considered here is

$$-fV_1 = -P_{1x} + \nu_h U_{1yy}, \tag{75a}$$

$$fU_1 = -P_{1y}, \tag{75b}$$

$$U_{1x} + V_{1y} = 0, \tag{75c}$$

where U_1, V_1 are the upper layer transports and $P_1 = \frac{1}{2}g'h_1^2$ is the depth-integrated, upper-layer pressure. Equations (75) are essentially the VLOM equations (44) with the $1\frac{1}{2}$-layer-model approximation $D \to \infty$, and the commonly used zonal-boundary-layer approximations $U_{1yy} \gg U_{1xx}$ and that the zonal transports are geostrophic.

In order to obtain a single equation describing the boundary layer, we substitute the cross-differentiated (75a) and (75b) into (75c). Furthermore, we set $y_2 = 0$, use $\tilde{x} = x_e - x$, and assume that the width of boundary layer is much smaller than the radius of the earth. The resulting Munk-layer equation is then

$$\beta P_{1\,\tilde{x}} = \nu_h P_{1\,yyyy}. \tag{76}$$

It describes the balance between viscous effects that attempt to smooth P_1 (and the zonal geostrophic flow) in the meridional direction, and Rossby waves that attempt to cancel the zonal pressure gradient[5].

To apply the Munk-layer equation (76) to the present boundary-layer problem along y_2, we have to specify one boundary condition at the eastern boundary and four boundary conditions in y. The eastern boundary condition is determined by the eastern-boundary

[5]The exact equations describing that balance for a layer flow in VLOM as well as in MITgcm are more complex, since the depth-integrated, baroclinic pressure terms are no perfect differentials.

density structure (47), that is $P_1(x_e) = \frac{1}{2}g'h_e^2 = \frac{1}{2}g'_s H_s^2$ in the limit $D \to \infty$ considered here. Two of the meridional boundary conditions are far-field conditions, that eliminate solutions that are not bounded away from y_2. Outside of the boundary layer, P_1 is given by eastern-boundary structure in the no-MOC solution, and hence the far-field conditions are $P_1 = \frac{1}{2}g'_s H_s^2$ and $P_{1y} = 0$ as $y \to -\infty$. A third boundary condition is a solvability condition that ensures that h_1 remains finite at $y = y_2$, which in terms of P_1 requires that $P_1(y_2) = \frac{1}{2}g'h_1^2|_{y=y_2} = 0$ since $g'(y_2) = 0$. Finally, the fourth boundary condition is related to the erosion of the no-MOC solution by meridional temperature advection in the Ekman layer. For simplicity, we assume that this process specifies a function $h_n(x) = h_1(y_2)$, so that $P_{1\,y}(y_2) = \frac{1}{2}h_n^2 g'_y$.

With these boundary conditions given, it is straightforward to integrate (76) numerically. Here, we only discuss some general properties of the boundary layer, *i.e.*, the relation of its width to the viscosity ν_h. After substitution of $x' = (\tilde{x}\nu_h/\beta)^{1/4}$, (76) takes the form,

$$\frac{1}{4x'^3}P_{1\,x'} = P_{1\,yyyy}, \tag{77}$$

which is invariant to transformations $(x', y) \to \lambda(x', y)$. Solutions to (77), however, are not scale invariant in general, but for $h_n = 0$ ($h_n > 0$, and hence $P_{1\,y}(y_2) \neq 0$, introduces an additional length scale into the problem), one can find solutions of the form $P'_1(\phi)$ where $\phi = y/x'$. In that case (77) transforms to

$$\frac{1}{4}\phi P'_{1\phi} + P'_{1\,\phi\phi\phi\phi} = 0. \tag{78}$$

According to (78), solutions P'_1 are constant along lines $y = \phi x'$, where ϕ is any constant, and it follows that

$$L_M = \left(\frac{\nu_h}{\beta}(x_e - x)\right)^{1/4} \tag{79}$$

measures the meridional width scale of the zonal Munk layer. In a basin of finite width L_x, it then follows from (79) that the no-MOC solution is stable, since $L_M < (\nu_h L_x/\beta)^{1/4} \to 0$ in the limit $\nu_h \to 0$. Interestingly, however, a boundary layer with the characteristics of a zonal Munk layer is found in the numerical solution with finite ν_h presented in Section 4.2, suggesting that these processes are involved when the model develops an MOC.

4.2 Solutions with overturning

In this section, we discuss Q-forced solutions to the complete version of MITgcm (one that retains all mixing and advection terms). We start with a brief description of the spin-up, then we examine the steady-state response for a particular set of model parameters. Throughout, we discuss dynamical causes of solution's key features through a comparison to the VLOM response in Chapter 3 and other idealized models. A description of the experimental design, important model parameters and some details of the model integration are provided in Chapter 2.

4.2.1 Spin-up : The MITgcm is initialized at rest with $T = T_n$. When the buoyancy forcing is turned on, temperature quickly adjusts to T^* at the surface ($z > -h_{\min}$) and to $\tilde{T}$ within the sponge layer ($y < y_s'$). After barotropic waves have canceled the barotropic circulation, and the interior flow has (approximately) adjusted to a geostrophic balance, the interior flow at $y_1 < y < y_2$ is essentially as in the conceptual solution (Stage 1). Along y_s', strong zonal currents develop that are eastward near the surface and westward at depth because of the temperature difference between the sponge layer and the interior ocean (*i.e.*, the thickness of the warm upper layer is measured by (31) is H_s in the sponge layer, whereas it is $h_{\min}$ elsewhere). Subsequently, baroclinic Kelvin waves radiate along the eastern boundary, both north of y_1 as in the former solutions but also out of the sponge layer (Stage 2); in effect, the zonal currents generated by the sponge layer turn northward as an eastern-boundary current. Along the western boundary, Kelvin waves are triggered north of y_1 (compare Section 4.1.1) and near y_s', where the current along the northern margin of the sponge layer turns south, in the direction of Kelvin wave propagation. As Kelvin waves are quickly damped, by Q to the north of y_1 and by Q_D in the sponge layer, the circulation is closed by entraining layer-2 water into layer 1 in both regions. At the same time, diffusion starts to smooth the temperature jump at the bottom of the mixed layer, thereby deepening the upper layer until the arrival of the Rossby-wave front from the eastern boundary (Stage 3). After the eastern-boundary Rossby waves have arrived at the western boundary (Stage 4), the density and velocity fields continue to change more gradually, until mixing and advection are balanced.

4.2.2 Steady-state solution : In the following, the steady-state MITgcm solution for the parameters given in Chapter 2.3 is discussed in detail. The vertical temperature profile in the sponge layer, $\tilde{T}$, is given by (6) with $\Delta H_s = 100$ m, which, according to (43), gives $H_s = 223\,\mathrm{m}$. As for the VLOM solutions, we first examine the the density and velocity fields along the eastern boundary, then in the interior ocean and at the western boundary. Finally, we discuss the strength and structure of the MOC.

4.2.2.1 Eastern boundary: The top panels of Figure 12 plot the eastern-boundary temperature field and zonal velocities one grid point away from the boundary, and the vertical velocities at the boundary. Isotherms are nearly vertical above the red curve, which shows the theoretical mixed-layer thickness (40) derived by Sumata and Kubokawa (2001). The theoretical mixed layer extends to the ocean bottom at 49.94°N. The cyan curve shows h_1 given by (31), and its structure is very close to $h_e(y)$ in (47) for VLOM (compare Figure 8). Below the mixed layer, isotherms are almost horizontal. Zonal velocities are relatively large within the mixed layer in the region with a surface temperature gradient, and at least an order smaller elsewhere. Consistent with the thermal-wind shear, u decreases linearly with depth, and the flow is eastward in the upper half and westward in the lower half of the layer. w is downward in the mixed layer and the strongest sinking occurs near $y_2 = 50°$N. All these primary features of the temperature and flow field are very similar to those in the VLOM and conceptual MITgcm solutions, indicating that the eastern-boundary dynamics are dominated by Kelvin-wave adjustments in all the solutions.

The solution also exhibits some secondary features that are not explained by (40). The transition between the mixed layer and the deep ocean does not occur in a jump but rather in a diffusive "sublayer" with finite width. In addition, deep isotherms are not perfectly level, most noticeably for the 3.1°-isotherm, and there is *upwelling* below the mixed layer, most prominently where the mixed layer is deep. The existence of upwelling below the mixed layer and the finite thickness of the diffusive "sublayer" suggest that as a result of diffusion, Kelvin waves are slightly damped in the numerical MITgcm solution. Indeed, $h_1(x_e)$ is slightly deeper than the curve h_e given by (47), consistent with such damping. Similar damping and subsequent deepening of the layer interface along the boundary is also

reported for solutions with strong mixing in Kawase (1987). Recently, Schloesser et al. (2011) used a $2\frac{1}{2}$-layer model to argue that the strong diffusive mixing near the eastern boundary results from the eastern-boundary density structure.

4.2.2.2 Interior ocean: Figure 14 provides a x-y map of upper-layer thickness h_1 defined by (31) and upper-layer transport/width vectors $\boldsymbol{V}_1$ obtained by using h_1 in the geostrophic versions of the VLOM equations (44a) and (44b). Similarly as in VLOM, the interior-ocean h_1 deepens towards the north (compare Figure 7), because Rossby waves propagate the eastern-boundary density structure to the west. Furthermore, the strong, eastward band of $\boldsymbol{V}_1$ near $y_2 = 50°$N indicates, that Rossby-wave damping considerably reduces h_1 away from the eastern boundary, as in VLOM in Region 2. The dynamics of that northern boundary layer are discussed in more detail in Section 4.3.

To the south of the northern boundary layer (its southern boundary is indicated by the blue curve in Figure 14, indicating the longitude where h_{1x} changes sign), the upper layer thickens away from the eastern boundary. That upper-layer thickening is consistent with diffusion damping the Rossby waves, as in the layer model solution of Kawase (1987). Consequently, the flow field indicated by $\boldsymbol{V}_1$ also resembles that of the Stommel and Arons (1960) circulation.

The zonal sections in Figure 13 show that h_1 and the isotherms are almost level at 12°N, and southward flow of the surface branch of the Stommel-Arons circulation is distributed evenly across the upper ocean. At 30°N, the westward deepening is slightly more pronounced. In the sections at 35°N and 43°N and 48°N, isotherms concentrate at the bottom of the mixed layer at the eastern boundary, and spread towards the west. The spreading is so large that some of the isotherms slope upwards, although most isotherms deepen away from the eastern boundary. Consequently, there is a relatively strong southward flow at the bottom of the mixed layer. At 43°N, the slopes are relatively steep near the eastern boundary, and decrease to the west. As a result, h_1 is almost level west of 30°E. The strong stratification below the mixed layer at the eastern boundary is a consequence of the eastern boundary structure (40). As Rossby waves are much slower than the eastern-boundary Kelvin waves, the strong, vertical density gradient is quickly eroded by diffusion, when Rossby waves propagate away

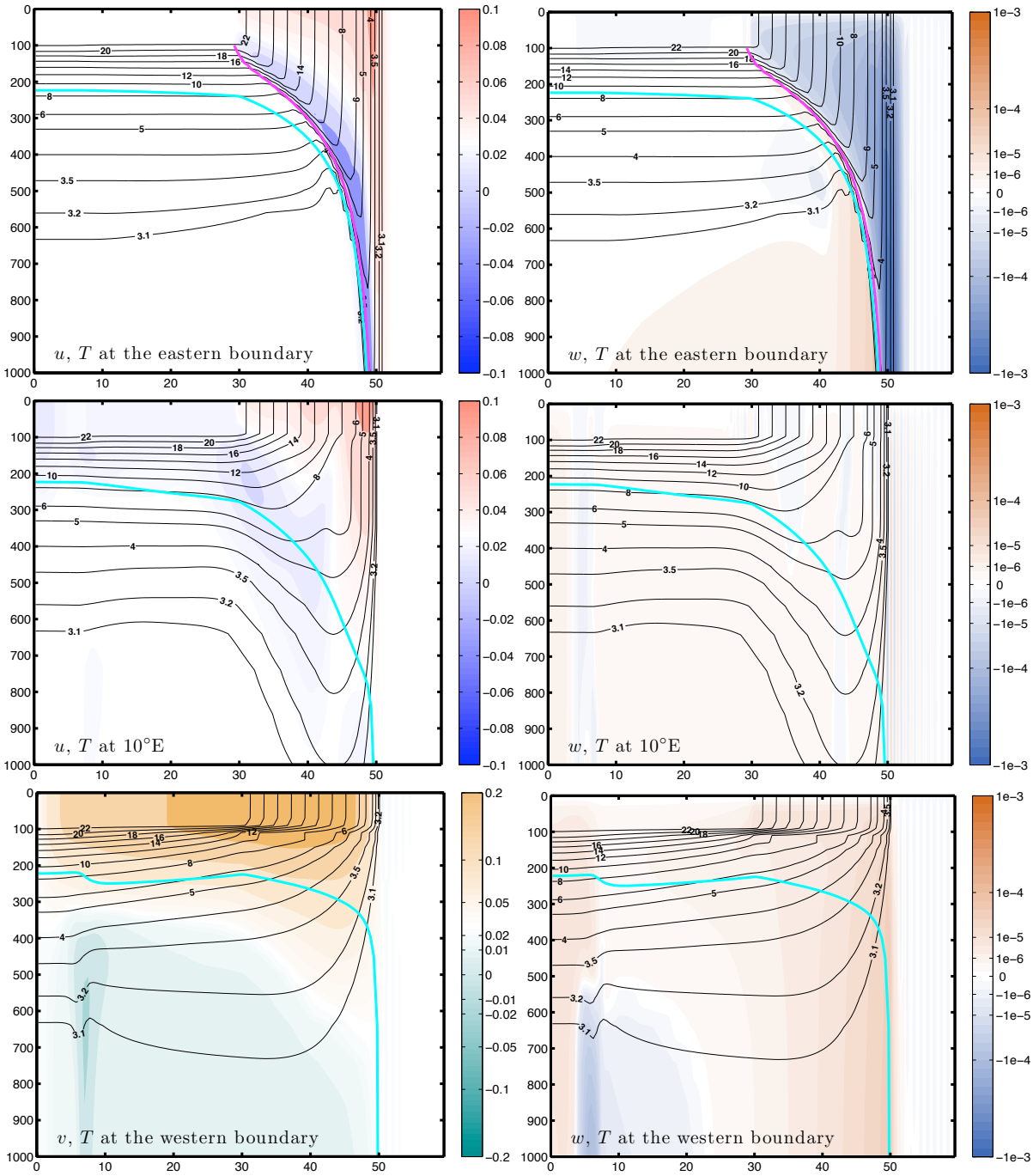

Figure 12: Meridional sections showing upper-ocean fields of temperature (contours, units are °C) along the eastern boundary (top), 10°E (interior, near the western boundary), and the western boundary (bottom) in the MITgcm run without winds and $H_s = 223$ m after 1000 years of integration. The shading in the left column corresponds to zonal velocities [ms^{-1}] in the top two panels, meridional velocity [ms^{-1}] in the bottom panel, and to vertical velocities [ms^{-1}] in the right column. The cyan lines indicates h_1 as given by Equation (31), the magenta curves shows the theoretical mixed-layer thickness as given by Equation (40).

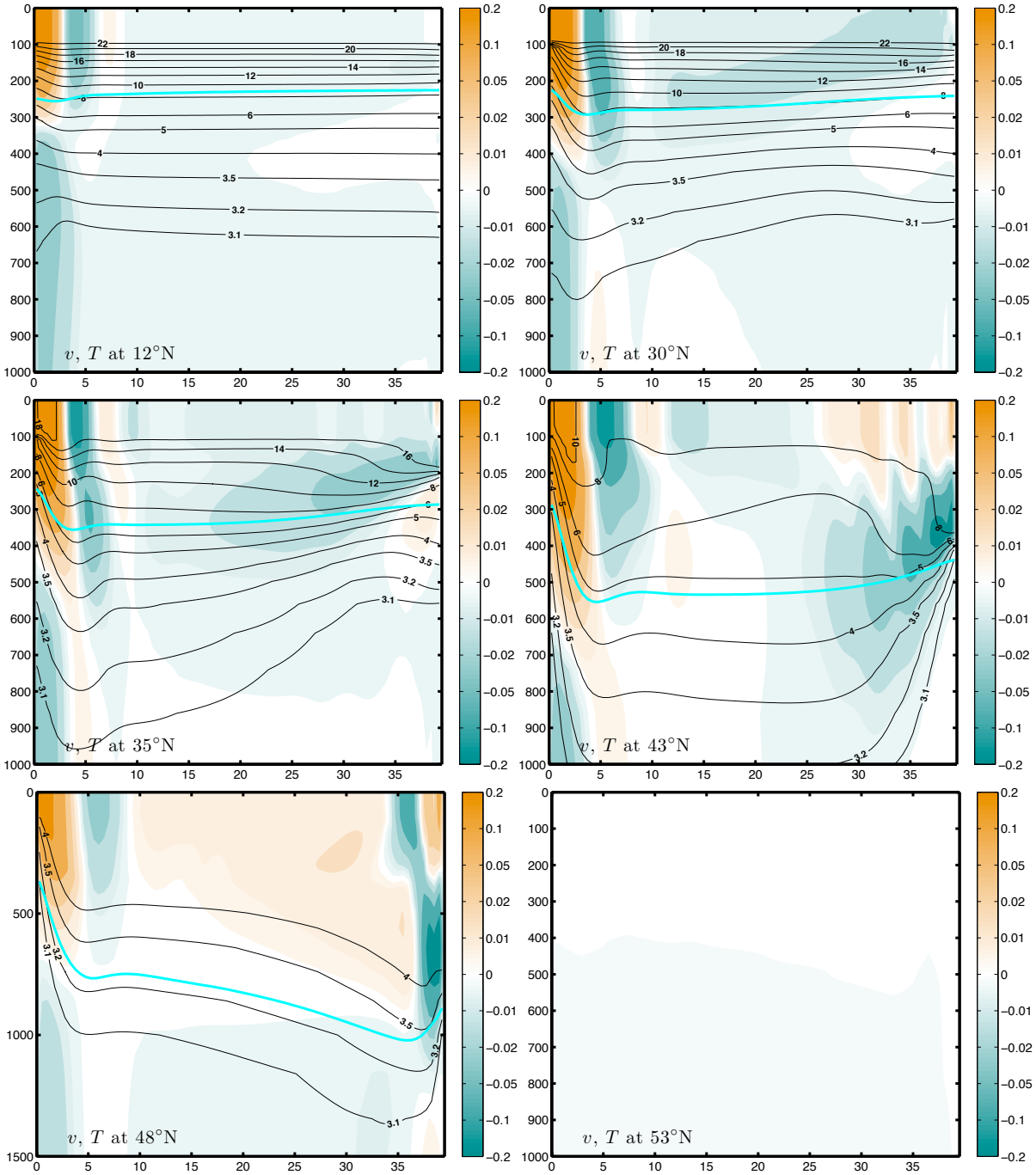

Figure 13: Zonal sections of upper-ocean v [ms^{-1}] and T [°C] in the MITgcm solution without winds and $H_s = 223$ m after 1000 years of integration, at $y = 12°$N (top-left), $y = 30°$N (top-right), $y = 35°$N (middle-left), $y = 43°$N (middle-right), $y = 48°$N (bottom-left), and $y = 53°$N (bottom-right). h_1 is indicated by the cyan line.

from the boundary (compare Schloesser et al., 2011). At 48°N, all isotherms deepen only right at the eastern boundary and then slope upwards to the west of 35°E, as that part of the section is located in the northern boundary layer. Consistently, the near-surface, meridional flow is northward in the interior ocean, in the opposite direction of the Stommel-Arons circulation further to the south. At 53°N, there is no stratification and no flow.

The middle panels of Figure 12 plot meridional sections of temperature and zonal and vertical velocities in the interior ocean at 10°E. In addition to the features discussed above, the middle-left panel reveals that the circulation in MITgcm is more complex than in a 2-layer model (*e.g.*, Kawase, 1987), because the upper-layer flow also has a shear component of the thermal wind in the region 30°N$\lesssim y \lesssim$ 50°N with a surface temperature gradient. The zonal flow is eastward near the surface and westward near the bottom of the of the upper layer, that is similar as at the eastern boundary, but weaker because the meridional temperature gradient is reduced below $z = -h_{\min}$. The middle-right panel shows that vertical motion is much weaker than at the eastern boundary. In general, w is positive and of the order of $10^{-6}\,\mathrm{m}^2/\mathrm{s}$, so that it can balance the diffusive, downward heat flux. There are pairs of very narrow vertical "lines"of enhanced upwelling and downwelling at 50°N and farther north, which are consistent with the zonal Ekman layer solution discussed in Section 4.1.3. Furthermore, there are two wider patches of sinking located at 35°N and 43°N, and a similar periodic pattern is apparent in the temperature field, which is likely associated with the northern boundary layer.

4.2.2.3 Western boundary layer: The bottom panels of Figure 13 plot the western-boundary temperature, as well as the vertical and meridional velocity fields, one grid point away from the western boundary, and Figure 13 illustrates the zonal structure of the western boundary layer. As can be seen in the meridional section, all isotherms rise monotonically towards the north, except for the deep 3.1°C and 3.2°C isotherms. Meridional velocities are northward near the surface, and southward below, and the northward flow deepens towards the pole, in contrast to the isotherms. Except for the region south of 20°N below 500 m where water sinks, upwelling extends over the entire water column and intensifies towards the north. The northward deepening of the western boundary current

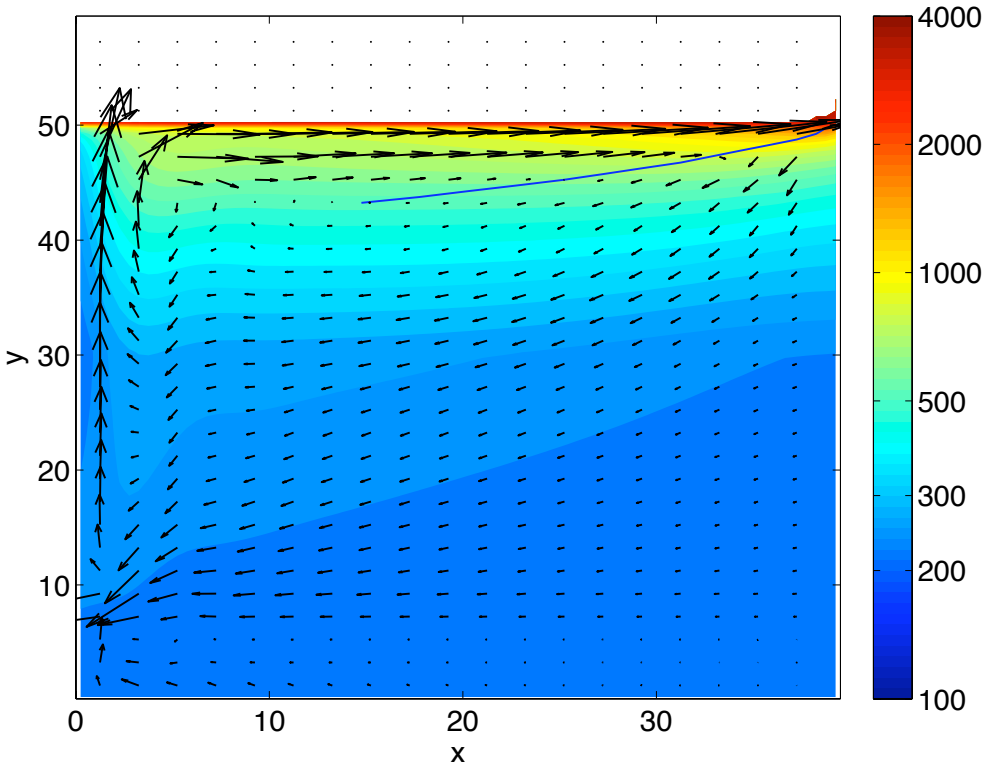

Figure 14: Plots of the upper-layer thickness h_1 and transport/width vectors $\boldsymbol{V}_1$, as derived in Section 2.3.2, for the MITgcm solution without winds and with $H_s = 223$ m. Vectors $\boldsymbol{V}_1$ are obtained assuming geostrophy in Equations (44a) and (44b). The blue line emerging from the northeastern corner of the circulation indicates the location of the maximum of h_1 along each latitude (*i.e.*, where $h_{1x} = 0$), which provides a measure of the southern edge of the northern-boundary layer.

can also be seen in the zonal sections, which exhibit a Munk-layer-like zonal structure with its characteristic recirculation, *i.e.*, a southward flow adjacent to the northward, western boundary current.

4.2.2.4 Meridional overturning circulation: Figure 15 plots two different meridional overturning streamfunctions, $\psi(y, z)$ and $\psi^T(y, T)$. Streamfunction $\psi(y, z)$ is obtained by a zonal integration of the continuity equation, whereas $\psi^T(y, T) \equiv \int_{x_w}^{x_e} V_T \, dx$ where the horizontal transport above an isotherm at depth h_T, V_T, is defined in Section 2.3.2. It follows, that the terms "upwelling" and "downwelling" have a different meaning with respect to these two streamfunctions. For $\psi(y, z)$, it actually means vertical motion, whereas for $\psi^T(y, T)$ it describes the flow across isotherms, either vertically or horizontally. As discussed above,

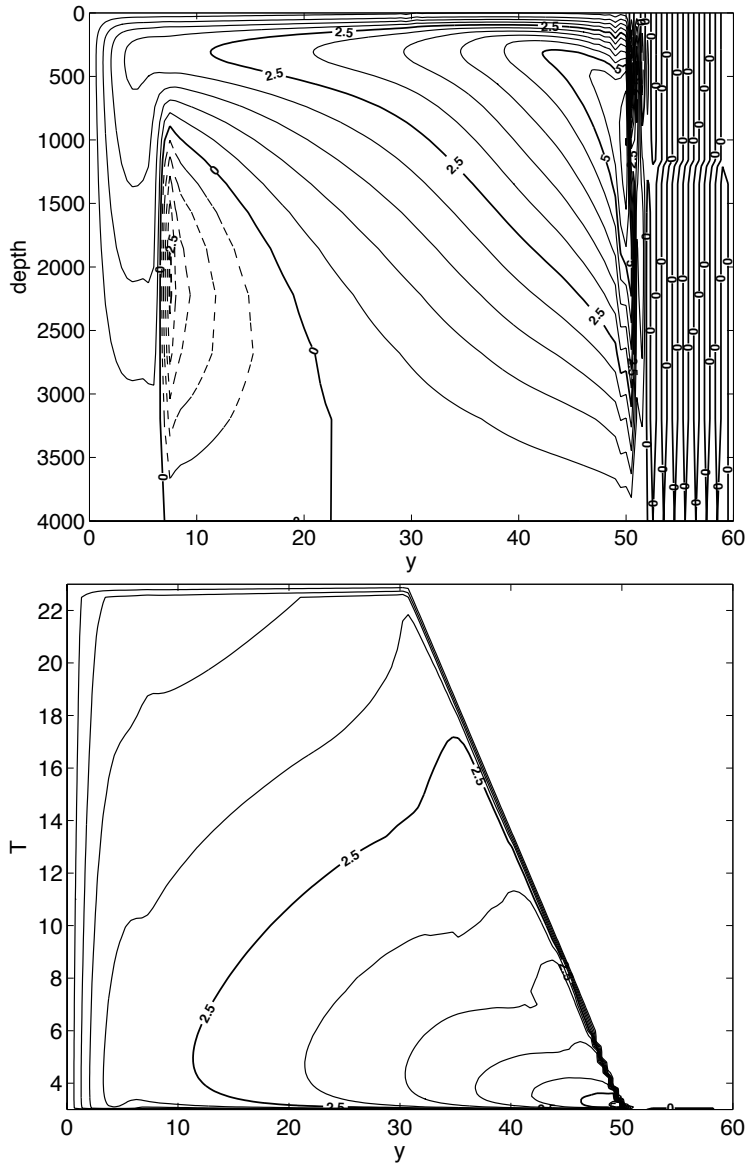

Figure 15: Plots of the streamfunctions $\psi(y, z)$ (upper panel) and $\psi^T(y, T)$ (lower panel) for the MITgcm solution with $H_s = 223$m and $\tau_o = 0$. The contour interval is 0.5 Sv in both figures.

sinking occurs primarily at the eastern boundary near y_2. Some weaker sinking also occurs in the interior, in the northern boundary layer, where upper-layer water converging towards y_2 is cooled to T_n, and hence deep-water is formed (Note that the dynamics of that boundary layer are discussed in the next section). As a result, the main overturning cell has a similar structure for ψ and ψ^T. Both reach a maximum at 49.5°N with upwelling occurring to the south of that latitude and downwelling north of it. Furthermore, the maximum overturning at each latitude is quite similar south of 45°N. Near y_2, however, ψ reaches a maximum of 7.5 Sv compared to only 6.1 Sv for ψ^T. Because of the different meanings for "upwelling" and "downwelling" for the two streamfunctions, that discrepancy can be explained by water recirculating without changing its temperature. That can occur, for example, in a closed thermal-wind-shear cell, or in an Ekman layer.

Streamfunction ψ also shows an oppositely directed, secondary, deep overturning cell adjacent to the sponge layer. This secondary cell can be explained be a difference in deep-ocean temperature at the eastern and western boundaries. Because of the Kelvin wave adjustment, the eastern-boundary, deep-ocean temperature just north of y_s' is the same as in the sponge layer, $\tilde{T} \approx T_n$. As water that downwells in the north is slightly warmer than T_n and is further warmed by diffusion as it moves southward in the western boundary current, however, western-boundary, deep-ocean water is then slightly warmer than T_n. The existence of the secondary cell follows then from the thermal-wind relation ($fv_z = g\alpha T_x$), as the vertical, meridional-velocity gradient v_z is proportional to the zonal temperature gradient T_x. The cell disappears in ψ^T because there is almost no diapycnal flux associated with it.

4.3 Northern boundary layer

The zonal boundary layer along $y_2 = 50°$N is a key feature of the MITgcm and VLOM solutions forced by buoyancy forcing with an MOC (see Sections 4.2 and 3.3). Here, we discuss the dynamics of that boundary layer in MITgcm, and what processes control the strength of upper-layer convergence there, through comparison to the corresponding boundary layer in VLOM.

4.3.1 Overview: In Chapter 3, it is argued that in the VLOM solution a northern-

boundary layer (Region 2) allows warm water to converge into the northeastern corner of the basin to close the MOC. Region 2 is associated with detrainment of upper-layer water by w_d defined in (23d) that relaxes h_1 to $h_{\max}$ and effectively damps eastern-boundary Rossby waves (see Figure 7). In Section 4.2, it is shown that a region with similar characteristics exists in the numerical MITgcm solution (Figure 13, lower left panel; Figure 14): Northwest of the line y'', isotherms rise and h_1 thins toward the west, and the upper-layer flow is (north)eastward and converges towards the eastern boundary and y_2. Despite these similarities, the detailed structures of the two northern boundary layers differ significantly: Whereas there is only one boundary-layer process (w_d) in VLOM, there are several in MITgcm and the boundary layer separates into an outer and an inner region, as illustrated in Figure 16.

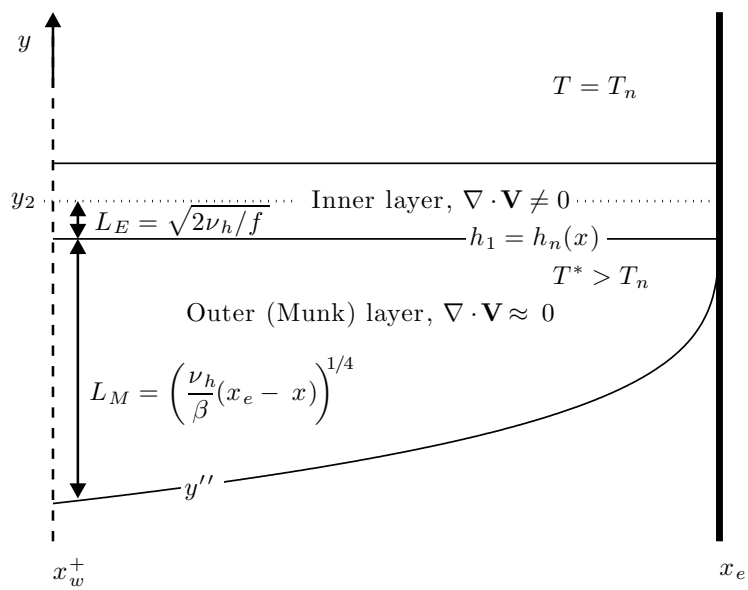

Figure 16: Schematic of the northern boundary layer and its inner and outer regions in the MITgcm.

4.3.2 Outer layer: The outer layer behaves like a zonal Munk layer (Section 4.1.3) in many respects. It has a cusp at the eastern boundary (compare Figure 14), oscillates and decays away from y_2, and, as demonstrated in sensitivity experiments using different values of ν_h, its width varies roughly like $\nu_h^{1/4}$.[6] Similar to VLOM, Rossby waves are damped

[6]The sensitivity to ν_h was tested in MITgcm by repeating the experiment described in Section 4.2 and increasing ν_h by a factor of 10. As a result, the width of the boundary layer, measured as the distance from

within the outer layer, and as a result water is channeled into the detrainment regions primarily in the northeastern corner but also along y_2. In contrast to VLOM, however, where entrainment occurs throughout the whole boundary layer, the Rossby-wave damping itself is not associated with (large) detrainment in the MITgcm. (In this regard, note that Eq. (76) is derived by setting the flow divergence to zero in the continuity equation.) Consequently, an inner boundary layer very close to y_2 is necessary to allow water to detrain; moreover, the inner layer determines the boundary condition $h_n(x)$ for the Munk layer. Thus, almost all detrainment occurs very near y_2, with only a small amount occurring slightly farther south in the numerical solution due to diffusion at the bottom of the upper layer (see below).

4.3.3 Inner layer: The inner layer restratifies the water column (thins h_1) very near y_2, provides a means for downwelling upper-layer water into the deep ocean, and sets the northern layer thickness $h_n(x)$ needed for the outer Munk layer. It is visible in the solution by the very narrow, alternating bands of upwelling and downwelling in the middle panels of Figure 12, properties which identify it as being primarily a zonal Ekman layer (Section 4.1.3). The meridional flow associated with the Ekman layer is northward near the surface and southward at depth just south of y_2. The northward advection of warm water near the surface is balanced by the a surface heat flux. Meridional advection associated with the deeper, southward flow effectively cools the deep ocean, however, and prevents the MITgcm from adjusting to the no-MOC state. Discussed next are other processes that impact the density field in the inner layer, including horizontal diffusion and numerical error.

To understand the impact of horizontal diffusion, consider an idealized version of the MITgcm first. It is initialized to a no-MOC state with geostrophic flow and vertically homogenous temperature in a region $y \leq y \leq y_2$, with $\nu_h = 0$, $\kappa_v = 0$ but finite horizontal diffusion κ_h. In addition, Q is so strong that temperatures remain unchanged at depths shallower than $h_{\min}$, and north of y_2 deep convection occurs instantaneously to ensures that $T = T_n$ at all depths. At depths greater than $h_{\min}$, away from the eastern and western boundaries, and before the arrival of a Rossby wave, temperature will then change according

the latitude where h_1 reaches its zonal maximum at $x = 20°$E to 50°N (see Figure 14), increases by a factor of 1.6, as compared to a theoretical increase of 1.8. Additional sensitivity experiments with similar results are reported in Schloesser et al. (2011).

to the one-dimensional, diffusion equation

$$T_t = \kappa_h T_{yy}. \tag{80}$$

As Q and convection then fix the boundary condition at y_2 to be $T(y_2) = T_n$, horizontal diffusion does not affect the temperature right at y_2, since the initial condition is $T = T^*$ at $y < y_2$ with $T^*_{yy} = 0$. Diffusion does affect temperatures near y', however, where temperature jumps initially from $T = T_n$ at $y < y', z = -D$ to $T = T^*$ at $y \geq y'$. As a result, T increases at $y < y'$, and decreases at $y \geq y'$. Since the latitudes y' and y_2 are rather close in all solutions, *e.g.*, $y_2 - y' \approx 0.04°$ in the solution in Section 4.2.2, diffusion quickly mixes away this narrow region of warmer temperatures, thereby thinning h_1 and restratifying the water column. That process is fastest at $z = -D$, and occurs more slowly at shallower depths, where the region occupied by warm, upper-layer water becomes wider.

Although MITgcm differs considerably from the ideal system above, diffusion must act similarly to restratify the narrow region at $y' \leq y \leq y_2$. Furthermore, as Q has a finite strength (recall that $\delta t = 3$ days in Eq. 3), the convergence of heat flux at y_2 (slightly) increases temperatures there, similar to the northward advection of warm surface water.

Regarding numerical error, since the model's horizontal resolution is 0.5°, and h_e deepens very rapidly near y' (from 1400 m at $y = 49.5°$ to 4000 m at $y = 49.96°$ for $H_s = 223$ m), the region where h_e is deep is not resolved by the grid. As a result, downwelling at the eastern boundary cannot homogenize the water column north of and the numerical model cannot adjust to a no-MOC solution, even without mixing. Since the numerical model includes physical diffusion, we presume that it dominates this numerical error.

4.3.4 Conclusions: The northern boundary layer in MITgcm consists of an outer and an inner boundary layer. The outer layer behaves like a zonal Munk layer, with a width that varies roughly proportional to $\nu_h^{1/4}$. This Munk layer channels water from the western boundary into the inner-boundary layer where it detrains near y_2. The flow field in the inner boundary resembles that of a zonal Ekman layer, and the temperature field derives from a rather complex balance of (meridional) temperature advection and diffusion, surface heat flux and convection, that may also impacted by numerical effects.

In contrast to VLOM, viscosity is dynamically important near y_2 in MITgcm, so that the flow extends into the region $y \gtrsim y_2$, where its temperature can be cooled to T_n. Furthermore, water detrains almost entirely in the inner boundary layer, very close to y_2, so that it is cooled by Q to temperatures close to T_n before it downwells. Since the diffusive heat flux in the deep ocean is rather small, it follows that the deep-ocean temperature is only slightly warmer than T_n in MITgcm. Note that this is implicit in the VLOM mixing parameterization w_d, where water detraining from layer 1 into layer 2 instantly changes its temperature from T^* to T_n.

As shown in the middle panels of Figure 12, the upper-layer thickness in MITgcm does not adjust to a constant depth $h_{\max}$ at x_w^+ as in VLOM, and h_{1y} is rather large. Thus, it appears to be impossible to determine a value for $h_{\max}$ in MITgcm from the h_1-field itself. Furthermore, the dynamics of the boundary layer are too complex as that the strength of the convergence of upper-layer water into the detrainment region could be determined form dynamical considerations alone. Note however, that an effective $h_{\max}$ can be determined by measuring the strength of overturning, applying the VLOM equation (61), and then back-solving for $h_{\max}$ (see Section 4.4).

4.4 Overturning strength

4.4.1 Definitions of $\mathcal{M}_n$: Different measures of the MOC transport are used in the literature. The most common measure of MOC strength is the absolute maximum value of the meridional streamfunction in depth space, $\psi(x, y)$, obtained by integrating the continuity equation across the basin. Alternately, the density streamfunction $\psi^\rho(y, \rho)$ is sometimes used. Since density and temperature are interchangeable in the present study, ψ^ρ is equivalent to the temperature streamfunction $\psi^T(y, T) \equiv \int_{x_w}^{x_e} V_T \, dx$, where V_T is defined in Section 2.3.2. In this manuscript, $\mathcal{M}_n$ is defined as the maximum of ψ^T, because that is more closely related to $\mathcal{M}_n$ in VLOM, where it is defined as the total amount of detrainment in the northern boundary layer (64), a diapycnal transport.

4.4.2 Relation of $\mathcal{M}_n$ to H_s, $h_{\max}$ and previous MOC scalings:

Figure 9 plots the overturning strengths in a series of MITgcm experiments, and compares

them to $\mathcal{M}_n$ curves from VLOM. The MITgcm runs differ from the one described in Section 4.2.2 only in the prescribed H_s (or $\tilde{T}$) in the sponge layer. Relation (1) suggests that $\mathcal{M}_n$ in MITgcm should be proportional to H_s^2, which essentially corresponds to VLOM results with a constant $h_{\max}$ (compare Eq. 61). Although there is no perfect fit with any of the black curves in Figure 9, the scaling with a constant C in (1) appears to describe an important part of the relation between $\mathcal{M}_n$ and H_s: Substitution of $\mathcal{M}_n$ into (1) and back-solving for C reveals that C only decreases from 0.96 to 0.63 as H_s increases from 223 m to 499 m (That means H_s^2 changes by a factor 3.7, whereas C changes only by 0.7.).

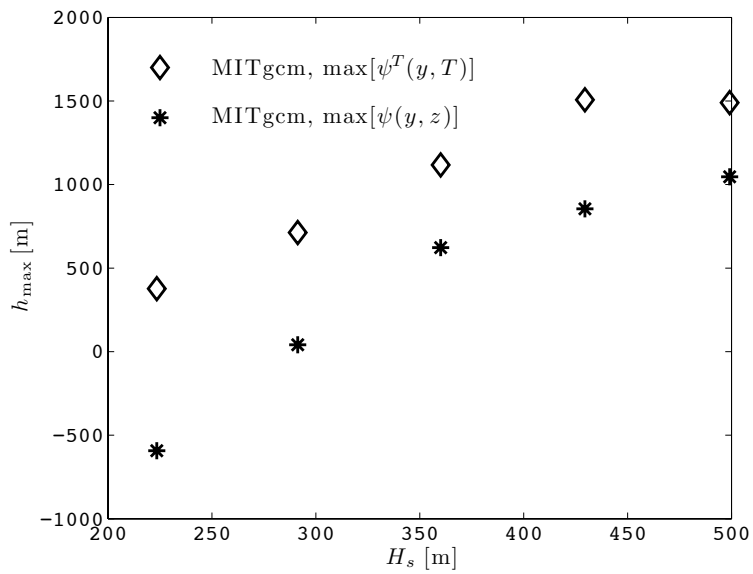

Figure 17: Mixing depth $h_{\max}$ in the MITgcm for the experiments with $\tau_o = 0$, determined by back-solving Equation (61) for $h_{\max}$ and assuming that $\mathcal{M}_n$ is given by the absolute maximum of ψ^T (diamonds) and ψ (stars) respectively.

On the other hand, the decrease in C is not negligible. A possible explanation is that the strength of Rossby-wave damping in the northern boundary layer (measured by $h_{\max}$ in VLOM) is not constant in MITgcm. The other parameters in (1) and (61) cannot account for the large differences between the MITgcm data points and VLOM curves with constant $h_{\max}$. Although $\bar{f}$ depends on H_s in VLOM, it changes rather slowly (compare the two solid black lines in Figure 9). Furthermore, the meridional density difference is constant (since the strong Q eliminates the effect of surface advection) and the deep-ocean temperature does not change much among the MITgcm experiments. Regarding the latter, the temperature

at which the maximum of ψ^T occurs increases only from 3.2°C to 3.25°C to 4.2°C as H_s increases from 223 m to 430 m to $H_s = 499$ m, respectively.

That the strength of Rossby-wave damping (measured by C) is not constant among the MITgcm experiments is furthermore supported by the fact that the MITgcm results follow the red curve in Figure 9, which shows VLOM results for non-constant $h_{\max}$, more closely than any of the other curves. To compare the VLOM results with non-constant $h_{\max}$ and MITgcm more closely, we write $C = C_{\max} = (1 - h_{\max}/D)$ in (1) without loss of generality, so that (1) and (61) are equivalent. The parameter $h_{\max}$ in MITgcm is then obtained by substituting the values for $\mathcal{M}_n$ in the MITgcm into (61) and back-solving for $h_{\max}$. The results are plotted in Figure 17 (diamonds), together with the values if the maximum of ψ is used rather than that of ψ^T (stars). The values of $h_{\max}$ increase, and hence the strength of Rossby-wave damping decreases with H_s for both estimates. Interestingly, the $h_{\max}$ values for ψ^T (except for the experiment with $H_s = 499$ m, see below) suggest almost a linear relation between $h_{\max}$ and H_s, essentially as in (65) where the width of the boundary is assumed to be constant in VLOM. Consistently, the width of the outer layer in MITgcm, as defined in Figure 14, does not change significantly with H_s in the numerical experiments. That is expected from the considerations in Section 4.3, as the width of the outer region of the boundary layer $L_M \sim (\nu_h/\beta(x_e - x))^{1/4}$ is related to the horizontal viscosity ν_h, which remains constant among the different MITgcm experiments. Hence, the correspondence between VLOM results with constant northern boundary layer thickness and the MITgcm results is consistent with the dynamics of the boundary layer in MITgcm.

A possible explanation for, why $h_{\max}$ does not further increase in the experiment with $H_s = 499$ m, is that the MITgcm solutions become unstable for sufficiently large H_s. That is the case for the solution $H_s = 499$ m that exhibits variability near $y_2 = 50$°N even in its equilibrium state, as illustrated in Figure 18, which plots h_1 and surface velocities for this solution after 1000 years. It shows periodic, westward propagating and intensifying features, that are centered just south of y_2 and are characterized by a minimum in h_1 and a cyclonic surface flow around them, which extends well into the region north of y_2. As these features reduce the time-averaged h_1 at the eastern margin of the western boundary layer (corresponding to smaller $h_{\max}$), it is plausible that they also increase the time-averaged

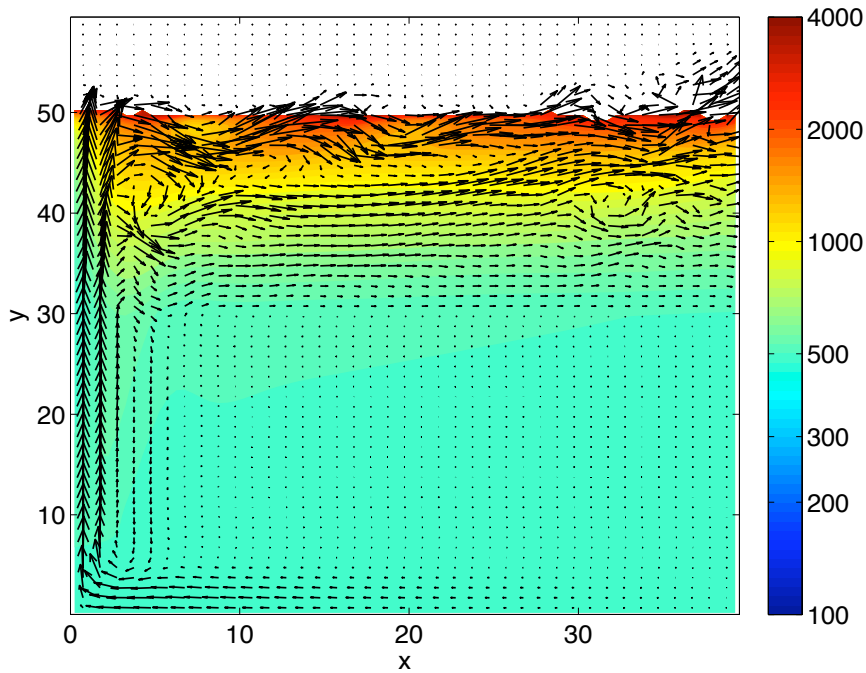

Figure 18: Horizontal map of h_1 (shading) and surface velocities (vectors) for the MITgcm experiment without winds and $\Delta H_s = 300\,\mathrm{m}$ ($H_s = 499\,\mathrm{m}$) after 1000 years.

convergence of upper-layer water into the northern boundary layer, and hence the MOC. This argument is also consistent with the findings of Cessi and Wolfe (2009), where eddies tend to lift up the thermocline and generate a "detrainment" in an eddy-resolving model near the eastern boundary. To explore that argument any further, however, is beyond the scope of this manuscript.

It is noteworthy that the value of $h_{\max}$ is negative (corresponding to a $C > 1$) for $H_s = 223\,\mathrm{m}$, when $\mathcal{M}_n$ is set to the maximum of $\psi(y, z)$. As the eastern-boundary, baroclinic pressure is equal to the tropical one because of Kelvin wave propagation, and the northern baroclinic pressure vanishes as stratification vanishes there, a value $C > 1$ (recall that C is the proportionality factor between zonal and meridional pressure difference) means that the western-boundary, baroclinic pressure has to be negative, an unphysical result. It follows that the MOC is larger than the maximal meridional, geostrophic transport (corresponding to $C = 1$), and the ageostrophic flow component is quite important near y_2. This hypothesis is consistent with the dynamical explanation of the northern boundary layer (Section 4.3), where zonal Ekman layers play an important role.

CHAPTER 5

VLOM solutions driven by differential heating and winds

In this chapter, we report VLOM solutions forced by both, buoyancy forcing Q and zonal winds τ^x. After reviewing the governing equations in Section 5.1, solutions without and then with mixing by w_d are presented in Sections 5.2 and 5.3, respectively. The depth-dependent circulation within the upper layer is discussed in Section 5.4, and finally the strength of overturning in Section 5.5. As in Chapter 3, Cartesian coordinates are used to simplify the derivation of the solutions, but solutions are calculated on a sphere to allow for a closer comparison to MITgcm solutions in Chapter 6.

5.1 Equations

As discussed in Chapter 2.2, the barotropic circulation is assumed to be in quasi steady state. With wind forcing as given in (8), the barotropic flow forms a subpolar and a subtropical gyre according to (14). An example is shown in Figure 19 with $\tau_o = 0.12\,\mathrm{N/m^2}$.

The response of the layers is governed by the equations

$$-fV_i = -\langle p_{ix}\rangle + \delta_{1i}\tau^x + \left[\nu_h \boldsymbol{\nabla}^2 U_i\right] \tag{81a}$$

$$+fU_i = -\langle p_{iy}\rangle + \left[\nu_h \boldsymbol{\nabla}^2 V_i\right] \tag{81b}$$

$$h_{it} + U_{ix} + V_{iy} = (-1)^{i+1} w_1 \tag{81c}$$

$$T_1 = T^* \qquad \text{and} \qquad T_2 = T_n, \tag{81d}$$

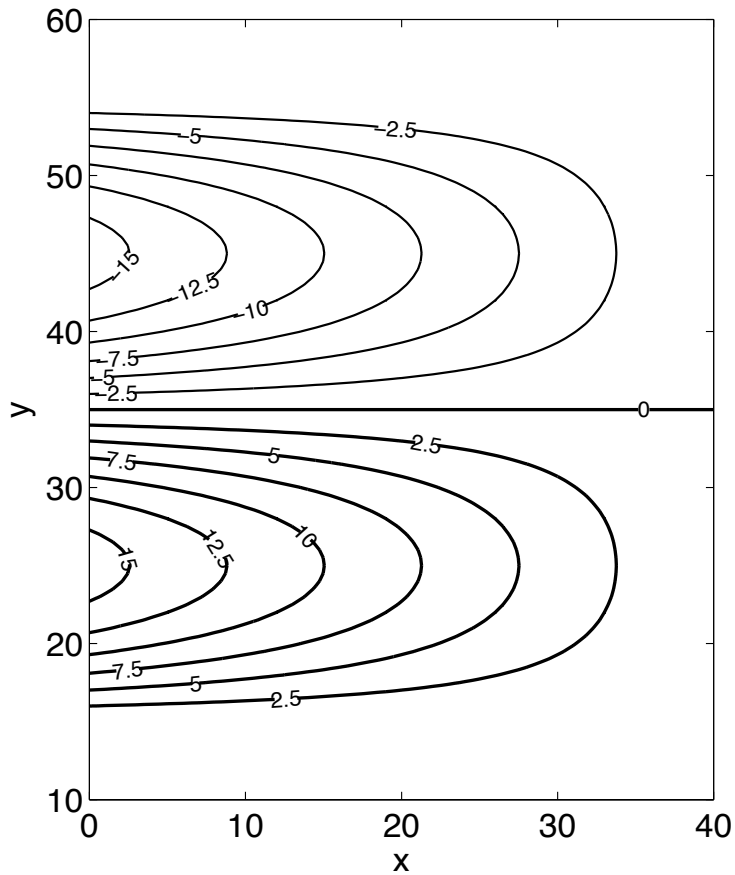

Figure 19: Plot of the barotropic streamfunction, $\Psi(x, y)$ in VLOM with $\tau_o = 0.12\,\mathrm{N/m^2}$. The unit is Sverdrups.

which are derived in Chapter 2.2.3.

In contrast to the case without winds, the pressure terms take a different form in the interior ocean and in the western-boundary layer now. The eastern-boundary and interior-ocean pressure terms are given by

$$\langle \boldsymbol{\nabla} p_1 \rangle = \frac{D - h_1}{D} \boldsymbol{\nabla} \left[\frac{1}{2} g' h_1^2 \right] + \frac{h_1}{D} \boldsymbol{\nabla} \left[\frac{f^2}{\beta} w_{ek} \left(x_e - x \right) \right] \tag{82a}$$

$$\langle \boldsymbol{\nabla} p_2 \rangle = -\frac{D - h_1}{D} \boldsymbol{\nabla} \left[\frac{1}{2} g' h_1^2 + \frac{f^2}{\beta} w_{ek} \left(x_e - x \right) \right]. \tag{82b}$$

where the barotropic solution (14) is used explicitly in equations (21), and the Ekman-pumping velocity (25). Since the depth-integrated flow is given by (14), the solutions for the two layers are not independent, and once the flow is known in one of the layers, the other

one follows from $\boldsymbol{V}_1 + \boldsymbol{V}_2 = \boldsymbol{V}$. Likewise, the layer depths are related by $h_1 + h_2 = D$ at lowest order. Note, however, that $\boldsymbol{\nabla} h$ can still be obtained from the results using (15). In the western boundary layer, solutions are derived only for the zonally-integrated, meridional transports $\mathcal{V}_{iw}$ and the western-boundary-layer entrainment W_m, and hence only the zonal pressure term,

$$\langle p_{1x} \rangle = \frac{D - h_1}{D} \left(\frac{1}{2} g' h_1^2 \right)_x + \frac{h_1}{D} f V, \tag{83}$$

is used, which is the same as in (22a).

5.2 Solution without mixing by w_d

5.2.1 Spin up: When the model is started, barotropic waves quickly adjust the depth-averaged flow, so that it forms subtropical and subpolar gyres according to (14) that are closed by western-boundary currents. Figure 19 shows the gyre circulation for $\tau_o = 0.12\mathrm{N/m}^2$. Substituting the initial layer depth H_s into (82), and then inserting the pressure gradients into (81a) and (81b), gives the interior layer transports at that stage,

$$U_1 = -\frac{D - H_s}{D} \frac{g'_y}{2f} H_s^2 - \frac{H_s}{D} \frac{\tau^x_{yy}}{\beta} (x_e - x), \qquad V_1 = -\frac{\tau^x}{f} + \frac{H_s}{D} \frac{f}{\beta} w_{ek}, \tag{84a}$$

$$U_2 = \frac{D - H_s}{D} \frac{g'_y}{2f} H_s^2 - \frac{D - H_s}{D} \frac{\tau^x_{yy}}{\beta} (x_e - x), \qquad V_2 = \frac{D - H_s}{D} \frac{f}{\beta} w_{ek}. \tag{84b}$$

Note that equations (84) include components due to the depth-averaged, geostrophic part of the gyre flow, the thermal-wind shear, and the Ekman transport.

Close to the eastern boundary, the wind-driven component of U_1 vanishes in (84), but the thermal-wind part (proportional to g'_y) does not. As a result, the thermally-driven flow converges at the eastern boundary, depresses the layer interface and triggers a Kelvin-wave response, as in the solution without wind.

In the interior subtropical ocean [that is at $y < y_r$ as defined in (28)], Ekman pumping starts to depress the layer interface h_1, and the Ekman suction raises h_1 in the subpolar ocean. At the same time, Rossby waves propagate away from the eastern boundary (see Rossby-wave characteristics in Fig. 20). After their passage, the Ekman convergence (divergence)

is balanced by geostrophic flow and h_1 is adjusted to its equilibrium state. These processes are described by (26), which since $g'_x = 0$ is

$$h_{1t} + \boldsymbol{c}_r \cdot \boldsymbol{\nabla}\, h_1 = -\frac{D - h_1}{D} w_{ek} + w_1, \tag{85}$$

where the baroclinic Rossby-wave speed now given by

$$\boldsymbol{c}_r = \left[-\beta \frac{D - h_1}{D} \frac{g' h_1}{f^2} + \frac{h_1^2 g'_y}{2Df} - \frac{\tau^x_{yy}}{D\beta}(x_e - x) \right] \boldsymbol{i} + \left[\frac{1}{D} \frac{f}{\beta} w_{ek} \right] \boldsymbol{j}. \tag{86}$$

In (85), the initial balance with Ekman pumping is a balance between the first and third terms, Rossby-wave propagation is a balance between the first and second terms, and the steady-state response (neglecting w_1) balances the second and third terms (a Sverdrup balance).

In regions where the gyre flow is eastward ($\tau^x_{yy} < 0$), the zonal component of $\boldsymbol{c}_r$ can become eastward as well. This occurs most notably near the western boundary where the zonal gyre transports are largest, provided h_1 is sufficiently small. In solutions with a zonal Rossby-wave speed reversal, there exists a region filled by western- instead of eastern-boundary, Rossby-wave characteristics[7] (see Fig. 20). The integration along Rossby-wave characteristics in this region is then determined by the layer thickness at the eastern margin of the western boundary layer, that is, $h_1(x_w^+) = h_w^+$. This property fundamentally changes the nature of the solution, since the western boundary layer, which otherwise passively closes the interior circulation, now actively feeds back onto the interior circulation. On the other hand, we will see that the effect on solutions presented in this manuscript is relatively small.

In some regions the thermocline is arrested even before the passing of a Rossby-wave front, namely, when h_1 is raised to $h_{\min}$, so that $w_1 = w_m$ given in (23a) becomes active. In that case the Ekman suction is (mostly) balanced by entrainment, and the right-hand-side terms add up to zero in (85).

For the reasons stated above, it is useful to separate the interior ocean south of y_2 into three dynamically distinct regions, which are defined as follows. Regions A and B_1 are both filled by eastern-boundary, Rossby-wave characteristics, but $w_m = 0$ in Region A and

[7] As illustrated for one example in Figure 20, the region with eastward Rossby-wave speed ($x < x_c$) is *not* equivalent to the region where Rossby-wave characteristics emerge from the western boundary layer ($x < \hat{x}_2$, Region B_2), *i.e.*, $x_r \neq \hat{x}_2$. The latter region is discussed in more detail in Section 5.2.2.2.

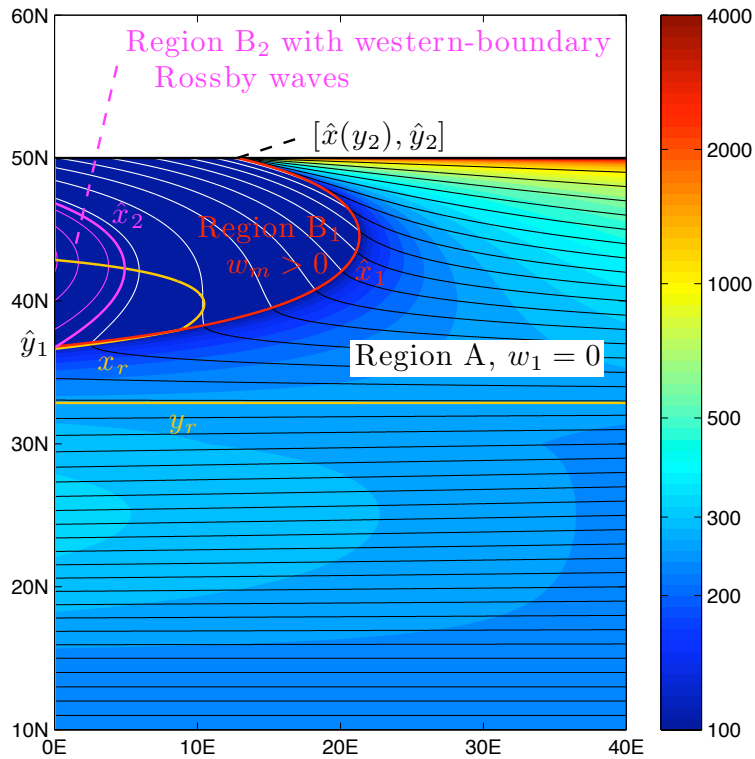

Figure 20: Map of Rossby-wave characteristics starting at the eastern boundary (black/white curves) and from the western boundary layer (magenta curves) in the VLOM solution with $H_s = 250\,\mathrm{m}$ and $\tau^x = 0.12\,\mathrm{N/m^2}$. The easternmost, magenta curve starting at $(x_w^+, \hat{y}_1)$ corresponds to $\hat{x}_2$, which separates the regions filled by eastern-boundary and western-boundary-layer characteristics (Region B$_2$). Also indicated are the upper-layer thickness h_1 (shading), the curves x_r and y_r (orange), where the zonal and meridional component of Rossby-wave speed vanishes, respectively, and the eastern boundary of Region B$_1$, $\hat{x}_1$ (red curve).

$w_m > 0$ in Region B$_1$. Region B$_2$ is filled by western-boundary, Rossby-wave characteristics (compare Figure 20).

Since the direct effect of the wind on the western-boundary layer is small, the spin-up is determined by similar processes as those described in Section 3.2.1.4. The solution for the western-boundary layer is somewhat more complex, however, because the boundary-current equation has an additional term. In addition, since h_w^+ and U_{1w}^+ are modified by Ekman pumping even before the arrival of the Rossby wave front, the western boundary layer does not adjust to a temporary steady state, but continues to adjust until the final equilibrium state is reached. For these reasons, a detailed description of the western-boundary solution

is delayed until Section 5.2.2.3.

5.2.2 Steady-state response: Now we discuss the stationary response at the eastern boundary, the interior ocean and in the western boundary layer. Throughout this section, we introduce the three nondimensional parameters γ_a, γ_b and γ_c, which characterize the MOC in the solutions. More specifically they indicate, whether entrainment occurs in the western-boundary layer (γ_a), wether an outcropping region (Region B_1) exists in the subpolar gyre (γ_b), and whether Region B_1 extends towards the northern, homogenous part of the ocean (γ_c).

5.2.2.1 Eastern boundary: Exactly as in the solution without wind forcing, Kelvin waves ensure that the steady-state pressure field along the eastern boundary adjusts $\langle p_{1y} \rangle = 0$, and it then follows from (82a) that $(g' h_1^2)_y = 0$ at $x = x_e$, the same structure as for the solution without wind forcing (47).[8] It is noteworthy that τ^y forcing does impact the eastern-boundary response, since the coastal pressure balance is then modified to $\langle p_{y1} \rangle = \tau^y$. Impacts of τ^y are not considered in this manuscript. In any case, including τ^y forcing does not impact the processes discussed below in any fundamental way.

5.2.2.2 Interior ocean:

In the interior ocean, the solution is complicated by the property that Rossby-wave characteristics do not all extend from the eastern boundary. As a result, the solution proceeds in several steps for the dynamically-distinct Regions A, B_1 and B_2. First, a solution for h_1 is derived under the assumptions that $w_1 = 0$ and that the entire basin is covered by eastern-boundary Rossby waves (Region A). For sufficiently strong wind forcing, that approach results in a region where $h_1 < h_{\min}$ (Region B_1). Within that region, mixed-layer entrainment must be active to ensure that $h_1 = h_{\min}$ there. Its eastern edge, $\hat{x}_1(y)$, is defined by the line where h_1 first thins to $h_{\min}$. Next, the extent of the region covered by western-boundary Rossby waves (Region B_2) is derived as follows: First we solve for the line where the zonal Rossby-wave speed vanishes, $x_r(y)$. To the west of x_r, the Rossby-wave speed is eastward.

[8] If a no-slip condition is applied at the eastern boundary, a viscous eastern boundary layer is required to cancel the meridional Sverdrup flow at x_e. Such a boundary layer, and its effect on the coastal density structure, is not considered here.

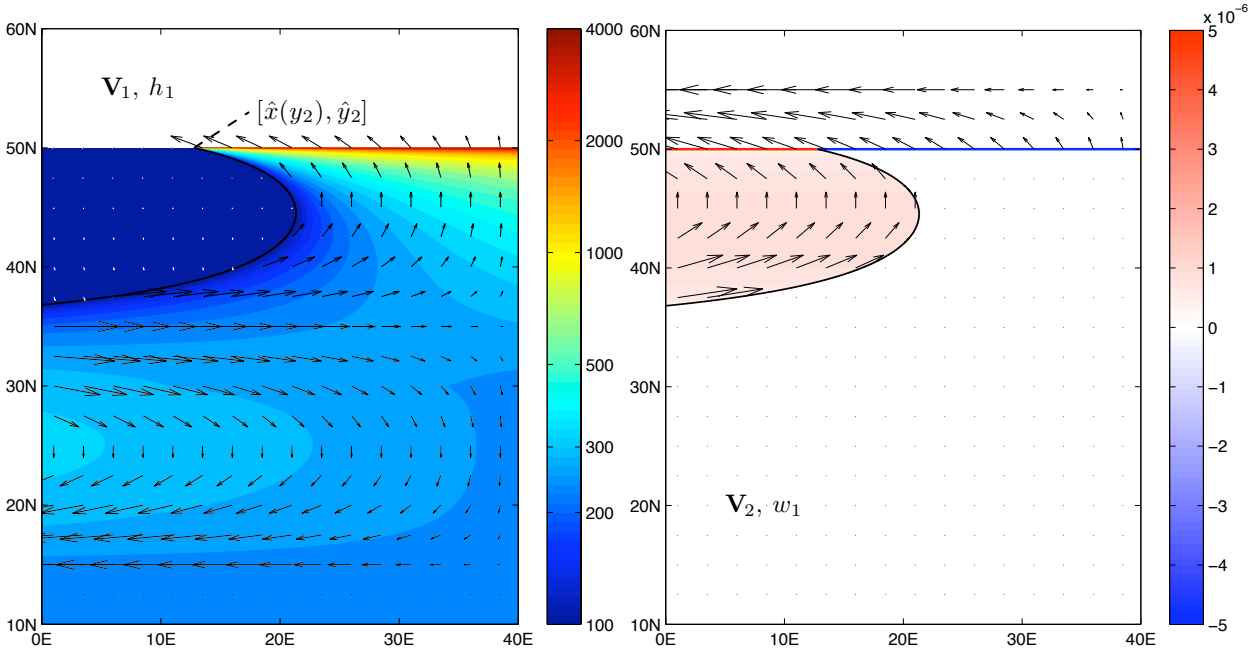

Figure 21: Horizontal map of the layer thickness h_1 (shading) and the horizontal transports/width $\boldsymbol{V}_1$ (vectors) in layer 1 (left panel), and the across-interface velocity w_1 (shading) and horizontal transports/width $\boldsymbol{V}_2$ (vectors) in layer 2 (right panel) for VLOM with $H_s = 250\,\mathrm{m}$ and $\tau^x = 0.12\,\mathrm{N/m^2}$. In the right panel at y_2, detrainment $w_1 = w_c$ is indicated as a blue line to the east of $\hat{x}_1(y_2)$, and entrainment $w_1 = w_m$ as a red line farther to the west. The corresponding western boundary layer solution is shown in Figure 22.

Then we solve for the westernmost, Rossby-wave characteristic leaving from the eastern boundary, which also constitutes the eastern boundary of Region B_2, $\hat{x}_2(y)$. The line is obtained by integrating the Rossby-wave speed (86) from the southern intersection of x_w^+ and x_r, $(x_W^+,\ y(x_r = x_w^+))$.[9] As argued below, $h = h_{\min}$ and $w_m > 0$ in Region B_2 in steady state, so that the union of Region B_1 and Region B_2 defines a Region B ($\mathrm{B}_1 \cup \mathrm{B}_2 = \mathrm{B}$). Figures 20 and 21 provide an example of a steady-state, interior-ocean solution for $H_s = 250\,\mathrm{m}$ and $\tau^x = 0.12\,\mathrm{N/m^2}$ in which Regions A, B_1 and B_2 are present.

[9]That step implies that $y(x_r = x_w^+) > y_r$ (recall the y_r is defined by (28), constitutes the line where $c_r^y = 0$ in the wind-driven gyres, and that $y_r = 32.86°\mathrm{N}$ for the τ^x used here), which holds for the solutions discussed in this manuscript. The characteristic $\hat{x}_2$ is then the westernmost characteristic starting from the eastern boundary, because the meridional Rossby wave speed is northward at $y > y_r$, and Rossby-wave characteristics do not intersect with each other. Hence all other characteristics starting at the eastern boundary must remain to the east, and western-boundary characteristics must remain to the west of $\hat{x}_2$. If x_r intersects with y_r, however, the intersection is a stagnation point with $\boldsymbol{c}_r = 0$; in that case, $\hat{x}_2$ is defined by two characteristics, which proceed just to the southeast and northeast of that stagnation point.

To obtain the solution in Region A, we first show that $\boldsymbol{V}_2 = 0$ there. Using the pressure term (82b), one can obtain the steady-state, vorticity equation for layer 2,

$$\boldsymbol{\nabla}\left(\frac{h_2}{fD}\right) \times \boldsymbol{\nabla}\left[\frac{1}{2}g'h_1^2 + \frac{f^2}{\beta}w_{ek}\left(x_e - x\right)\right] = -w_1. \tag{87}$$

It follows that $\boldsymbol{V}_2$ is parallel to lines of constant h_2/f where $w_1 = 0$ (*i.e.*, in Region A). Since isolines of h_2/f intersect the eastern boundary, and there can be no flow through that solid boundary, it follows that $\boldsymbol{V}_2 = 0$. Interestingly, since $\boldsymbol{V}_2 = 0$ in Region A, the Sverdrup transport (14) is contained entirely within layer 1.

There are two subregions within Region A: one where $h_1 < D$ and the other where $h_1 = D$ [10]. To obtain h_1 in the former subregion, one solves for $\langle \boldsymbol{\nabla} p_2 \rangle = 0$ in (82b), which results from (81a) and (81b) since $\boldsymbol{V}_2 = 0$. It follows that

$$h_1(x,y) = \begin{cases} \left[\dfrac{g'_s}{g'}H_s^2 - \dfrac{2f^2}{g'\beta}w_{ek}(x_e - x)\right]^{1/2}, & x \le x_D(y) \\ D, & x > x_D(y) \end{cases} \tag{88}$$

where $x_D(y)$ (defined next) is the dividing line between the two subregions. The solution to $\langle \boldsymbol{\nabla} p_2 \rangle = 0$ uses the constant of integration, $g'_s H_s^2$, which results from applying the boundary condition that $h_1(x_e) = h_e$ for $y < y'$ (recall that y' is the latitude where h_1 first thickens to D along the eastern boundary) and using the relation $g'h_e^2 = g'_s H_s^2$ (see Eq. 47). Curve $x_D(y)$ is the Rossby-wave characteristic that extends westward and northward from (x_e, y'), and $h_1 = D$ along that characteristic because the right-hand side of (85) vanishes.

Lines of constant $h_1 = H$ are given by the curves

$$x_H(y,H) = x_e - \frac{g'_s H_s^2 - g'H^2}{2(f^2/\beta)w_{ek}} \tag{89}$$

which is derived by back-solving (88) for x. It is useful to determine whether h_1 contours extend to the western boundary or intersect latitude y_2. Interestingly, for a particular (critical) value of H_s, H_c, *all* h_1 contours intersect the point $(x_w^+,\, y_2)$. Setting $x_H = x_w^+$ in (89) gives,

$$H_c = \left[\frac{2f_2^2}{g'_s\beta_2}w_{ek2}(x_e - x_w^+)\right]^{1/2}, \tag{90}$$

[10] Variations of h_1 due to changes in sea-level height are neglected for the lowest-order response, but the sea-level slope can be calculated using (15). Hence the upper-layer thickness is not necessarily constant in regions where layer 2 vanishes, as suggested by the lowest order result $h_1 = D$.

where the subscript "2" indicates the variable has been evaluated at $y = y_2$. Note that, because $g'(y_2) = 0$, H doesn't enter (90) at all, which is the reason why all h_1 contours converge to (x_w^+, y_2). Consequently, the dimensionless parameter,

$$\gamma_c = \frac{H_c^2}{H_s^2}, \tag{91}$$

determines whether h_1 contours intersect the western boundary ($\gamma_c \leq 1$) or latitude y_2 ($\gamma_c > 1$).

North of latitude y_r (defined by Eq. 28), Ekman suction thins h_1 away from the eastern boundary. Depending on the strength of the winds and the value of H_s, h_1 may reach its minimum thickness $h_{\min}$ at some longitude, $\hat{x}_1$, east of the western boundary. In that case, w_m ensures that h_1 does not thin west of $\hat{x}_1$ by entraining enough water to keep $h_1 = h_{\min}$ and defining Region B_1. Suppose for the moment that Region B_1 exists. Then, the eastern boundary of Region B_1 is defined by (89) with $x_H(y) = \hat{x}_1(y)$ and $h_1 = h_{\min}$,

$$\hat{x}_1(y) = x_e - \frac{g_s' H_s^2 - g' h_{\min}^2}{2(f^2/\beta) w_{ek}}. \tag{92}$$

Under what conditions does $\hat{x}_1(y) > x_w^+$ so that Region B_1 exists? For a given wind strength (τ_o), it exists when H_s is larger than a critical value, H_b. To find H_b, set $x = x_w^+$ and $H = h_{\min}$ in (89), and (for the moment) allow H_s to be a function of y. The latitude y_b where H_s is minimal is then found by solving $H_{s\,y} = 0$ for y, and it is generally located slightly south of $y_W + \frac{1}{2}\Delta y_W$. From (88) it then follows that Region B_1 exists if $H_s < H_b$, where

$$H_b = \left[\frac{g'}{g_s'} h_{\min}^2 + \frac{2f^2}{g_s'\beta} w_{ek}(x_e - x_w^+)\right]^{1/2} \quad @ \quad y = y_b. \tag{93}$$

The dimensionless parameter,

$$\gamma_b = \frac{H_b^2}{H_s^2}, \tag{94}$$

then indicates whether an outcropping of the deep layer does ($\gamma_b > 1$) or does not occur ($\gamma_b \leq 1$).

Equation (88) is not valid in the region filled by western-boundary Rossby-wave characteristics (Region B_2), because the eastern-boundary condition, $h_1(x_e) = h_e$, is implicit in

it, and it assumes $\boldsymbol{V}_2 = 0$. In order to derive a solution within Region B_2, a boundary condition at $h_1(x_w^+) = h_w^+$ is required, which then allows for integration along Rossby-wave characteristics. As these characteristics emerge from the western-boundary layer, however, it is difficult to derive that boundary condition from dynamical principles alone, *i.e.,* it is impossible without solving for the structure of the western boundary layer. For the solutions discussed in this manuscript, that problem is solved by imposing the boundary condition $h_w^+ = h_{\min}$, which is plausible for the following reasons: *i)* The northern part of the region is contained within Region B_1, within which $h_1(x_w^+) = h_{\min}^+$ already. *ii)* A corresponding region must be present in the MITgcm solutions discussed in Section 6, and there $h_w^+ \approx h_{\min}$ (compare Figure 30). *iii)* Finally, in order for c_r^x to be eastward, it follows from (86) that $h_1 < (f^2\tau_{yy}^x)/(Dg')(x_e - x_w^+)$. Hence h_1 cannot be much larger than $h_{\min}$ for the (reasonable) parameter choices discussed in this manuscript.

From Equation (85), it follows then that $h_1 = h_{\min}$ is valid also in the interior of Region B_2 in steady state: The upper-layer thickness h_1 can either thin along Rossby-wave characteristics (if the second and third terms balance) or remain constant at $h_{\min}$ (if the third and fourth terms balance and $w_1 > 0$). As w_m does not allow for h_1 to be smaller than $h_{\min}$, however, the latter has to be the case.

The eastern boundary of Region B, $\hat{x}(y)$, is defined to be either $\hat{x}_1(y)$ or $\hat{x}_2(y)$, depending on which extends further to the east at any latitude y. As $h_1 = h_{\min}$ in both Regions B_1 and B_2, the layer thickness is constant throughout the entire Region B. The upper-layer flow in Region B is then given by the inviscid versions of (81a) and (81b) with $h_1 = h_{\min}$,

$$U_1 = -\frac{D - h_{\min}}{D}\frac{g_y'}{2f}h_{\min}^2 - \frac{h_{\min}}{D}\frac{\tau_{yy}^x}{\beta}(x_e - x), \qquad x < \hat{x}, \tag{95a}$$

$$V_1 = -\frac{\tau^x}{f} + \frac{h_{\min}}{D}\frac{f}{\beta}w_{ek}, \qquad x < \hat{x}. \tag{95b}$$

In addition, the layer-2 flow is non-zero for $x < \hat{x}$, so that the total transport still adds up to the Sverdrup transport (14). Finally, substitution of (95) into the continuity equation gives the entrainment

$$w_1 = w_m = -\frac{D - h_{\min}}{D}\left(\frac{\tau^x}{f}\right)_y = \frac{D - h_{\min}}{D}w_{ek}, \tag{96}$$

which is essentially the Ekman suction.

Let the southernmost and northernmost latitudes of Region B (*i.e.*, where $\hat{x}$ intersects with x_w^+) be $\hat{y}_1$ and $\hat{y}_2$, respectively. Then, $\hat{y}_2$ lies south of y_2 if $\gamma_c < 1$, whereas it extends to y_2 so that $\hat{y}_2 = y_2$ if $\gamma_c \geq 1$.

Interestingly, h_1 is discontinuous along part of the southern boundary of Region B, when it is determined by Region B_2 rather than B_1 (*i.e.*, $\hat{x}_2 > \hat{x}_1$), and hence a northeastward boundary current exists along $\hat{x}_2(y)$. Assuming that the along-boundary flow is geostrophic, which is justifiable provided mixing is small enough for the boundary layer to be narrow, the transport of the boundary current is given by

$$\mathcal{V}_B = \frac{g'}{2f}\left[h_1^2 - h_{\min}^2 - \frac{2}{3D}\left(h_1^3 - h_{\min}^3\right)\right], \tag{97}$$

where h_1 is given by (88). Equation (97) is derived by integrating (81b) across the jump in h_1 from $\hat{x}_2 - \Delta x$ to $\hat{x}_2 + \Delta x$ and then taking the limit $\Delta x \to 0$.

It is useful to contrast the Region-B solution to similar solutions discussed in Huang and Flierl (1987). In the limit $h_{\min} \to 0$, the case $\gamma_b \leq 1$ ($\gamma_b > 1$) corresponds to their subcritical (supercritical) regimes and $\hat{x}_1(y)$ is identical to their outcropping line. It is noteworthy, that without density advection, the dynamics of the outcropping region (Region B) is only marginally affected by the consideration of a variable upper-layer temperature. Since the first two terms in the zonal Rossby-wave speed (86) vanish as $h_1 \to 0$, $\hat{x}_2$ must lie to the east of $\hat{x}_1$ in the region where $\tau_{yy}^x < 0$ in the present solution, when the limit $h_{\min} = 0$ is considered. As a result, Region B in the present solution is slightly larger than in theirs. (Huang and Flierl (1987) interpreted the point $\hat{y}_1$ to indicate the separation of the western Gulf Stream. With that interpretation, the separation point is shifted slightly farther to the south in our model.) Finally, the boundary current transport, $\mathcal{V}_B$, is different, since the present solutions allow for a transport within Region B (since $h_{\min} \neq 0$), as do solutions discussed in Nonaka et al. (2006).

In summary, the reversal of the Rossby-wave speed generates dynamically interesting features in the solution, that may be worth exploring in more detail in future studies. In the present framework, the effect on the strength of the MOC is negligible, however, as Region B_2 is (almost) entirely enclosed in Region B_1, so that the extent of the region with

$h_1 = h_{\min}$ is not affected much by the inclusion of Region B_2.

In contrast to the VLOM solution without winds, $V_1(y_2)$ in Regions A and B does not vanish if y_2 is located within the subpolar gyre ($y_2 < y_W + \Delta y_W$). (See Figure 21) East of $\hat{x}(y_2)$, $V_1(y_2)$ is given by Equation (14) and directed to the north. Consequently water is cooled to T_n when it crosses y_2, and it is transformed to layer-2 water with a rate of

$$w_c(y_2) = -\frac{\tau_y^x}{\beta}\,\delta(y_2 - y), \qquad x \geq \hat{x}. \tag{98}$$

West of $\hat{x}(y_2)$, w_c vanishes because $V_1(y_2)$ is given by (95b) there, which is dominated by southward Ekman transport. In this region, water is heated to $T^* > T_n$ at $z \geq -h_{\min}$ when it flows southward across y_2, forming layer 1; hence this near-surface flow formally constitutes an entrainment,

$$w_m(y_2) = \left[\frac{\tau^x}{f} - \frac{h_{\min}}{D}\frac{f^2}{\beta}w_{ek}\right]\delta(y_2 - y), \qquad x < \hat{x}, \tag{99}$$

which is slightly less than the southward Ekman transport, as it is partly compensated by the northward, geostrophic, gyre transport contained in the upper layer.

5.2.2.3 Western boundary: The solution is closed by a western boundary layer. In this section, we first discuss the equations and some additional assumptions made to simplify matters. Then we derive an algorithm for obtaining the solution, and finally solve for the transports of the alongshore currents and the entrainment within the boundary layer.

Equations and assumptions: For the barotropic flow, the transport of the boundary current is given by (16), $\mathcal{V}_w = \left(\tau_y^x/\beta\right)(x_e - x_w)$, and is directed southward in the subpolar gyre. For the upper-layer transport, the continuity equation is integrated from a latitude just north of y_2, $y_2^+ = \lim_{\Delta y \to 0} y_2 + \Delta y$, which yields

$$\mathcal{V}_{1w}(y) = \int_y^{y_2^+} W_m\,dy' - \int_y^{y_2^+} U_{1w}^+\,dy', \tag{100}$$

where x_w^+ is a longitude just to the east of the boundary layer, and $U_{1w}^+ \equiv U_1(x_w^+)$. The boundary condition $\mathcal{V}_{1w}(y_2^+) = 0$ is applied because the upper layer, and hence its transport, vanishes to the north of y_2. There are two difficulties with using (100) to solve for $\mathcal{V}_{1w}$. First, it is not entirely determined by the interior flow U_{1w}^+ because western-boundary-layer

entrainment $W_m = \int_{x_w}^{x_w^+} w_m \, dx$ may occur. Second, U_{1w}^+ and h_w^+ are not given by the interior solution in regions where the Rossby-wave speed is westward. In this study, the second problem has been solved by specifying $h_w^+ = h_{\min}$ in Region B_2 above. The first is dealt with below.

The fundamental problem with the solution for the western-boundary entrainment W_m is that it depends on the structure of h_1 within the boundary layer, *i.e.*, w_m occurs at any point where h_1 adjusts to a value smaller than $h_{\min}$ otherwise (compare Equation 23a). To avoid solving for the boundary-layer structure, we now derive an approximation to W_m that only depends on the western-boundary layer thickness h_w.

We start by deriving a second equation for $\mathcal{V}_{1w}$, relating $\mathcal{V}_{1w}$ to h_1. Integrating (81a) zonally across the boundary layer, with (83) and the assumption that the boundary layer is infinitesimally small, so that the contribution from the Ekman transport vanishes, we obtain

$$\mathcal{V}_{1w}(y) = \underbrace{\frac{g'}{2f}\left[h_w^{+2} - h_w^2 - \frac{2}{3D}\left(h_w^{+3} - h_w^3\right)\right]}_{\text{baroclinic part}} + \underbrace{\int_{x_w}^{x_w^+} \frac{h_1}{D} V \, dx}_{\text{barotropic part}}, \tag{101}$$

where $h_w^+ \equiv h_1(x_w^+)$. For convenience, the first part of the right-hand-side of (101) is referred to as the baroclinic part of $\mathcal{V}_{1w}$ since it is equivalent to (50) with no barotropic flow, and the second part is called the barotropic part.

The barotropic term in (101) involves an integral across the western-boundary current, and to evaluate it exactly requires that the boundary-layer structure is known, similarly as for W_m in (100). Instead of solving exactly for that structure, however, the integral is approximated as

$$\int_{x_w}^{x_w^+} \frac{h_1}{D} V \, dx = \frac{h_w}{D} \mathcal{V}_w \theta(-\mathcal{V}_w) + \mathcal{V}_w \theta(\mathcal{V}_w). \tag{102}$$

According to (102), the barotropic part of $\mathcal{V}_{1w}$ has two different formulas in the subpolar gyre where ($\mathcal{V}_w \leq 0$) and the subtropical gyre ($\mathcal{V}_w \geq 0$). In the subpolar gyre, the approximation assumes that most of the V_1-integral occurs very near the coast where $h_1 \approx h_w$; in the subtropical gyre it assumes that all the Sverdrup transport occurs in the upper layer and essentially eliminates western boundary upwelling there. That is reasonable, as the western-

boundary layer interface also deepens abruptly to the south of y_W in the MITgcm solutions (compare Figure 28, lower panels)

Furthermore, we assume that $W_m > 0$ only when $h_w = h_{\min}$. This assumption is valid, when h_1 has a Munk-layer-like zonal structure, and the baroclinic part of (101) is directed to the north. In the northern part of the subpolar gyre, however, the baroclinic part is directed to the south in some solutions so that h_1 can decrease away from the coast. As the error possibly introduced in such a situation is minor, however, the assumption is reasonable.

Algorithm: With these assumptions, (101) can be used to determine whether W_m is needed in (100): Specifically, if $h_w(y) < h_{\min}$ with $W_m = 0$, then $\int_y^{y_2^+} W_m\, dy'$ is set so that $h_w(y) = h_{\min}$. To perform this operation more efficiently, it is convenient to define the maximal western boundary current transport $\tilde{\mathcal{V}}_{1w} \equiv \mathcal{V}_{1w}(h_w = h_{\min})$ analogous to (62), that is

$$\tilde{\mathcal{V}}_{1w}(y) = \frac{g'}{2f}\left[h_w^{+2} - h_{\min}^2 - \frac{2}{3D}\left(h_w^{+3} - h_{\min}^3\right)\right] + \left[\theta(\mathcal{V}_w) + \frac{h_{\min}}{D}\theta(-\mathcal{V}_w)\right]\mathcal{V}_w. \tag{103}$$

As $\mathcal{V}_{1w}$ is inversely proportional to h_w, the statement $\mathcal{V}_{1w}(y) > \tilde{\mathcal{V}}_{1w}(y)$ is identical to $h_w(y) < h_{\min}$, and the solution can be in principle obtained as follows: First $\mathcal{V}_{1w}(y)$ is calculated from (100) with $W_m = 0$, then (100) is solved for $\int_y^{y_2^+} W_m\, dy'$ to ensure that $\mathcal{V}_{1w} \not> \tilde{\mathcal{V}}_{1w}$. There is a practical problem with that approach, however , as $\mathcal{V}_{1w} \not> \tilde{\mathcal{V}}_{1w}$ has to be tested for every point in the interval $[y, y_2]$ to make sure that all entrainment is accounted for. For solutions where W_m is sufficiently smooth, reasonable solutions can be obtained by evaluating (100) iteratively for a finite number of points Y_i, starting at $Y_1 = y_2$ and then proceeding southwards. At the ith point, the "preliminary" transport $\mathcal{V}'_{1w}$ (defined next) is then given by

$$\mathcal{V}'_{1w}(Y_i) = \mathcal{V}_{1w}(Y_{i-1}) + \int_{Y_i}^{Y_{i-1}} U_{1w}^+\, dy'. \tag{104a}$$

The actual boundary-current transport and the entrainment are then given by

$$\mathcal{V}_{1w}(Y_i) = \mathcal{V}'_{1w}(Y_i) - \int_{Y_i}^{Y_{i-1}} W_m\, dy' \tag{104b}$$

$$\int_{Y_i}^{Y_{i-1}} W_m\, dy' = \left(\mathcal{V}'_{1w}(Y_i) - \tilde{\mathcal{V}}_{1w}(Y_i)\right)\theta[\mathcal{V}'_{1w}(Y_i) - \tilde{\mathcal{V}}_{1w}(Y_i)]. \tag{104c}$$

This methodology even allows for the solution to be obtained without introducing an error, if the discrete points Y_i are chosen such that they are located at points where western-boundary

entrainment occurs[11]. In order to find these point, however, we first have to understand where, and under which conditions, western-boundary entrainment occurs. That issue is discussed next.

We start by zonally integrating the continuity equation from the western to the eastern boundary, which yields

$$\mathcal{V}_{1y} = W_m + \int_{x_w^+}^{x_e} w_m \, dx \qquad y < y_2, \tag{105}$$

with the total, meridional, layer-1 transport $\mathcal{V}_1(y) = \int_{x_w}^{x_e} V_1 dx$. It follows from (105) that $\mathcal{V}_1$ must increase monotonically ($\mathcal{V}_{1y} > 0$) for all $y < y_2$, because detrainment ($w_1 < 0$) is confined to $y = y_2$, and hence the second and third terms in (105) are always positive. Furthermore, $\mathcal{V}_{1y} = 0$ at latitudes where no entrainment occurs. Next, we define the maximal, meridional transport that can be maintained by the model $\tilde{\mathcal{V}}_1 \equiv \mathcal{V}_1 + (\tilde{\mathcal{V}}_{1w} - \mathcal{V}_{1w})$, and note that $\mathcal{V}_1 \leq \tilde{\mathcal{V}}_1$ at all y follows directly from $\mathcal{V}_{1w} \leq \tilde{\mathcal{V}}_{1w}$, and that $\mathcal{V}_1 = \tilde{\mathcal{V}}_1$ is a necessary condition for western-boundary entrainment. We proceed by deriving two other useful properties of $\tilde{\mathcal{V}}_1$.

First, consider a latitude y where $\tilde{\mathcal{V}}_{1y} \leq 0$: As the integrations in (100) are performed southward, and $\mathcal{V}_1(y + \Delta y) \leq \tilde{\mathcal{V}}_1(y + \Delta y)$, it follows in the limit $\Delta y \to 0$ that $\mathcal{V}_1(y) \leq \mathcal{V}_1(y + \Delta y) \leq \tilde{\mathcal{V}}_1(y + \Delta y) < \tilde{\mathcal{V}}_1(y)$. Consequently, $W_m = 0$ at y, because $W_m(y) > 0$ only in case $\mathcal{V}_1(y) > \tilde{\mathcal{V}}_1(y)$ with $W_m(y) = 0$. As a result, $\tilde{\mathcal{V}}_{1y} > 0$ is a necessary condition for $W_m > 0$.

Now, consider a latitude y where $\tilde{\mathcal{V}}_{1y} > 0$ and $\mathcal{V}_1(y + \Delta y) = \tilde{\mathcal{V}}_1(y + \Delta y)$ with $\Delta y \to 0$. It follows that $\mathcal{V}_1(y + \Delta y) = \tilde{\mathcal{V}}_1(y + \Delta y) > \tilde{\mathcal{V}}_1(y) \geq \mathcal{V}_1$, so that $\mathcal{V}_{1y} \geq \tilde{\mathcal{V}}_{1y} > 0$. Hence $\tilde{\mathcal{V}}_{1y} > 0$ and $\mathcal{V}_1(y + \Delta y) = \tilde{\mathcal{V}}_1(y + \Delta y)$ are sufficient conditions for western-boundary entrainment to occur at y, if $\int_{x_w^+}^{x_e} w_m \, dx = 0$. In case $\int_{x_w^+}^{x_e} w_m \, dx > 0$, on the other hand, it can be shown analogous, that western-boundary entrainment must occur if $\tilde{\mathcal{V}}_{1y} > \int_{x_w^+}^{x_e} w_m \, dx$ and $\mathcal{V}_1(y + \Delta y) = \tilde{\mathcal{V}}_1(y + \Delta y)$.

From these two properties of $\tilde{\mathcal{V}}_1$, it follows that an exact solution to $\mathcal{V}_{1w}(y)$ can be

[11] That is because $\mathcal{V}_{1w}(Y_i) = \tilde{\mathcal{V}}_{1w}(Y_i)$ is known at points where $W_m > 0$, hence the entrainment $\int_{Y_i}^{Y_{i-1}} W_m \, dy'$ can be calculated exactly in (104). On the other hand, when $W_m = 0$ at a point, one *assumes* that $\int_{Y_i}^{Y_{i-1}} W_m \, dy' = 0$, although one knows only that $\int_{Y_i}^{Y_{i-1}} W_m \, dy' \leq \tilde{\mathcal{V}}_{1w}(Y_i) - \mathcal{V}'_{1w}(Y_i)$. Hence an error is introduced in case $W_m > 0$ at anywhere in the interval $[Y_i, Y_{i-1}]$.

obtained by choosing the discrete points in (104) such that a Y_i is located at the southern edge of each continuous region where $\tilde{\mathcal{V}}_{1y} > \int_{x_w^+}^{x_e} w_m\, dx$. In case $W_m > 0$ at one point within such a region north of Y_i, it follows from the second property above that $W_m(Y_i) > 0$, and hence $\mathcal{V}_1 = \tilde{\mathcal{V}}_1$ in (104) is exact. If no entrainment occurs in a region with $\tilde{\mathcal{V}}_{1y} > \int_{x_w^+}^{x_e} w_m\, dx$, it follows from the first property that $W_m = 0$ throughout $[Y_1, Y_{i-1}]$, and hence (104) is exact as well. The points Y_i are found by solving $\tilde{\mathcal{V}}_{1y} = \int_{x_w^+}^{x_e} w_m\, dx$, and are local minima of $\tilde{\mathcal{V}}_1$ in regions without interior entrainment.

Solution: Now, we apply the algorithm derived above to obtain a solution for the western-boundary layer. The first step is to obtain the transport and the entrainment at $y = y_2$. To the north of that latitude, where the ocean is unstratified, the southward western-boundary current has no baroclinic structure. When the current crosses y_2, Q starts to heat the upper part ($z > -h_{\min}$) of the flow to a temperature $T^* > T_n$ and forms a layer 1. As $g'(y_2) = 0$, so that the baroclinic term vanishes, $\mathcal{V}_{1w}$ is given by the barotropic part in (101). Consistently, the formal application of (104) with $Y_1 = y_2$ and $Y_o = y_2^+$ yields the preliminary transport $\mathcal{V}'_{1w}(y_2) = 0$, as $\mathcal{V}_{1w}(y_2^+) = 0$ and the third term in (104a) vanishes in the limit $y_2^+ \to y_2$. It follows that $W_m > 0$ in (104b) and (104c), and that at y_2 it is

$$\int_{y_2}^{y_2^+} W_m\, dy = -\frac{h_{\min}}{D}\frac{\tau_y^x}{\beta}(x_e - x_w) \equiv \mathcal{W}_m(y_2). \tag{106}$$

Furthermore, $\mathcal{V}_{1w}(y_2) = -\left(h_{\min}/D\right)\left(\tau_y^x/\beta\right)(x_e - x_w)$, which is then the northern-boundary condition for further integration.

We proceed by determining the boundary-layer transports and entrainment shown in Figure 22, which correspond to the example with $H_s = 250\,\mathrm{m}$ and $\tau_o = 0.12\,\mathrm{N/m^2}$, and $\gamma_c > 1$, so that Region B extends to y_2 in the north (compare Figure 21). First, we show that $\tilde{\mathcal{V}}_{1y} > \int_{x_w^+}^{x_e} w_m\, dx$ in the interval $[\hat{y}_1, \hat{y}_2]$ using the continuity equation, (95a) and (103),

$$\tilde{\mathcal{V}}_{1y} - \int_{x_w^+}^{x_e} w_m\, dx = \tilde{\mathcal{V}}_{1wy} + U_{1w}^+ = -\frac{D - h_{\min}}{D}\frac{g'_y}{2f}h_{\min}^2 > 0, \qquad \hat{y}_1 \le y \le \hat{y}_2. \tag{107}$$

Furthermore, as $\mathcal{V}_1 = \tilde{\mathcal{V}}_1$ and $W_m > 0$ at y_2, it follows from (107) that $W_m = -\frac{D-h_{\min}}{D}\frac{g'_y}{2f}h_{\min}^2 > 0$ at all $\hat{y}_1 \le y < y_2$, and hence $\mathcal{V}_1 = \tilde{\mathcal{V}}_1$ and $\mathcal{V}_{1w} = \tilde{\mathcal{V}}_{1w}$ (compare Figure 22). Interestingly, the baroclinic part of $\mathcal{V}_{1w}$ vanishes entirely throughout that region, because $h_w = h_w^+ = h_{\min}$, and hence there is no zonal, baroclinic pressure difference across the boundary layer.

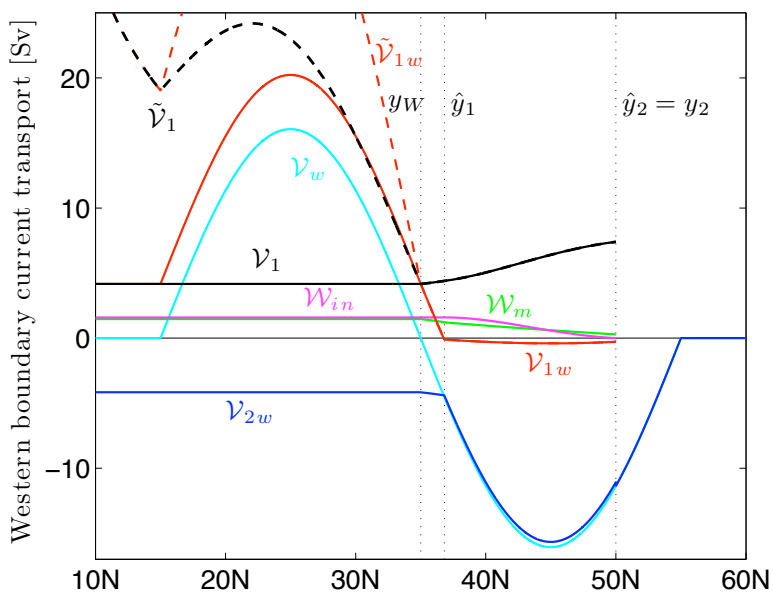

Figure 22: Latitudinal profiles of western-boundary-current transports in the upper ($\mathcal{V}_{1w}$, red curve), and deep layer ($\mathcal{V}_{2w}$, blue curve), corresponding to the interior solution shown in Figure 21 with $H_s = 250\,\mathrm{m}$ and $\tau_o = 0.12\,\mathrm{N/m^2}$. Also shown are the barotropic, boundary-current transport $\mathcal{V}_w$ (cyan curve), the total, meridional, layer-1 transport $\mathcal{V}_1$ (black curve), and the interior (magenta curve) and western-boundary (green curve) entrainment integrated southward from y_2. The maximal, meridional (western-boundary-current) transport $\tilde{\mathcal{V}}_1$ ($\tilde{\mathcal{V}}_{1w}$) is indicated by the dashed black (red) curve. All transports are in Sverdrup, and for orientation the latitudes y_W, $\hat{y}_1$ and $\hat{y}_2$ are indicated as vertical, dotted lines.

At $y < \hat{y}_1$, (14), (88) and (103) can be used to write the maximal, meridional transport as

$$\tilde{\mathcal{V}}_1 = \frac{g_s'}{2f}H_s^2 - \frac{\tau^x}{f}(x_e - x_w^+) + \frac{\tau_y^x}{\beta}(x_e - x_w^+)\left(\frac{h_{\min}}{D}\theta(-\mathcal{V}_w) + \theta(\mathcal{V}_w)\right) + \frac{g'}{2f}\left[-h_{\min}^2 - \frac{2}{3D}\left(h_w^{+3} - h_{\min}^3\right)\right]. \tag{108}$$

In the subpolar gyre at $y_W \leq y < \hat{y}_1$, the third and fourth terms are relatively small as h_W^+ and $h_{\min}$ are much smaller than D, and $h_{\min}^2$ smaller than H_s^2. As the first term varies only with f^{-1}, it follows that $\mathcal{V}_{1y} > 0$ because of the second term (the Ekman transport), which increases with y. Consequently, $W_m > 0$, $\mathcal{V}_1 = \tilde{\mathcal{V}}_1$ and $\mathcal{V}_{1w} = \tilde{\mathcal{V}}_{1w}$, as can be seen in Figure 22. In the subtropical gyre at $y < y_W$, on the other hand, the third term in (108) becomes important and $\mathcal{V}_{1y} < 0$ in the northern part of the gyre, so that $\mathcal{V}_1$ has a minimum at y_W. Thus, $Y_2 = y_W$ has to be used in (104) for $y < y_W$. Consistently, Figure 22 indicates that

$\mathcal{V}_1 < \tilde{\mathcal{V}}_1$, $\mathcal{V}_{1w} < \tilde{\mathcal{V}}_{1w}$ and $W_m = 0$ to the south of y_W. Furthermore, $\tilde{\mathcal{V}}_1$ has a second minimum at the southern edge of the subtropical gyre. No entrainment occurs there, however, because the southward Ekman transport weakens to the south of y_r and f in the first term in (108) decreases towards the Equator.

Interestingly, a minimum of $\tilde{\mathcal{V}}_1$ at some latitude y_a near y_W is apparent in all solutions, as it is robustly derived from the maximal Ekman transport close to y_W, and the different values for the barotropic part of $\tilde{\mathcal{V}}_{1w}$ to the north and south of y_W (Equation 102), but western-boundary-layer entrainment does not always occur. As that entrainment has important implications for the MOC (see Section 5.5 and Chapter 7), however, it is useful to understand what conditions result in $W_m(y_a) > 0$. Recall that $\mathcal{V}_1(y_2) = \tilde{\mathcal{V}}_1(y_2)$, and that $\mathcal{V}_{1y} > 0$ (Equation 105). Hence $\tilde{\mathcal{V}}_1(y_a) < \tilde{\mathcal{V}}_1(y_2)$ is a necessary condition or $W_m(y_a) > 0$, and the relationship $\tilde{\mathcal{V}}_1(y_a) = \tilde{\mathcal{V}}_1(y_2)$, can then easily be solved for a critical $H_s = H_a$,

$$H_a^2 = h_{\min}^2 + \frac{2f}{g_s'}\left[-\frac{D - h_{\min}}{D}\frac{\tau_y^x}{\beta}(x_e - x_w)\right]_{y=y_2} + \frac{2f}{g_s'}\left(\frac{\tau^x}{f} - \frac{h_{\min}}{D}\frac{\tau_y^x}{\beta}\right)(x_e - x_w) \text{ at } y = y_a. \tag{109}$$

It follows that the dimensionless parameter

$$\gamma_a = \frac{H_a^2}{H_s^2} \tag{110}$$

necessarily takes values $\gamma_a > 1$ for western-boundary entrainment to occur.

5.3 Solution with mixing by w_d

In this section, detrainment w_d is included in VLOM, so that it has a northern-boundary layer (Region 2), as for solutions without wind forcing (Section 3.3). Although it is possible to obtain particular solutions by integrating Rossby-wave characteristics from the eastern boundary, it is no longer possible to derive an exact general solution, which can illustrate the dependence of the solution on model parameters (*e.g.*, H_s and τ_o). Here, we therefore consider a "conceptual" solution that is a good approximation to the exact one.

Specifically, we assume that the steady-state response is the $w_d = 0$ solution in Section 5.2 everywhere along the eastern boundary and in the interior ocean, except where $h_1 \geq h_{\max}$

and in that region w_d is active (Region 2). Accordingly, the southern edge of the northern-boundary layer, $y''(x)$, lies along the curve $x_H(y, H)$ defined in (89) with $H = h_{\max}$. We also assume that w_d is just strong enough (t_d is small enough) so that (58) holds at x_w^+ in Region 2, which allows a simple expression for the MOC strength (see Section 5.5). This conceptual solution is not exact because eastern-boundary characteristics from south of $y_e'' \equiv y''(x_e)$ do not fill all of Region 1. That is, the northernmost part of Region 1 is filled by characteristics from north of y_e'' and therefore pass through Region 2 first (compare Fig. 20, where characteristics intersect with h_1-contours in Region A). As a result, the actual y'', given by the characteristic originating from (x_e, y_e''), runs slightly south of the one assumed in the "conceptual" solution. Furthermore, as h_1 thins in Region 2 along characteristics even without w_d (compare Eq. 85), the form of (23d) does not really ensure that h_1 approaches $h_{\max}$ along characteristics. Nonetheless, the "conceptual" solution reasonably reproduces the essential features of the exact response, that is a thinning of h_1 due to Rossby-wave damping in a northern boundary layer, and the strength of that damping is measured by $h_{\max}$.

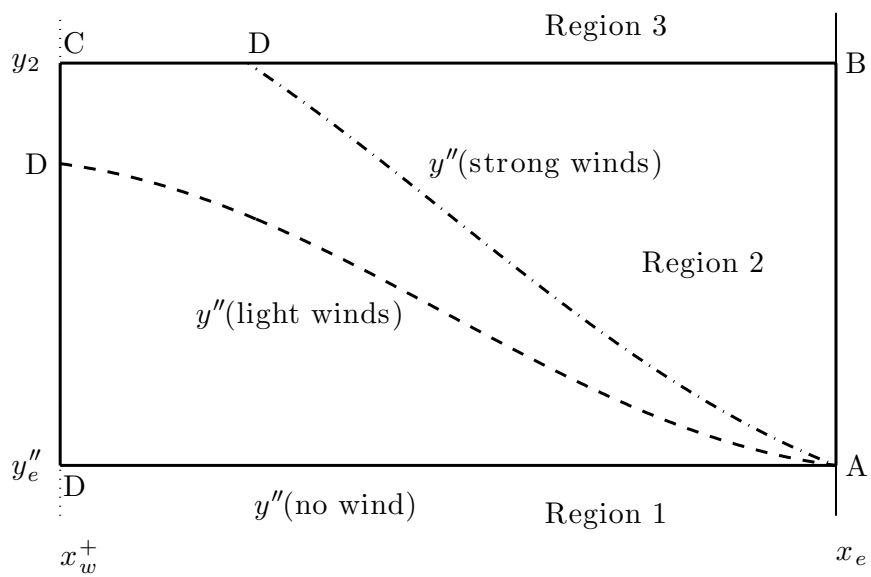

Figure 23: Schematic x-y map of the northern-boundary layer and its boundaries for solutions with no wind, light winds ($\gamma_c < 1$) and strong winds ($\gamma_c > 1$). The corners of the boundary layer are defined as A $= (x_e, y_e'')$, B $= (x_e, y_2)$, C $= (x_w^+, y_2)$ and D $= (x_w^+, y''(x_w^+))$ as $\gamma_c \leq 1$ and D $= (\hat{x}(y_2), y_2)$ as $\gamma_c > 1$.

Figure 23 provides a schematic of the boundaries of Region 2 for different wind strengths.

The corners of Region 2 are located at A $= (x_e, y_e'')$, B $= (x_e, y_2)$, C $= (x_w^+, y_2)$, and either D $= (x_w^+, y''(x_w^+))$ or D $= (\hat{x}_1(y_2), y_2)$, point C needed only when $y''(x)$ intersects the western boundary ($\gamma_c < 1$). In the limit $\tau_o \to 0$, $y''(x) = y_e''$ and the northern-boundary layer has exactly the same form as in Section 3.3. When $\tau_o > 0$, however, $y''(x)$ bends northward since, according to (88), the layer interface rises to the west due to Ekman suction. Consequently, D $= (x_w^+, y''(x_w^+))$ shifts northward as τ_o increases. Eventually, τ_o becomes large enough for y'' to intersect the line $y = y_2$ ($\gamma_c = 1$), and for large τ_o ($\gamma_c > 1$) the northern-boundary layer intersects the northern boundary so that D $= (\hat{x}_1(y_2), y_2)$.

Outside the northern-boundary layer and along $y''(x)$, the horizontal transports are given by (14) in Region A and by (95) in Region B. If $\gamma_c < 1$, so that the northern boundary intersects the western boundary, the zonal flow across x_w^+ is given by

$$U_{1w}^+ = -\frac{D - h_{\max}}{D}\frac{g_y'}{2f}h_{\max}^2 - \frac{h_{\max}}{D}\frac{\tau_{yy}^x}{\beta}(x_e - x_w^+), \qquad y_w'' \le y \le y_2, \tag{111}$$

where $y_w'' \equiv y''(x_w^+)$. If $\gamma_c \ge 1$, the flow into the western-boundary layer, U_{1w}^+, is not affected by w_d at all. Since we do not solve for the solution in Region 2, the detailed structure of w_1 is not known there. The important quantity for evaluating overturning strength, however, is the integrated detrainment $\mathcal{M}_n = \int_{R_2} w_1 \, dA$, which is derived in Section 5.5.

The western-boundary solution is obtained by the same procedure as for the $w_d = 0$ solution (Section 5.2.2.3). When $\gamma_c \ge 1$, the western-boundary current is not affected by the existence of northern boundary layer at all. When $\gamma_c < 1$, however, additional western boundary entrainment may appear just south of y_2 if $U_{1w}^+ > -\tilde{\mathcal{V}}_{1wy}$. It follows that entrainment occurs for $h_{\max} < \hat{H}$, where $\hat{H}$ is given by the solution to the third-order polynomial[12]

$$\hat{H}^3 - \frac{6f\tau_{yy}^x(x_e - x_w^+)}{\beta g_y'}\hat{H} = 3Dh_{\min}^2 - 2h_{\min}^3 - \frac{6f\tau_{yy}^x(x_e - x_w^+)}{\beta g_y'}h_{\min}, \tag{112}$$

and all variables are evaluated at $y = y_2$. In the limit $\tau_o \to 0$, (112) gives the same $\hat{H}$ as (52) for the solution without winds, as it should. As τ_o increases, $\hat{H}$ decreases for the solutions considered here since $\tau_{yy}^x(y_2) > 0$, and so the western-boundary entrainment near

[12] In the northern part of the subpolar gyre $\tau_{yy}^x > 0$, so that both terms on the l.h.s. of (112) are positive, and the polynomial has only one real solution.

y_2 decreases as well. If $h_{\max} < \hat{H}$, the southward extent of entrainment is calculated by solving $U_{1w}^{+} = -\tilde{\mathcal{V}}_{1wy}$, which then gives a latitude Y_2 and the boundary-current transport, $\mathcal{V}_{1w}(Y_1) = \tilde{\mathcal{V}}_{1w}$, which then serves as the northern-boundary condition for further southward integration of (100), as described in Section 5.2.2.3.

5.4 Three-dimensional circulation

As for the solutions without winds, we now consider the z-dependent circulation for the solutions discussed above. The interior velocities are given by (24). The Ekman flow is confined to a layer at the top of layer 1, which in (24) is a δ-function in the limit that vertical mixing vanishes. Below the Ekman layer, the flow is geostrophic, one part being the geostrophic part of the Sverdrup circulation, and the other due to thermal-wind shear. At the eastern boundary, where the upper-layer thickness is given by h_e, and the zonal component of Sverdrup flow vanishes, zonal velocities (just to the west of an eastern boundary layer where water sinks) are the same as in the solutions without winds (compare left panel of Fig. 8). Recall that the shear part of the thermal wind is eastward near the surface and westward near the bottom of the upper layer. It follows then, that away from the eastern boundary, the eastward gyre flow is surface intensified, whereas in regions with westward Sverdrup flow, velocities are the largest near the bottom. This is illustrated in the left panel of Figure 24, which shows the upper 1000 m of a y-z section of zonal velocities in a VLOM solution in the interior ocean without mixing ($w_d = 0$). Near y_2 ($= 50°$N), where the layer is deep, the depth-averaged velocities are relatively small and the vertical shear is large. As a result, velocities are eastward in the upper part of the layer, although the Sverdrup transport is directed to the west. In Region B ($42°\text{N} \lesssim y \lesssim 47°\text{N}$ in Fig. 24) where $h_1 = h_{\min}$, both zonal-velocity components are small; the Sverdrup part because it is distributed over the entire water column and $|\tau_{yy}^{x}|$ is small, and the shear part because the upper layer is thin.

As the zonal velocities near the eastern boundary are the same as in the solutions without winds, the coastal sinking (63) remains unchanged (see right panel of Fig. 8). Away from the eastern boundary, vertical motion is determined by the Ekman pumping [Note that the third and fourth terms balance on the r.h.s. of (24b)], and hence $w > 0$ to the south and

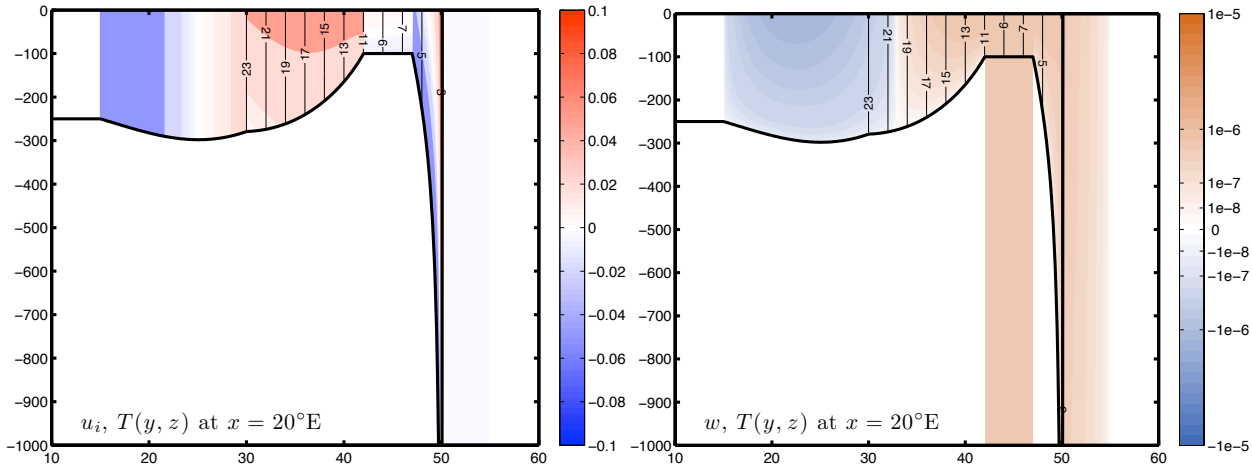

Figure 24: Meridional sections of depth-dependent, zonal velocities (shading, left panel) and vertical velocities w (shading, right panel) at $x = 20°$E, for the VLOM solution with $H_s = 250\,\mathrm{m}$, $\tau_o = 0.12\,\mathrm{N/m^2}$, $h_{\min} = 100\,\mathrm{m}$, $D = 4000\,\mathrm{m}$ and $w_d = 0$. The thick, black curve indicates the layer interface, and thin contours correspond to isotherms.

$w < 0$ to the north of y_r (compare right panel of Fig 24). Furthermore, w is confined to the upper layer in Region A, whereas the Ekman pumping extends to the bottom in Region B ($42°\mathrm{N} \lesssim y \lesssim 47°\mathrm{N}$ in Fig. 24) and to the north of y_2 ($= 50°\mathrm{N}$). As the interior sinking is then confined to the upper ocean in the subtropical gyre, deep sinking of cold water occurs only near the eastern boundary, and is identical as in the solutions without winds.

5.5 Overturning strength

In this section, we define measures for the strength of the wind and buoyancy-driven MOC $\mathcal{M}$, and for its components: the formation of deep water $\mathcal{M}_n$, the entrainment in Region B, $\mathcal{W}_{in}$, and the western-boundary entrainment $\mathcal{W}_w$. To keep the discussion of these transports somewhat concise, we concentrate on the dependence on the upper-layer thickness H_s and the strength of the winds τ_o, although other parameters (such as the width of the basin or the position of the the outcropping line relative to the wind forcing) may also be important in determining the strength and structure of the MOC.

Transport $\mathcal{M}_n$, defined in (64), is a measure of the total detrainment that occurs near y_2. In contrast to the solution without winds discussed in Chapter 3, $\mathcal{M}_n$ can be non-zero

in solutions with winds even without a northern boundary layer ($w_d = 0$).

When $w_d = 0$, (64) reduces to $\mathcal{M}_n = -\mathcal{W}_c$, and all detrainment occurs when water flows northward across y_2 and is cooled to T_n. If $\gamma_c \leq 1$ so that water detrains over the entire width of the basin, the northward convergence is given by

$$\mathcal{W}_c = -\int_{x_w}^{x_e} V_1(y_2)\,dx = \frac{\tau_y^x}{\beta}(x_e - x_w), \qquad y = y_2,\ \gamma_c \leq 1, \tag{113a}$$

that is, by the total Sverdrup transport across y_2. If $\gamma_c > 1$ so that detrainment occurs only east of $\hat{x}(y_2)$,

$$\mathcal{W}_c = \frac{\tau_y^x}{\beta}(x_e - \hat{x}) = -\frac{g_s'}{2f}H_s^2\frac{-\tau_y^x/\beta}{\tau^x/f - \tau_y^x/\beta} \equiv -\frac{g_s'}{2f}H_s^2 C_\tau \qquad y = y_2,\ \gamma_c > 1, \tag{113b}$$

where (89) is substituted in the second step. Interestingly, Equation (113b) has the same form as that for $\mathcal{W}_d$ without winds (61), except that $\bar{f} = f(y_2)$, and the factor C_τ is determined by the winds instead of mixing ($h_{\max}$). Furthermore, C_τ depends only on the shape of the forcing function $\tau^x(y)$, but not on its amplitude τ_o. Since $\tau^x > 0$, $\tau_y^x < 0$ and $\tau^x/f < -\tau_y^x/\beta$ in the subpolar gyre in the present solutions, it follows that $\frac{1}{2} < C_\tau < 1$, with C_τ being close to one in the northern part of the gyre, where the Ekman transport is small.

In the upper panel of Figure 25 $\mathcal{M}_n(H_s) = \mathcal{W}_c(H_s)$ is plotted for solutions with $\tau_o = 0.12\,\mathrm{N/m^2}$ (blue curve). It increases proportional to H_s^2 for $H_s < H_c = 300\,\mathrm{m}$ ($\gamma_c > 1$), consistently with (113b), and is constant for $H_s > H_c$ ($\gamma_c < 1$) as in (113a). In the lower panel of Figure 25 $\mathcal{M}_n(\tau_o) = \mathcal{W}_c(\tau_o)$ is shown. Let the critical, wind-forcing amplitudes τ_a, τ_b and τ_c be the value of τ_o where $\gamma_a = 1$, $\gamma_b = 1$ and $\gamma_c = 1$ respectively. For $\tau_o < \tau_c \approx 0.12\,\mathrm{N/m^2}$ ($\gamma_c < 1$), the detrainment $\mathcal{W}_c(\tau_o)$ then increases linearly with τ_o, in agreement with (113a), and for $\tau_o > \tau_c$ ($\gamma_c > 1$), $\mathcal{W}_c(\tau_o)$ is constant, consistently with (113b).

When $w_d \neq 0$ and the solution has a northern boundary layer, $\mathcal{M}_n$ is calculated using the convergence theorem, which states that in steady state, the detrainment in the northern boundary layer is identical to the flow across its boundaries. Figure 23 plots a schematic for the boundaries of the northern boundary layer. Since $\boldsymbol{V}_1 = 0$ north of y_2 and at the eastern boundary, the net flow into the boundary layer is given by the the flow across y'', and, if

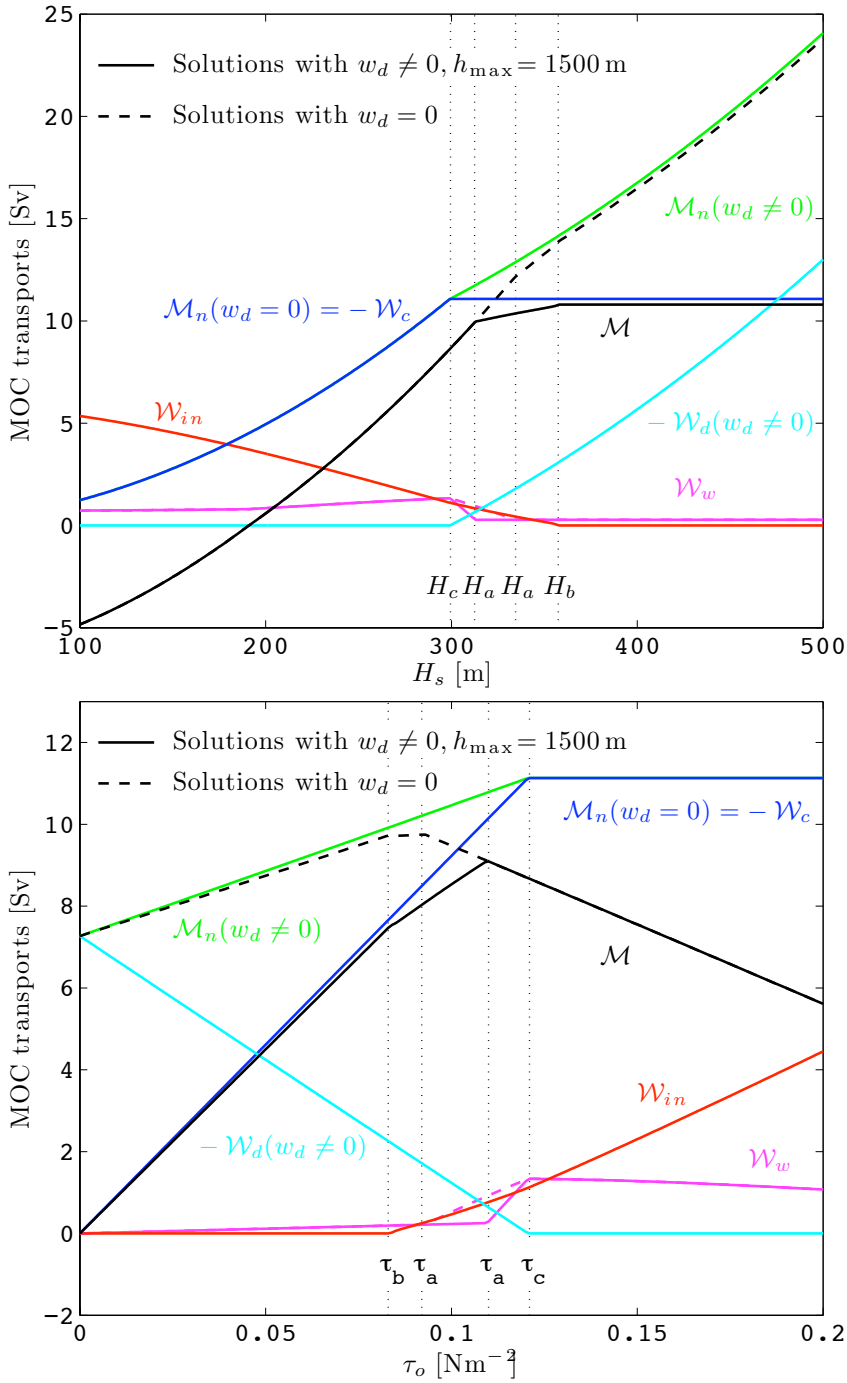

Figure 25: The different components of the MOC in VLOM, $\mathcal{M}$ (solid/dashed black line for $w_d = 0/w_d \neq 0$), $-\mathcal{W}_c$ and $\mathcal{M}_n$ for $w_d = 0$ (blue curve), $\mathcal{M}_n$ for $w_d \neq 0$ (green curve), $-\mathcal{W}_d$ for $w_d \neq 0$ (cyan curve), $\mathcal{W}_{in}$ (red curve) and $\mathcal{W}_w$ (solid/dashed magenta line for $w_d = 0/w_d \neq 0$) as a function of H_s with $\tau_o = 0.12\,\mathrm{N/m^2}$ in the upper and of τ_o with $H_s = 300\,\mathrm{m}$ in the lower panel. All transports are in Sverdrup, and $h_{\max} = 1500\,\mathrm{m}$ in solutions with $w_d \neq 0$. The critical latitudes H_a, H_b and H_c and wind strengths τ_a, τ_b and τ_c are indicated by vertical, dotted lines. The larger H_a and smaller τ_a correspond to the solutions with $w_d \neq 0$.

$\gamma_c < 1$, the zonal transport across x_w^+. Hence the detrainment is given by

$$\mathcal{M}_n = \int_{y_w''}^{y_2} U_{1w}^+(x_w^+)\, dy + \int_{y_e''}^{y_w''} \boldsymbol{V}_1 \cdot \boldsymbol{n}\ dy'', \tag{114}$$

where U_{1w}^+ is given by (111) and $\boldsymbol{n}$ is the unit vector normal to y''. Although the relative contributions of $\mathcal{W}_c$ and $\mathcal{W}_d$ cannot be precisely determined without a solution within the northern boundary layer, it is useful to define $\mathcal{W}_c$ by (113), so that it is the same as in the case without mixing; $\mathcal{W}_d$ is then given by $\mathcal{W}_d = \mathcal{M}_n - \mathcal{W}_c$. Substitution into (114) gives then

$$\mathcal{W}_d = \left\{ \frac{g'(y_w'')}{g'(y_e'')} \frac{g_s'}{2\bar{f}} H_s^2 - \left[\frac{\tau_y^x}{\beta}(x_e - x_w^+) \right]_{y_w''}^{y=y_2} \right\} \frac{D - h_{\max}}{D}, \tag{115}$$

where $\bar{f}^{-1} = -\left[1/g'(y_w'')\right] \int_{y_w''}^{y_2} \left(g_y'/f\right) dy$, (47) is substituted as $g_s' H_s^2 = g'(y_e'') h_e^2(y_e'')$, (113a) is used, and $[F]_b^a \equiv F(a) - F(b)$. Note that (115) is consistent with (61) in the limit $\tau_o = 0$.

Figure 25 plots $\mathcal{M}_n$ for solutions with mixing ($h_{\max} = 1500\,\mathrm{m}$)[13] as a grgreeneen line. Since $\mathcal{W}_d = 0$ for $H_s \leq H_c$ ($\gamma_c \geq 1$), $\mathcal{M}_n$ and the large scale MOC do not depend on the northern-boundary layer, and hence $\mathcal{M}_n = \mathcal{W}_c$ as in the case with $w_d = 0$ (blue line). For $H_s > H_c$ ($\gamma_c < 1$), $\mathcal{W}_d$ (cyan line) becomes important, and it allows for $\mathcal{M}_n(H_s)$ to become larger than $\mathcal{M}_n(H_c)$, which is an upper limit of $\mathcal{M}_n$ in solutions without mixing. The lower panel of Figure 25 shows how $\mathcal{M}_n(\tau_o)$ (green curve) increases with the strength of the winds, although $\mathcal{W}_d$ (cyan curve) decreases, until it reaches its maximum $\mathcal{M}_n(\tau_c)$.

To illustrate the dependence of $\mathcal{M}_n$ on H_s and τ_o in more detail, the upper panel of Figure 26 plots $\mathcal{M}_n(H_s)$ for various values of τ_o. For all solutions with $w_d = 0$ (solid curves), $\mathcal{M}_n(H_s)$ is independent of τ_o, until it reaches a maximum $\mathcal{M}_n(H_c)$, and then remains constant for $H_s \geq H_c$. The maximum $\mathcal{M}_n(H_c)$ and critical layer thickness H_c vary among the solutions, however, and are both increasing with the strength of the wind. For solutions with $w_d \neq 0$ (dashed lines), $\mathcal{M}_n(H_s)$ deviates from the results without mixing only for $H_s > H_c$, where $\mathcal{M}_n$ continues to grow due to $\mathcal{W}_d$.

[13] Whereas the MITgcm results in Section 4.4 give a range in which the mixing depth $h_{\max}$ may be chosen for solutions without winds, it is not clear whether similar values apply for solutions with winds or how $h_{\max}$ depends on the strength of the winds. Thickness $h_{\max} = 1500\,\mathrm{m}$ is used for the solutions shown, since that value for $h_{\max}$ is approximately estimated for large H_s in the solutions without winds, and the overturning strength is independent of $h_{\max}$ in solutions with $H_s < H_c$.

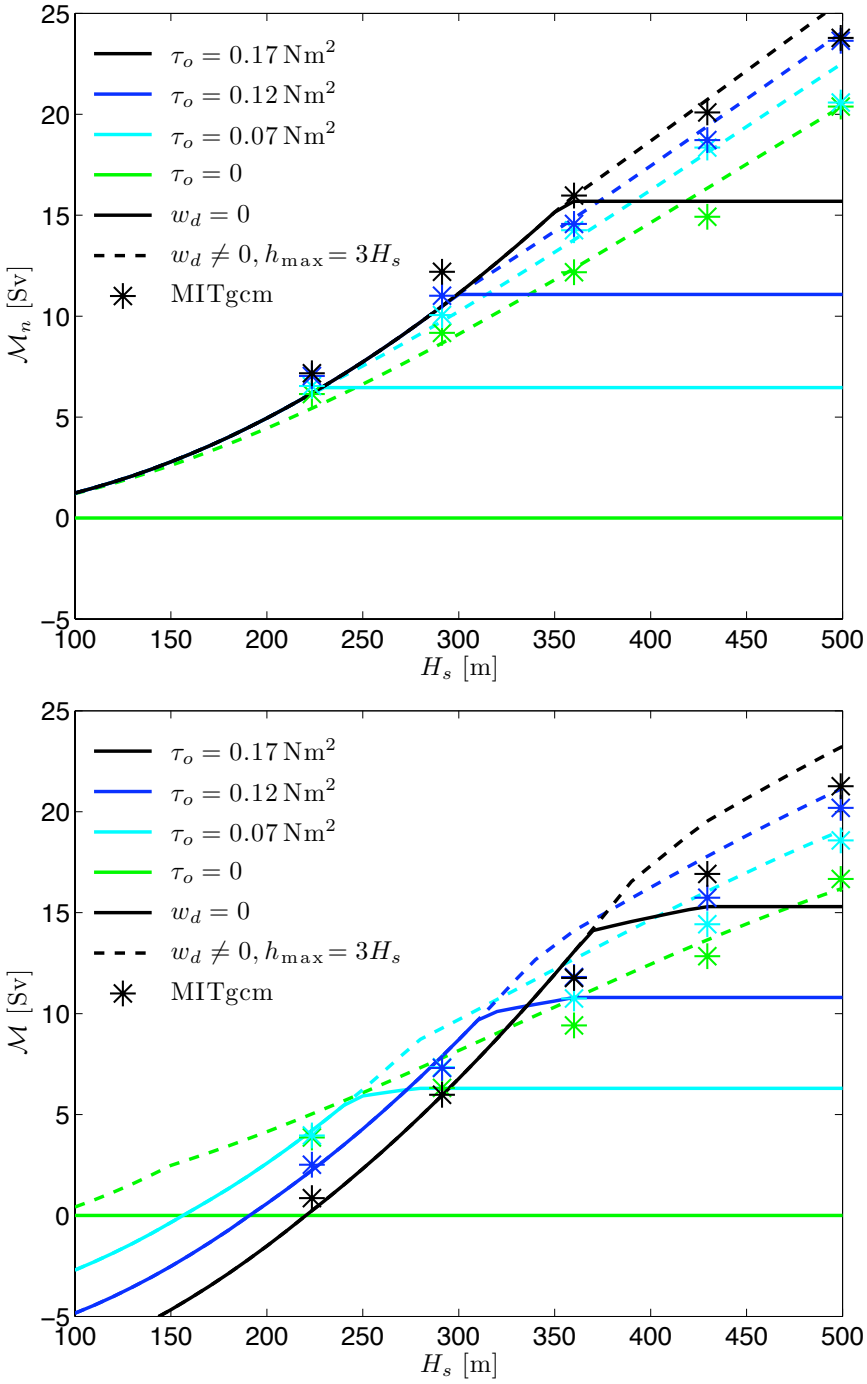

Figure 26: Plots of $\mathcal{M}_n$ (upper panel) and $\mathcal{M}$ (lower panel) in VLOM as a function of H_s for $\tau^x = 0$ (green), $0.07\,\mathrm{N/m^2}$ (cyan), $0.12\,\mathrm{N/m^2}$ (blue) and $0.17\,\mathrm{N/m^2}$ (black) for the case without w_d (solid lines) and with w_d ($h_{\max} = 1500$ m, dashed lines). Also shown are MITgcm data points (diamonds), indicating $\max(\psi^T)$ in the upper and $\max(\psi^T(y_W))$ in he lower panel, and using the same color code as for the VLOM solutions. The unit of the transports is Sv.

Interior entrainment in Region B occurs only for $\gamma_b > 1$ defined in (94), as there is no Region B otherwise. Since $w_1 = 0$ in Region A, and the flow across the eastern boundary vanishes, the convergence theorem can be used to write the integral over all entrainment in Region B (R_B) as

$$\mathcal{W}_{in} \equiv \int_{R_B} w_1 \, dA = \int_{\hat{x}(\hat{y}_2)}^{x_e} V_1(\hat{y}_2) dx - \int_{x_w^+}^{x_e} V_1(\hat{y}_1) \, dx - \int_{\hat{y}_1}^{\hat{y}_2} U_{1w}^+ \, dy. \tag{116}$$

Note that the lower limit of the first integral is chosen such that if $H_s \leq H_c$ so that Region B extends to y_2, the entrainment of the southward surface flow (95b) across y_2 to the west of $\hat{x}(y_2)$ is included in $\mathcal{W}_{in}$. Substitution of the transports (14) and (95a) and accounting for the current (97) at the southwestern corner of Region B gives for the interior subpolar gyre entrainment

$$\mathcal{W}_{in} = \frac{D - h_{\min}}{D} \left[\frac{\tau_y^x}{\beta} (x_e - x_w^+) \right]_{\hat{y}_2}^{y=\hat{y}_1} + \left[\frac{\tau_y^x}{\beta} (\hat{x} - x_w^+) \right]^{y=\hat{y}_2} - \frac{h_{\min}}{D} \frac{[g']_{\hat{y}_2}^{y=\hat{y}_1}}{2\hat{f}} h_{\min}^2 - \mathcal{V}_B(\hat{y}_1), \tag{117}$$

where $\hat{f}^{-1} = (\rho^*(\hat{y}_1) - \rho^*(\hat{y}_2))^{-1} \int_{\hat{y}_2}^{\hat{y}_1} (\rho_y^*/f) dy$ is an average over f^{-1}.

While (117) is useful to calculate the entrainment in a particular solution, it is not as useful for understanding how $\mathcal{W}_{in}$ behaves as a function of H_s and τ_o, because it depends on $\hat{y}_1$ and $\hat{y}_2$. Since the latitudes $\hat{y}_1$ and $\hat{y}_2$ strongly depend on the shape of the wind forcing function and geometry (Huang and Flierl, 1987), however, it is not straightforward to make general statements on the strength of $\mathcal{W}_{in}$, other than that it vanishes for $\gamma_b < 1$, that is $H_s > H_b$ or $\tau_o < \tau_b$, and that it is proportional to τ_o and inversely proportional to H_s in case $\gamma_b > 1$. That behavior can also be seen in Figure 25, where $\mathcal{W}_{in}$ is indicated by the red curves, and $H_b \approx 358\,\mathrm{m}$ and $\tau_b \approx 0.85\,\mathrm{N/m^2}$.

The total western-boundary-layer entrainment outside of the southern sponge layer is defined as $\mathcal{W}_w \equiv \int_{y_s'}^{y_2} W_m \, dy$. In all solutions, $\mathcal{W}_w > 0$, as entrainment (106) always occurs, when the barotropic boundary current flows southward across y_2 and an upper layer is formed by surface heating. The amount of entrainment at that latitude is of the order $(h_{\min}/D)\,\mathcal{M}_n$, however, and relatively small compared to the MOC.

Larger amounts of western-boundary entrainment are generated at latitudes where the net sinking farther to the north, that is $\mathcal{M}_n$ minus the upwelling to the north of that latitude, is larger than the maximum upper-layer meridional transport that can be maintained by

model, $\tilde{\mathcal{V}}_1$. In the present solutions, that occurs near y_W, and as all interior entrainment takes place at $y > y_W$, the boundary-layer entrainment is given by

$$\mathcal{W}_w = \mathcal{W}_m(y_2) + \left[\mathcal{M}_n - \mathcal{W}_{in} - \tilde{\mathcal{V}}_1(y_W)\right] \theta \left[\mathcal{M}_n - \mathcal{W}_{in} - \mathcal{W}_m(y_2) - \tilde{\mathcal{V}}_1(y_W)\right]. \tag{118}$$

In Figure 25, $\mathcal{W}_w$ is indicated by the solid (dashed) magenta lines for solutions with $w_d = 0$ ($w_d \neq 0$). As $\mathcal{W}_w = \mathcal{W}_m(y_2)$ for $\gamma_a < 1$, $\mathcal{W}_w$ is slightly larger for $H_s < H_a$ ($H_a \approx 313\,\mathrm{m}/335\,\mathrm{m}$ for the solutions with $w_d = 0/\ w_d \neq 0$), but still remains relatively small compared to the other transports. Nonetheless $\mathcal{W}_w$ is dynamically important, as it sets essentially an upper limit for the MOC transport to the south of y_W, which is given by

$$\tilde{\mathcal{V}}_1(y_W) = \frac{g'}{2f}\left[h_e^2 - h_{\min}^2 - \frac{2}{3D}\left(h_e^3 - h_{\min}^3\right)\right] - \frac{\tau^x}{f}(x_e - x_w) \quad @ \quad y = y_W. \tag{119}$$

Whereas $\mathcal{M}_n$ measures the northward convergence of upper-layer flow and hence the formation rate of deep water, it is not a good measure for the strength of the MOC south of the subpolar ocean because entrainment in the subpolar gyre ($\mathcal{W}_{in}$ and $\mathcal{W}_w$) may significantly reduce the MOC further to the south. Therefore, it is useful to define a new measure for the deep-water export,

$$\mathcal{M} \equiv \mathcal{M}_n - \mathcal{W}_{in} - \mathcal{W}_w. \tag{120}$$

In case western boundary entrainment occurs at y_W ($\gamma_a < 1$), it follows directly from substitution of (118) that $\mathcal{M} = \tilde{\mathcal{V}}_1(y_W)$ is given by (119). As a result, the deep-water export is independent of its formation rate $\mathcal{M}_n$ in this parameter range. This can also be seen in Figure 25, where $\mathcal{M}(H_s)$ (upper panel) and $\mathcal{M}(\tau_o)$ are plotted as solid black curves for $w_d = 0$ (dashed black lines for $w_d \neq 0$). In the upper panel, three different regimes are apparent. In the first one, as $H_s < H_a$ ($\gamma_a > 1$), $\mathcal{M}$ is indeed given by (119). Then there is a transition for $H_a \leq H_s \leq H_b$ indicated by a decrease in slope, where $\mathcal{W}_{in} > 0$, but western boundary entrainment occurs only at y_2, so that $\mathcal{M}$ is not limited by (119). Finally, when $H_s > H_b$, $\mathcal{M}$ is given by $\mathcal{M}_n - \mathcal{W}_m(y_2)$.

Interestingly, $\mathcal{M}(\tau_o)$ reaches a maximum at $\tau_a \approx 0.11\,\mathrm{N/m^2}$ for $w_d = 0$ ($\tau_a \approx 0.09\,\mathrm{N/m^2}$ for $w_d \neq 0$) in the lower panel of Figure 25. As a result, whether the deep-water export is proportional or inversely proportional to the strength of the winds depends on γ_a. For

$\tau_o > \tau_a$ ($\gamma_a > 1$), $\mathcal{M}(\tau_o)$ decreases according to (119). For $\tau_b < \tau_o < \tau_a$, $\mathcal{M}_n(\tau_o)$ and $\mathcal{M}_{in}$ are both increasing with τ_o, and as a result $\mathcal{M}(\tau_o)$ is nearly constant for $w_d \neq 0$, and increases slightly for $w_d = 0$. For $\tau_o < \tau_b$, $\mathcal{M}(\tau_o)$ is proportional to τ_o, as $\mathcal{W}_{in} = 0$.

The deep-water export $\mathcal{M}(H_s)$ is also shown in the lower panel of Figure 26, where it is plotted for various values of τ_o. Each solution has the same regimes as discussed for Figure 25, and the critical layer thicknesses H_a and H_b, where solutions shift from one regime into the other, increase with the strength of the winds. The figure also demonstrates that $\mathcal{M}$ is proportional to τ_o for large, but inversely proportional to τ_o for small values of H_s.

CHAPTER 6

MITgcm solutions driven by differential heating and winds

In this chapter, we report numerical solutions to the MITgcm forced by buoyancy forcing and zonal winds. We start by examining the circulation and density field, and the underlying dynamics in one particular, steady-state solution. Then we discuss the strength of overturning and its dependence on the forcing in a series of MITgcm experiments. Throughout both sections, we note similarities and differences to the VLOM solutions presented in Chapter 5, and the MITgcm solutions without winds (Chapter 4).

6.1 Solution

This section is organized as follows. We first discuss the barotropic circulation, then the temperature and velocity fields at the eastern boundary, the interior ocean and in the western boundary layer, and finally the strength and structure of the MOC. The solution's experimental design is described in Chapter 2.1, with $\Delta H_s = 100\,\mathrm{m}$, that is $H_s = 223\,\mathrm{m}$, and $\tau_o = 0.12\,\mathrm{N/m^2}$. To illustrate the solution, Figure 27 provides a map of the barotropic streamfunction, Figures 28 and 29 show y-z and x-z sections of temperature and velocity, an x-y map of the upper layer thickness h_1 is plotted in Figure 30, and plots of the MOC streamfunctions are shown in Figure 31.

6.1.1 Barotropic circulation: The map of the barotropic streamfunction (Figure 27) indicates that its maximum transports, 16 Sv in the subtropical gyre and 18 Sv in the

subpolar gyre, are close to the values in the VLOM solution (Figure 19). A difference from the VLOM solution is the finite width of the western-boundary layer, which takes up a considerable fraction of the relatively narrow basin.

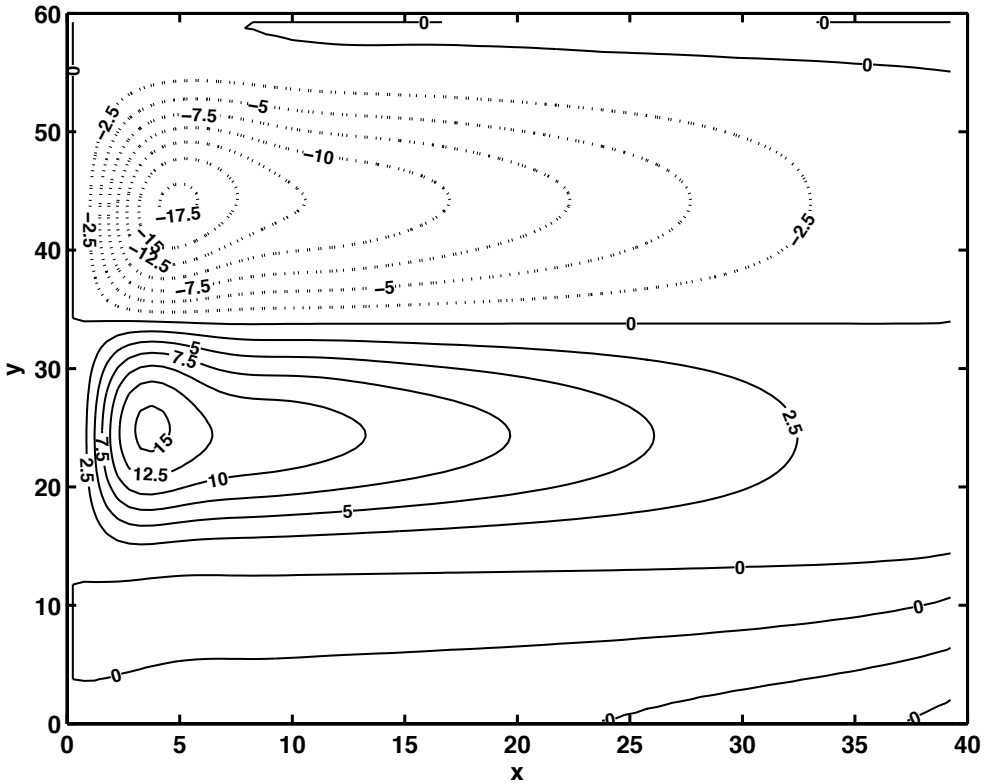

Figure 27: Plot of the barotropic streamfunction, $\Psi(x, y)$ in the MITgcm solution with τ^x = 0.12 N/m^2 and H_s = 223 m. The unit is Sverdrups.

6.1.2 Eastern boundary: The eastern-boundary temperature field, vertical velocities, and zonal velocities (the latter one grid point away from the boundary) are shown in the upper panels in Figure 28. As in the solution without winds (Figure 12), isotherms are vertical within and horizontal below the mixed layer, with the mixed-layer thickness $h_m(x_e)$ following very closely the curves described by (40) (magenta line). Consequently, the upper-layer thickness $h_1(x_e)$ (cyan) is very similar to h_e (47) in VLOM (compare Fig. 8). The zonal flow is confined to the region above $h_m(x_e)$, and it exhibits the now familiar, thermal-wind shear pattern, consisting of eastward flow at the top of the mixed layer and westward flow at its bottom. Strong isothermal sinking occurs within the mixed layer to

close that circulation. The solution also has the same secondary features as in the solution without winds, albeit somewhat weaker: a finite-width transition zone between the regions with horizontal and vertical isotherms, and upwelling (and also some downwelling) below the mixed layer.

6.1.3 Interior ocean: The sections at 10°E in the middle panels of Figure 28 illustrate that isotherms and h_1 are depressed in the subtropical gyre at 15°N$\leq y \leq$ 35°N, and raised away from the eastern boundary in the subpolar gyre at 35°N$\leq y \leq$ 55°N. The zonal flow is mostly confined to the upper layer, and goes in the direction of the gyre circulation, as in Region A in the VLOM solutions (compare to Fig. 24). There is also a region where h_1 is near $h_{\min}$ in the subpolar gyre (39°N$\lesssim y \lesssim$ 45°N), however, where the flow (and hence the Ekman pumping in the middle-right panel) extends over the entire water column, as in Region B. Furthermore, in the northern part of the subpolar gyre, the thermal-wind shear has about the same strength as the gyre flow, so that the flow is eastward near the surface.

The same, basic features are apparent in Figure 29. At 30°N, located within the subtropical gyre, the upper layer thickens markedly to the west and the meridional flow is directed to the south, that is the direction of gyre flow, and mostly confined to the upper layer. At 35°N along the boundary between the gyres and at 43°N, 48°N and 53°N within the subpolar gyre, isotherms rise away from the eastern boundary. Below a thin Ekman layer, the meridional, upper-layer flow is northward, as expected from the Sverdrup relation, and is also confined to the upper ocean. The section at 43°N is an exception, however, as isotherms are close to $h_{\min}$ at $y \lesssim$ 20°E, and the meridional flow extends over the entire water column. Consequently, the maps of layer thickness for the MITgcm (Figure 30) and VLOM solution (Figure 21) show the same basic features, including the eastward extend of Region B. A northern boundary layer at $y < y_2$ is apparent in Figure 30, where the eastward $\boldsymbol{V}_1$ is in the opposite direction than the Sverdrup circulation. Although such a boundary layer is not present in Figure 21, as mixing is excluded ($w_d = 0$) for that particular solution, the characteristics of that boundary layer are essentially as discussed in VLOM solutions with mixing in Chapters 3.3 and 5.3.

Despite these many similarities, the MITgcm solution also shows some (secondary) fea-

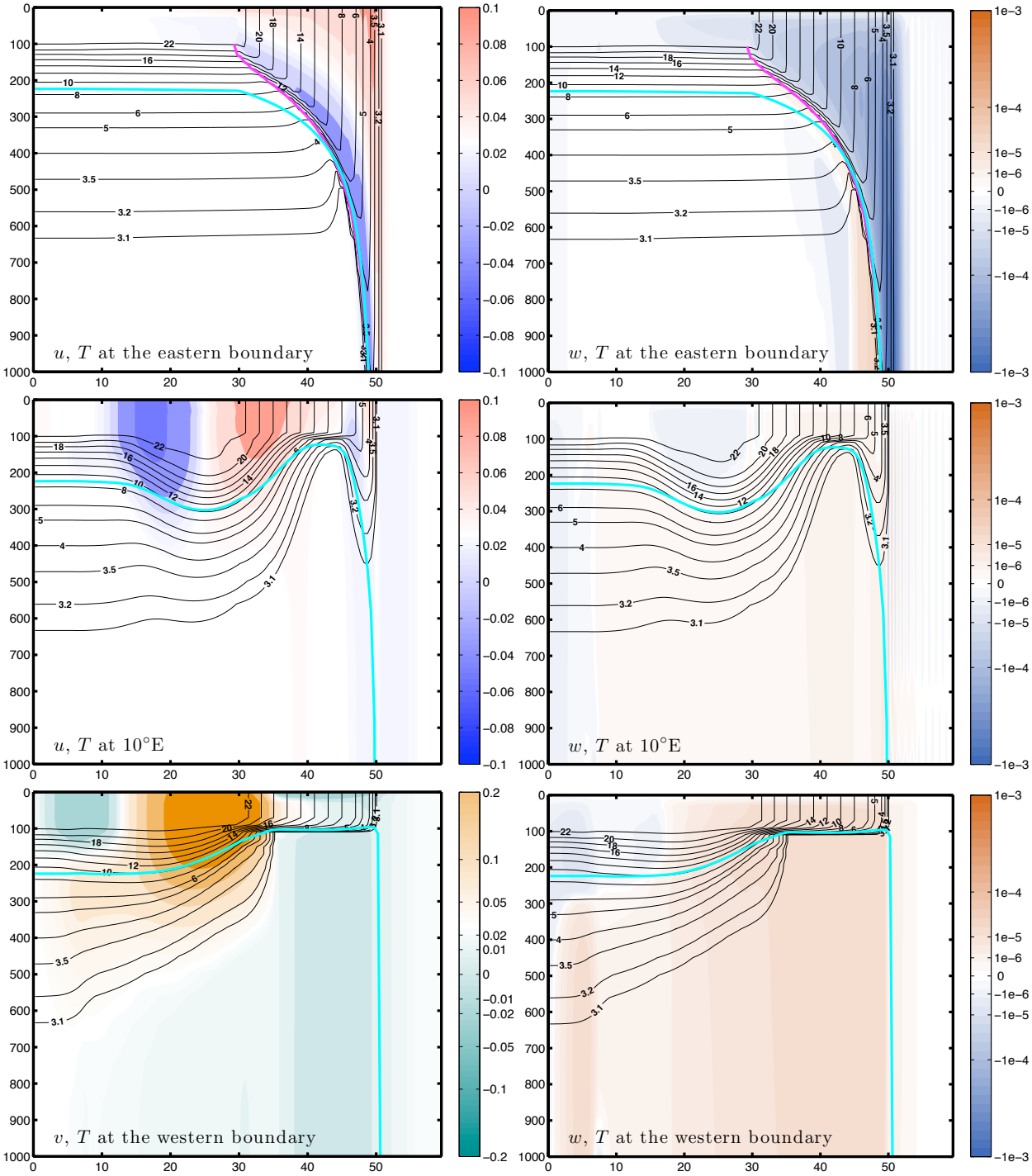

Figure 28: Meridional sections from the MITgcm run with $\tau_o = 0.12\,\mathrm{N/m^2}$ and $H_s = 223\,\mathrm{m}$ after 1000 years of integration, showing upper-ocean fields of temperature (contours) along the eastern boundary (top), 10°E (interior, near the western boundary), and the western boundary (bottom). The left column also plots zonal velocities in the top two panels and the meridional velocity in the bottom panel, the right column plots vertical velocities (shading).

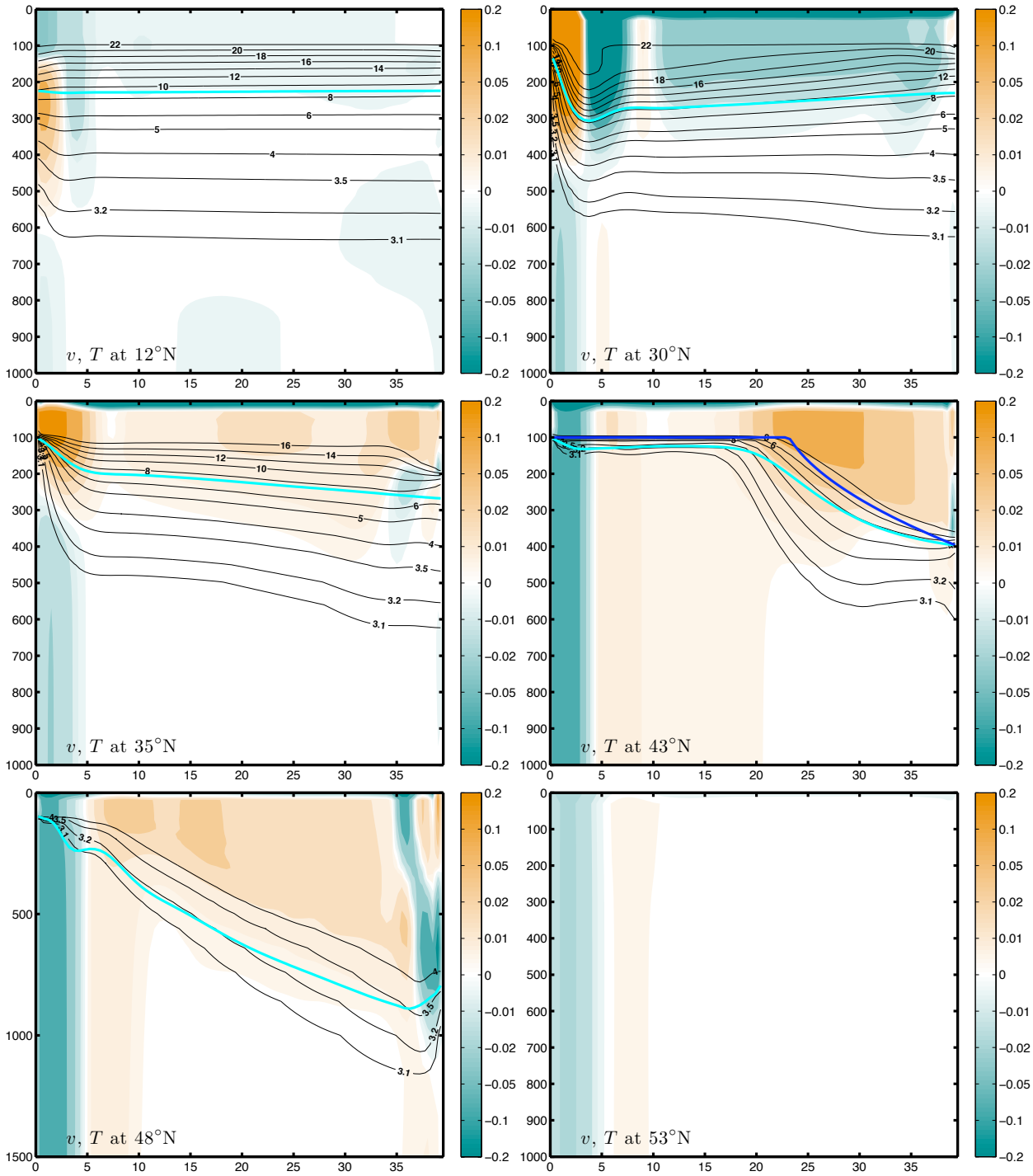

Figure 29: Zonal sections of upper-ocean v and T from the MITgcm solution with $\tau_o = 0.12$ N/m^2 and $H_s = 223$ m after 1000 years of integration, at $y = 12°$N (top-left), $y = 30°$N (top-right), $y = 35°$N (middle-left), $y = 43°$N (middle-right), $y = 48°$N (bottom-left), and $y = 53°$N (bottom-right). The layer interface h_1 in MITgcm is indicated by cyan curves and h_1 in VLOM by a blue curve in the middle-right panel.

tures, that are not explained by VLOM. As diffusion continues to deepen the thermocline at depths below the wind-driven upper-layer flow, a circulation somewhat similar to the Stommel and Arons (1960) circulation discussed in Chapter 4.2 develops there, which is characterized by weak, interior upwelling with a northward flow at depth. The horizontal flow at depth is so weak that it is invisible in the Figures, but the corresponding upwelling, which allows for an advective-diffusive balance in the steady state, can be seen in the middle-right panel in Figure 28. Furthermore, the zonal section at 12°N, which is located south of the subtropical gyre, shows some southward, near-surface flow, which is part of the upper branch of the Stommel and Arons (1960) circulation.

In the middle-right panel of Figure 29, h_1 of MITgcm (cyan) and VLOM (blue) are compared in a zonal section at 43°N. The comparison shows that the zonal gradient of layer thickness is larger in VLOM than it is in MITgcm. This difference can also possibly be explained by diffusive mixing, which is present in MITgcm but not in VLOM: in terms of layer-model processes, it acts as an entrainment velocity ($w_1 > 0$, *e.g.,* Kawase, 1987), and hence tends to thicken the upper layer away from the eastern boundary in steady state (see Eq. 26). As a result of this reduced layer-thickness gradient, the longitude $\hat{x}(y)$, where h_1 reaches $h_{\min}$ first, is shifted to the west, so that Region B is slightly smaller in MITgcm than it is in VLOM.

In the subtropical gyre at 30°N (upper-right panel in Figure 29), the interior Sverdrup flow has a southward component that crosses isotherms of $T^* = 23$°C, but T only remains near T^* for depths shallower than $h_{\min}$. At greater depths ($z < -h_{\min}$), cool water advects southward, cooling the subsurface water, and thereby stratifying the upper layer; this stratification contrasts to the VLOM solution in which Q acts throughout layer 1. Essentially, subduction is occurring in the MITgcm solution, a process that cannot be represented in a system with a single upper layer. Idealized models ($2\frac{1}{2}$-layer models) have been developed to describe this process (*e.g.,* Luyten et al., 1983; McCreary and Lu, 1994). It is noteworthy that this process does not occur in the interior, subpolar gyre, where the meridional, Sverdrup-flow component is northward, and surface cooling and convection ensure that the upper-layer temperature remains relatively uniform.

Finally, there are also eastern-boundary currents present in the zonal sections in Figure

29). In addition to the horizontal Ekman layer and the current at the bottom of the mixed layer, which are also present in the solutions without winds (Chapter 4), an eastern-boundary Munk layer is expected in the solution, as the interior, meridional, depth-averaged, upper-layer flow does not vanish and no-slip conditions are applied at the horizontal boundaries. Interestingly, these boundary layers do not significantly affect (disturb) the density field, either along the eastern boundary or away from coast.

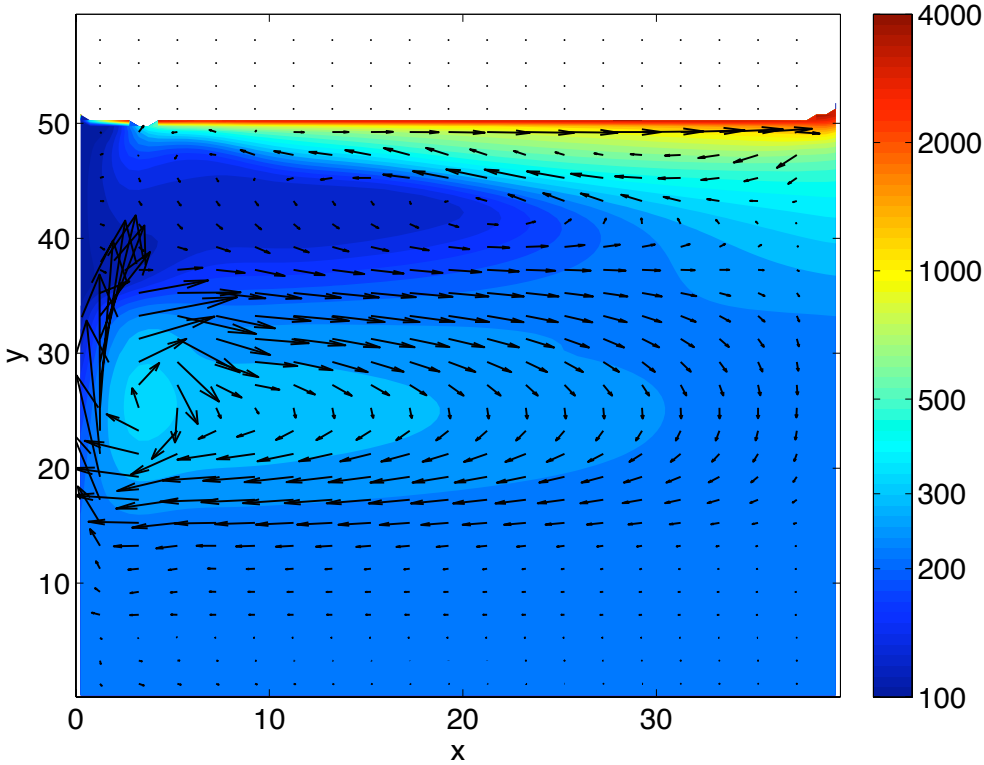

Figure 30: Map of layer thickness h_1 and V_1 in the MITgcm solution with $\tau^x = 0.12$ N/m^2 and $H_s = 223$ m.

6.1.4 Western boundary layer: The bottom panels of Figure 28 show meridional velocities, vertical velocities, and isotherms in a meridional section along the western boundary. In the subpolar gyre, all isotherms are near $h_{\min}$ before they outcrop, and the current is southward without showing much baroclinic structure. South of the latitude y_W, where the wind curl is positive, isotherms are depressed and the flow is northward near the surface and southward at depth, albeit weaker than in the subpolar gyre. Interestingly, the upwelling

weakens and the coastal h_1 deepens abruptly south of y_W in all solutions where $h_1 \approx h_{\min}$ at $y > y_W$ (not shown). To ensure that this property also holds in VLOM, the barotropic part of $\mathcal{V}_{1w}$ is approximated as in (102) there. South of the subtropical gyre, the western boundary current is southward near the surface, likely a consequence of the circulation being closed in the sponge layer. Finally, the zonal Munk (1950) layer structure of the western boundary current is revealed in Figure 29, as a strong recirculation to the east of the main branch adjacent to the coast is apparent in all sections.

6.1.5 Overturning circulation:

Figure 31 plots the meridional streamfunctions, $\psi(y, z)$ and $\psi^T(y, T)$. The $\max(\psi) = 6.8\,\mathrm{Sv}$ is about 10% smaller than in the solution without winds (compare Figure 15), but is also located right at $y_2 = 50°\mathrm{N}$. Upwelling is stronger in the subpolar gyre, and almost all upwelling occurs within the basin, that is, the upwelling in the sponge layer is negligible.

The maximum of the temperature streamfunction, $\max(\psi^T) = 7.0\,\mathrm{Sv}$, located at y_2, occurs at 3.05°C. As in VLOM, where the flow across y_2 and hence the deep-water formation is enhanced by the winds, $\max(\psi^T)$ is 15% larger than for the solution without winds. Upwelling in the subpolar gyre is so strong, however, that the net flow of deep water out of the subpolar ocean is only $\max\left[\psi^T(y_W)\right] = 2.5\,\mathrm{Sv}$, compared to 4.5 Sv in the solution without winds. This increased upwelling is consistent with the entrainment processes in Region B ($\mathcal{W}_{in}$) and the western boundary layer ($\mathcal{W}_w$) in VLOM, and as a consequence downwelling occurs in the sponge layer at $y < y_s$.

As in similar OGCM solutions (*e.g.,* Bryan, 1991), where subtropical and subpolar overturning cells (STC and SPC) are present in the upper 500 m of the ocean, a strong subpolar cell can be seen in the upper panel of Figure 31. As τ^x does not extend to the equator in the present solution, however, the subtropical cell is absent. As shown by McCreary and Lu (1994), the strength of these cells is strongly related to subduction in the subtropical gyre, a process that is not resolved in VLOM. Since these shallow overturning circulations do not have major implications for the deep MOC, a more detailed discussion is omitted in this manuscript.

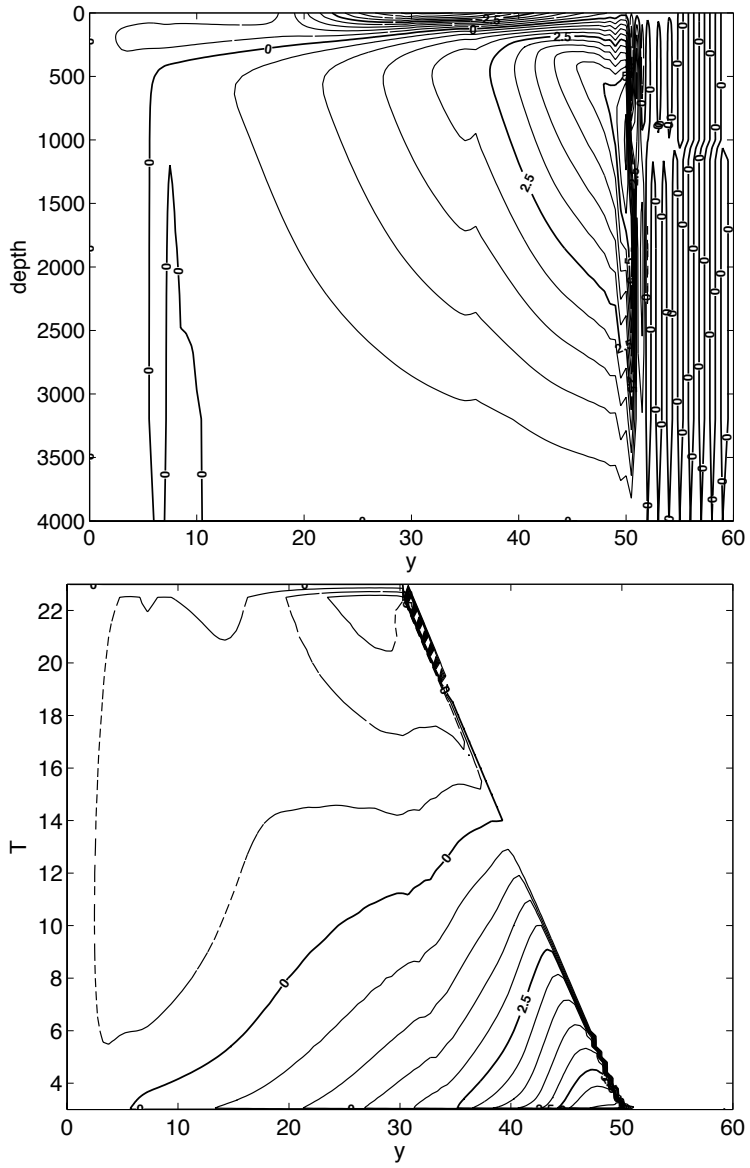

Figure 31: Plots of the streamfunctions $\psi(x, y)$ (upper panel) and $\psi^T(y, T)$ (lower panel) for the MITgcm solution with $H_s = 223$m and $\tau_o = 0.12\,\mathrm{N/m^2}$. The contour interval is $0.5\,\mathrm{Sv}$ in both figures.

6.2 Overturning strength

To investigate the dependence of the strength of the MOC on the thermocline thickness H_s and the strength of the wind forcing τ_o, a set of experiments has been conducted using various values for H_s and τ_o. Throughout the following discussion, we focus on two measures for the MOC: the deep-water formation rate, defined as for the solutions without wind, $\mathcal{M}_n \equiv \max(\psi^T)$, and the deep-water export from the subpolar ocean $\mathcal{M} \equiv \max\left[\psi^T(y_W)\right]$, given by the maximum of the streamfunction at the boundary of the subpolar and subtropical gyre.

The rate of deep-water formation $\mathcal{M}_n$ is indicated in the upper panel of Figure 26. As in VLOM, $\mathcal{M}_n$ is nearly independent of τ_o for the experiments with $H_s = 223\,\mathrm{m}$, but proportional τ_o as H_s increases. This general agreement suggests that the processes determining the upper-layer flow convergence into the region north of y_2, where it is cooled to T_n and transformed to deep-layer water is similar among the two models.

On the other hand, $\mathcal{M}_n$ tends to be slightly larger in MITgcm than in VLOM for smaller H_s and vice versa for larger H_s. A possible explanation for this difference is that diffusive mixing is included in MITgcm, but not in VLOM. As a result, Region B is smaller and its eastern boundary $\hat{x}(y_2)$ is slightly shifted to the west in MITgcm compared to VLOM (for more details, see the discussion in Section 6.1.3). As $\mathcal{M}_n$ is proportional to $\hat{x}(y_2)$ only for relatively small H_s ($\gamma_c > 1$), the discrepancy among the models is consistent with (113). Another reason for the difference at larger H_s ($\gamma_c < 1$) is that $\mathcal{M}_n$ then depends on the northern boundary layer in VLOM, and hence on the poorly constrained parameter $h_{\max}$.

The strength of the deep-water export $\mathcal{M}$ is shown in the lower panel of Figure 26. Irrespectively of the winds, $\mathcal{M}$ is proportional to the thermocline thickness H_s. As $\mathcal{M}$ increases faster with H_s for stronger winds, however, $\mathcal{M}$ is inversely proportional to τ_o for small H_s and proportional to H_s for large H_s. These general properties are the same as in the VLOM solutions, and $\mathcal{M}$ in MITgcm and VLOM are in a remarkably good agreement when the thermocline is relatively shallow. On the other hand, the results differ considerably when H_s is large.

As for $\mathcal{M}_n$, congruities and discrepancies are consistent with the dynamical picture de-

rived for VLOM and the effects of diffusion in MITgcm. When H_s is relatively small, and the winds relatively strong, ($\gamma_a > 1$) western-boundary entrainment $\mathcal{W}_w$ occurs in VLOM. As a result, $\mathcal{M} = \tilde{\mathcal{V}}_1(y_W)$ is set to the maximal, meridional, upper-layer transport that can be maintained by the model (Eq. 119), and which is independent of the entrainment and detrainment processes further to the north. It follows that an additional (diffusive) entrainment in the subpolar gyre does not affect $\mathcal{M}$, as long as that entrainment is not strong enough to allow for h_1 to become thicker than $h_{\min}$ at y_W, and to eliminate $\mathcal{W}_w$. The good agreement among the models in this regime suggests that the maximal meridional upper-layer transport $\tilde{\mathcal{V}}$ is set by similar dynamics in both models. In solutions without strong western boundary entrainment ($\gamma_a < 1$), on the other hand, $\mathcal{M}$ is given by the sum of all entrainment and detrainment processes to the north of y_W. In that case, the additional diffusive entrainment in MITgcm weakens $\mathcal{M}$ relative to VLOM, and hence can explain the discrepancies for larger H_s.

CHAPTER 7

VLOM solutions with an MOC closed by physical entrainment processes

In the previous chapters, solutions are closed by a sponge layer at the southern boundary in which H_s is externally prescribed. Here, the VLOM solutions in Chapter 5 are extended to allow for closure by an upwelling branch, in which H_s is determined as part of the solution. Deriving detailed solutions for the southern ocean or including the effects of diffusion outside the northern boundary layer is beyond the scope of this study. Therefore, the upwelling branch is implemented in a conceptual way, as in the model of Gnanadesikan (1999). A description of the Gnanadesikan (1999) model and how it is merged with the VLOM is provided in Section 7.1, solutions are reported in Section 7.2, and some conclusions are discussed in Section 7.3.

7.1 The model

The Gnanadesikan (1999) model subdivides the ocean into two reservoirs with light and dense waters (top panel of Figure 32). To reach an equilibrium state, the thermocline thickness H_s is adjusted until the various transports across the boundary of the reservoir are balanced: $\mathcal{V}_n(H_s)$ in the north, $\mathcal{W}_{mix}(H_s)$ at the bottom, and $\mathcal{V}_s(H_s)$ in the southern ocean. As in VLOM, buoyancy forcing ensures that density remains constant in time in each reservoir. The equations for the transports are

$$\mathcal{V}_n = C_n H_s^2, \qquad \mathcal{W}_{mix} = \frac{\kappa_v A}{H_s}, \qquad \mathcal{V}_s = \mathcal{V}_{EK} - C_{eddy} H_s, \tag{121}$$

where $\mathcal{V}_n$, depending on a constant factor C_n and H_s^2, is identical to (1). Transport $\mathcal{W}_{mix}$ represents the entrainment via diffusive mixing and depends on the vertical (diapycnal) diffusivity κ_v, the mixing or entrainment area A and H_s^{-1}. Transport $\mathcal{V}_s$ represents an upper-ocean mass flux from the Southern Ocean, and it has a wind-driven $\mathcal{V}_{EK}$ (Wyrtki, 1961; Toggweiler and Samuels, 1995) and eddy-driven $\mathcal{V}_{eddy}$ components, the latter depending on a constant C_{eddy} and H_s. The solution proceeds by setting

$$\mathcal{V}_n = \mathcal{W}_{mix} + \mathcal{V}_s, \tag{122}$$

which provides an equation that can be solved for H_s.

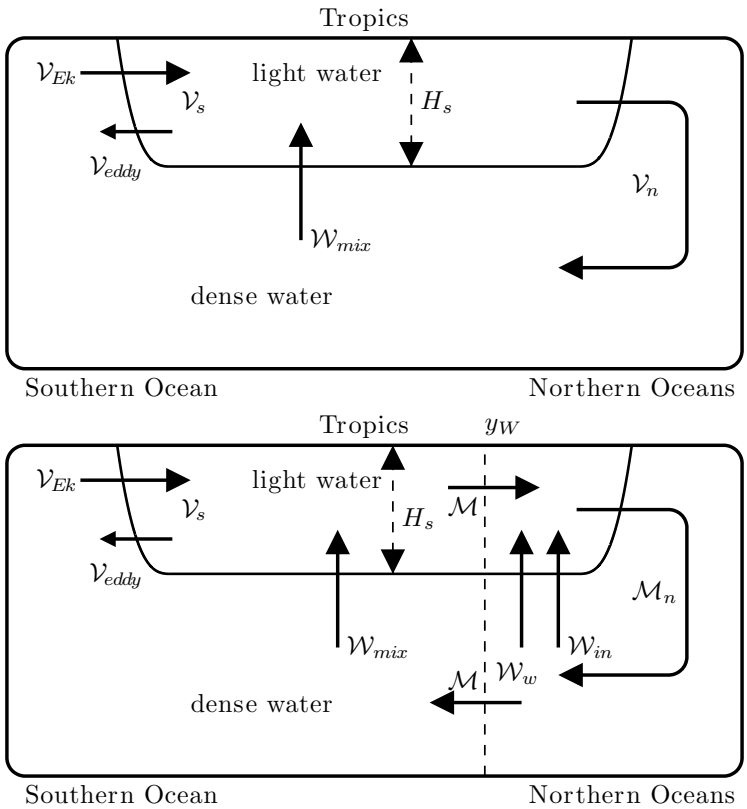

Figure 32: Schematic of the model used in Gnanadesikan (1999) (upper panel), and in the modified version of VLOM considered here (lower panel). In the VLOM version, the solution from Section 5 is used to solve for transports in the northern-hemisphere, subpolar gyre.

In applying the Gnanadesikan (1999) model to VLOM (bottom panel of Figure 32), $\mathcal{V}_n$ is replaced by the deep-water export from the subpolar ocean, $\mathcal{M} = \mathcal{M}_n - \mathcal{W}_{in} - \mathcal{W}_w$,

which is the sum of the northward convergence and deep water formation $\mathcal{M}_n$, the interior wind-driven entrainment $\mathcal{W}_{in}$, and the western-boundary-layer entrainment $\mathcal{W}_w$, as derived in Chapter 5 (For convenience, the VLOM equations are rewritten in the box below). The VLOM solution is then obtained by the replacing (122) with

$$\mathcal{M} = \mathcal{W}_{mix} + \mathcal{V}_s, \tag{123}$$

which can be iterated to obtain H_s.

VLOM transports:

(i) The deep-water formation rate

$$\mathcal{M}_n = \begin{cases} \frac{-\tau_y^x}{\beta}(x_e - x_w) + \frac{D-h_{\max}}{D}\left(\frac{g'(y_w'')}{g'(y_e'')}\frac{g_s'}{2f}H_s^2 - \left[\frac{\tau_y^x}{\beta}(x_e - x_w)\right]_{y_w''}^{y=y_2}\right), & \gamma_c \le 1, \\ \frac{-\tau_y^x/\beta}{\tau^x/f - \tau_y^x\beta}\frac{g_s'}{2f}H_s^2, \qquad y = y_2, & \gamma_c \ge 1. \end{cases}$$

(ii) The entrainment in the interior subpolar-ocean outcropping region

$$\mathcal{W}_{in} = \begin{cases} 0, & \gamma_b \le 1, \\ \frac{D-h_{\max}}{D}\left[\frac{\tau_y^x}{\beta}(x_e - x_w)\right]_{\hat{y}_1}^{y=\hat{y}_1} + \left[\frac{\tau_y^x}{\beta}(\hat{x} - x_w)\right]^{y=\hat{y}_2} - \frac{h_{\min}}{D}\frac{[g']_{\hat{y}_1}^{y=\hat{y}_1}}{2\hat{f}}h_{\min}^2 - \mathcal{V}_B(\hat{y}_1), & \gamma_b \ge 1. \end{cases}$$

(iii) The entrainment in the subpolar-ocean western-boundary layer

$$\mathcal{W}_w = \begin{cases} \mathcal{W}_m \equiv -\frac{h_{\min}}{D}\frac{\tau_y^x}{\beta}(x_e - x_w), \qquad y = y_2, & \gamma_a \le 1, \\ \mathcal{M}_n + \mathcal{W}_m - \mathcal{W}_{in} - \frac{g'}{2f}\left[h_e^2 - h_{\min}^2 - \frac{h_e^3 - h_{\min}^2}{3D/2}\right] + \frac{\tau^x}{f}(x_e - x_w), \quad y = y_W, & \gamma_a \ge 1, \end{cases}$$

In these equations, τ^x is the wind-stress, f the Coriolis parameter and β its meridional gradient, g' is the reduced gravity, and g_s' is the reduced gravity in the tropics, where the eastern-boundary layer thickness h_e takes the value H_s. The thickness $h_{\max}$ is the maximum upper-layer thickness set by mixing processes, $h_{\min}$ the minimum upper-layer thickness maintained by "mixed-layer" processes, and D the ocean depth. The longitude x_e corresponds to the eastern boundary, x_w to the western boundary, and $\hat{x}(y)$ to the longitude where the upper layer thickness reaches $h_{\min}$ first in the subpolar ocean. The latitude y_2 separates the regions with and without an upper layer, y_e'' denotes the

southern boundary of the northern boundary layer at the eastern and y''_w at the western boundary. The latitudes $\hat{y}_1$ and $\hat{y}_2$ correspond to the to the southern and northern extent of the interior subpolar-ocean outcropping region. The transport $\mathcal{V}_B$, corresponding to the boundary current transport given by (97), but its contribution is negligible in the solutions presented here.

7.2 Solutions

Solutions to three versions of (123) are reported that explore the MOC's sensitivity to the strength of the westerlies (τ_o) on the northern hemisphere. The domain of the first system is a single closed basin, and solutions are obtained by solving (123) with $\mathcal{V}_s = 0$ so that the upwelling branch is only driven by interior diffusion. The second and third systems both include a Pacific basin that is connected to the Atlantic by the Southern Ocean, and they retain both terms on the right-hand side of (123). Both systems allow entrainment in the Pacific basin due to interior diffusion by $\mathcal{W}_{mix}$; they differ in that the third system also allows wind-driven entrainment in the North Pacific subpolar gyre (active) but the second does not (passive). The parameters used in all three solutions are given in Table 1. Results are shown in Figure 33. Generally, as τ_o increases solutions shift between different dynamical regimes. Specifically, the γ_α parameters ($\alpha = a, b, c$) defined in Chapter 5 change from being less than one to greater than one. In the following, points on the τ_o-axis where $\gamma_\alpha = 1$ are labelled τ_α, and the slopes of curves change abruptly at these points.

For the solutions in a single, closed basin, all VLOM parameters have the same values as for the solutions in Chapter 5. The depth-independent diffusive mixing parameter is $\kappa_v = 4 \times 10^{-5}\,\mathrm{m}^2/\mathrm{s}$ and the entrainment area $A = 2 \times 10^{13}\,\mathrm{m}^2$. With these parameter choices, $\mathcal{W}_{mix}$ is approximately as strong as in the VLOM standard solution discussed in Schloesser et al. (2011). Since the basin is closed at the southern boundary, there is no mass exchange between the reservoirs in a southern ocean, and (123) is solved with $\mathcal{V}_s = 0$. Results are shown in the upper panels of Figure 33, which plot various transports (top-left panel) and layer thicknesses (top-right panel) vs. τ_o.

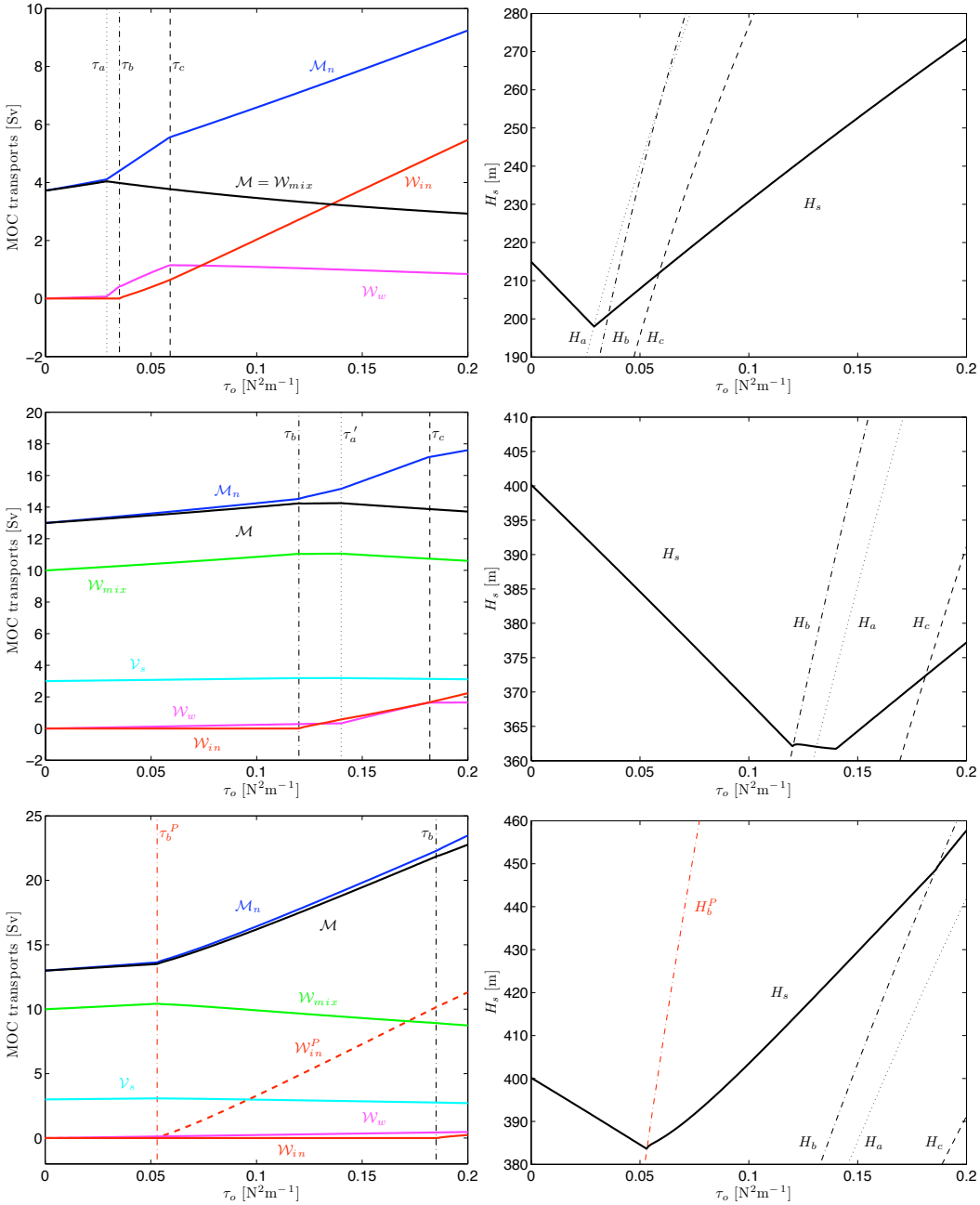

Figure 33: Transports of MOC branches (left panels) and H_s (right panels) for the VLOM solutions discussed in Chapter 7, showing the closed-basin solution in the upper panels, and the solution with passive and active Pacific Oceans in the middle and lower panels, respectively. In the top-left panel, the transports plotted as a function of τ_o are $\mathcal{M}_n$ (blue), $\mathcal{M} \equiv \mathcal{M}_n - \mathcal{W}_{in} - \mathcal{W}_w = \mathcal{W}_{mix}$ (black), $\mathcal{W}_{in}$ (red) and $\mathcal{W}_w$ (magenta) in the upper panel, $\mathcal{V}_n$ (blue), $\mathcal{M} \equiv \mathcal{V}_n - \mathcal{W}_{in} - \mathcal{W}_w$ (black), $\mathcal{W}_{in}$ (red), $\mathcal{W}_w$ (magenta), $\mathcal{W}_{mix}$ (green) and $\mathcal{V}_s$ (cyan) in the middle panel. In the lower panel, solid curves correspond to the same transports as in the middle panel, and a red, dashed curves is added for $\mathcal{W}_{in}^P$ in the North Pacific. The right column shows H_s (solid curve) and H_a (dotted curve), H_b (dash-dotted curve) and H_c (dashed curve); black curves correspond to values in the Atlantic and red curves to the Pacific. The τ_α ($\alpha = a, b, c$), where H_α intersect with H_s in the right panels are indicated by vertical lines in the left panels.

Table 1: Parameters used in the three solutions discussed in this Chapter.

Parameter	Single basin	Passive Pacific	Active Pacific
κ_v [10^{-5} m^{2}s^{-1}]	4	4	4
A [10^{14} m^2]	0.2	1	1
$\mathcal{V}_{Ek}[Sv]$	0	5	5
C_{eddy} [10^3 m^{2}s^{-1}]	0	5	5
Width of the Atlantic	40°	40°	40°
Width of the Pacific	-	-	100°

For weak winds in the range, $0 \leq \tau_0 < \tau_a$ ($\tau_a \approx 0.03\,\mathrm{N/m^2}$), H_s is larger than all critical thermocline depths, H_α ($\gamma_\alpha < 1$). Therefore, no entrainment occurs in the subpolar gyre ($\mathcal{W}_{in} = \mathcal{W}_w = 0$) and $\mathcal{M}_n$ is balanced entirely by diffusive entrainment $\mathcal{W}_{mix}$. In this regime, the northward transport across y_2, $\mathcal{W}_c$ is then given by (113a), so that $\mathcal{M}_n$ is proportional to τ_o; in addition, H_s decreases for increasing τ_o in order for the balance $\mathcal{M}_n = \mathcal{W}_{mix}$ to hold (top-right panel of Figure 33). For winds in the range, $\tau_a \leq \tau_o < \tau_b$ ($\tau_a \approx 0.035\,\mathrm{N/m^2}$), entrainment occurs in the western-boundary layer of the subpolar gyre, and $\mathcal{W}_w$ contributes to the total upwelling. As $\mathcal{W}_{mix}$ is assumed to occur only south of the subpolar gyre, $\mathcal{M}$ is given by (119). Since $\mathcal{M}$ is then inversely proportional to τ_o for constant H_s, H_s has to increase with τ_o for the balance, $\mathcal{W}_{mix} = \mathcal{M}$, to hold. For $\tau_b \leq \tau_o < \tau_c$ ($\tau_c \approx 0.06\,\mathrm{N/m^2}$), the layer interface outcrops in the interior of the subpolar gyre, and the Ekman suction there generates an additional entrainment, $\mathcal{W}_{in}$, that also contributes to the total upwelling. Because the entrainment $\mathcal{W}_{in}$ is not strong enough to reduce $\mathcal{M}$ below the maximal, meridional transport that can be maintained by VLOM at y_W, $\tilde{\mathcal{V}}_1(y_W)$ (119), it does not increase the total upwelling in the subpolar gyre, but merely shifts the location from the western boundary to the interior. Therefore, $\mathcal{W}_{in}$ does not affect the MOC south of the subpolar gyre. Finally, for $\tau_o > \tau_c$, $\mathcal{M}_n$ becomes less sensitive to an increase in τ_o. This property is apparent in the top-left panel of Figure 33, where the slope of the blue curve decreases. Because the growth of $\mathcal{M}_n$ is smaller now than that of $\mathcal{W}_{in}$, $\mathcal{W}_w$ is reduced.

Nevertheless, this change does not affect the solution to the south of the subpolar gyre, where H_s continues to be determined by $\mathcal{W}_{mix} = \tilde{\mathcal{V}}_1(y_W)$.

In the second set of solutions (middle panels of Figure 33), the domain includes both an Atlantic and Pacific Ocean connected by the Southern Ocean, diffusive entrainment occurs everywhere in the Pacific basin, but no wind-driven entrainment is allowed in the Pacific subpolar gyre. To allow for diffusive entrainment in the Pacific, the area of diffusive entrainment is expanded to $A = 10^{14}\,\mathrm{m}^2$. In addition, wind-driven entrainment in the Southern Ocean is chosen to be $\mathcal{V}_{EK} = 5\,\mathrm{Sv}$ and $C_{eddy} = 5 \times 10^3\,\mathrm{m}^2/\mathrm{s}$, and both contribute to $\mathcal{V}_s$ in (123). Parameters for the North Atlantic are unchanged. Results are shown in the middle panels of Figure 33.

For small and very large τ_o, that is $\tau_o < \tau_\alpha$ or $\tau_o > \tau_\alpha$ with $\alpha = a, b, c$, the solution behaves essentially like the closed-basin solution discussed above. Since the upwelling branch is stronger because of the increased area in $\mathcal{W}_{mix}$ and the contribution of $\mathcal{V}_s$, however, the MOC is stronger, and H_s and the critical wind strengths τ_α are larger than in the previous solution. Furthermore, $\tau_b = 0.12\ \mathrm{N/m^2} < \tau_a = 0.13\,\mathrm{N/m^2}$, so that as τ_o increases, interior entrainment $\mathcal{W}_{in}$ occurs first as $\tau_o > \tau_b$. As a result, western-boundary entrainment, $\mathcal{W}_w$, occurs only when $\tau_o > \tau_a' = 0.14\ \mathrm{N/m^2} > \tau_a$, because $\mathcal{W}_{in}$ reduces the strength of the MOC to the north of y_W, so that $\mathcal{M} < \tilde{\mathcal{V}}_1(y_W)$ despite $\mathcal{M}_n > \tilde{\mathcal{V}}_1(y_W)$.

The active Pacific solution is an extension of the passive Pacific solution, the only difference being that a VLOM solution that allows for upwelling in the North Pacific subpolar gyre ($\mathcal{W}_{in}^P$) is included. For clarity, all variables in the North Pacific are indicated by a superscript P. The wind forcing is the same in both northern basins, and the relaxation temperature in the North Pacific is also given by (4), but with $y_2^P = y_n$, so that the subpolar gyre lies entirely in the region where $T^{*P} > T_n$. Finally, the mixing depth is $h_{\max}^P = D$, which shuts off all detrainment by w_d^P. With this choice of parameters, all deep-water formation is eliminated ($\mathcal{M}_n^P = \mathcal{W}_d^P = \mathcal{W}_c^P = 0$). The width of the Pacific is assumed to be 100°, 2.5 times the width of the North Atlantic (40°), but all other parameters, including the strength of the winds τ_o, are the same as in the North Atlantic. Furthermore, H_s also takes the same value in both oceans[14]. Results are shown in the bottom panels of Figure 33.

[14]The relation of the layer thicknesses in the Atlantic and Pacific has been explored in several idealized,

Since two VLOM solutions are included in the model, each solution is described by a different set of nondimensional parameters, γ_α and γ_α^P. In the North Pacific, only γ_b^P is relevant, since γ_a^P and γ_c^P have no meaning because there is no deep-water formation. Recall that γ_b^P determines whether the deep layer outcrops, and interior-ocean entrainment $\mathcal{W}_{in}^P$ occurs. Since the Pacific is much wider than the Atlantic, the deep layer outcrops for much weaker winds ($\gamma_b^P > \gamma_b$).

Transports and thermocline thickness are identical to the case with a passive Pacific only for $\tau_o \leq \tau_b^P = 0.05\,\mathrm{N/m^2}$. For $\tau_o > \tau_b^P$, the interior entrainment in the Pacific, $\mathcal{W}_{in}^P$, increases rapidly. That additional upwelling can only be balanced by increasing H_s, so that deep-water formation in the North Atlantic, $\mathcal{M}_n$, increases as well. As a result, H_s, and hence the τ_α, are larger than in the solution without entrainment in the Pacific, and the entrainments in the North Atlantic ($\mathcal{W}_{in}$ and $\mathcal{W}_w$) are essentially canceled for reasonable wind strengths $\tau_o < \tau_b \approx 0.18\,\mathrm{N/m^2}$.

7.3 Conclusions

In all three solutions, the equilibrium response to changes in the strength of the wind forcing depends on the particular state of the system, as described by the values of four parameters, γ_a, γ_b, γ_c, and γ_b^P. For relatively weak winds, when the westerlies in the northern hemisphere do not drive any upwelling in the subpolar gyre(s) (*i.e.*, γ_a, γ_b, $\gamma_b^P < 1$), an increase in τ_o decreases H_s, and causes a slight increase in overturning strength ($\mathcal{M}$ and $\mathcal{M}_n$). For larger τ_o (γ_a, γ_b, $\gamma_b^P > 1$), H_s grows proportional to τ_o, and the formation of deep water in the North Atlantic, $\mathcal{M}_n$, increases more rapidly. The deep-water export from the subpolar gyre in the Atlantic, $\mathcal{M}$, increases only in the solution with wind-driven entrainment $\mathcal{W}_{in}^P$ in the North Pacific, however, because the increase in $\mathcal{M}_n$ is overcompensated by upwelling in the subpolar gyre ($\mathcal{W}_{in}$, $\mathcal{W}_w$) in the other systems.

The critical strengths of the wind τ_α, at which the systems shift from one regime into

layer-model studies (*e.g.*, Huang et al., 2000; Johnson and Marshall, 2004), indicating that the difference in layer thickness between the two oceans is related to the (geostrophic) transport from one into the other. Although it is straightforward to implement such a relation in the present model, that step is omitted for simplicity.

the other, vary strongly among the three systems discussed above. As a result, the response to a change in the strength of the winds for a given τ_o can be completely different. For a (reasonable) value of $\tau_o = 0.11\,\mathrm{N/m^2}$, for example, the strength of overturning $\mathcal{M}$ is proportional to τ_o in the experiments with a Pacific and inversely proportional in the closed basin experiment. The thermocline thickness H_s, on the other hand, increases with τ_o in the closed-basin and the active-Pacific experiments, and decreases in the one with a passive Pacific. This example illustrates that it might be difficult (impossible) to infer the response of the real MOC to changes in the wind forcing from idealized models, if the corresponding, real τ_α are unknown.

CHAPTER 8

Summary and conclusions

8.1 Summary and discussion

Historically, hierarchies of idealized ocean models and solutions of different complexity have been developed to investigate the dynamics of the basin-scale, deep, meridional overturning circulation (MOC). The most dynamically-reduced solutions at the base of the hierarchy are those for the thermohaline circulation (THC), which are forced by a surface buoyancy flux only, whereas slightly more complex solutions also include zonal wind forcing τ^x. In this manuscript, we explore unresolved aspects of these two kinds of solutions and, more specifically, the dynamical linkage of the tropical thermocline thickness H_s and the sinking branch of the MOC.

We use two types of models, a variable-density, 2-layer ocean model (VLOM) and an ocean general circulation model (MITgcm), the former allowing for analytic solutions and the latter for a more accurate representation of processes. For both models, solutions are obtained first without and then with wind forcing in an idealized, flat-bottom basin on the northern hemisphere. In almost all solutions, the thermocline thickness H_s (or the vertical temperature profile $\tilde{T}$) are prescribed in a sponge layer along the southern boundary. For simplicity, density depends only on temperature, and the solutions are forced by a surface heat flux Q, which quickly relaxes near-surface temperature to a prescribed $T^*(y)$. The temperature $T^*(y)$ linearly decreases from T_s to T_n (density increases from ρ_s to ρ_n) in a region $y_1 = 30°\text{N} \leq y \leq y_2 = 50°\text{N}$ (see middle panel in Fig. 3). In solutions with winds,

the idealized forcing function consists of cosine-shaped westerlies driving a subtropical and a subpolar gyre. The westerlies reach a maximum τ_o at the latitude $y_W = 35°$N (see right panel in Fig. 3), which also marks the boundary between the two gyres.

Constant-density, layer-model solutions without wind forcing (*e.g.,* Stommel and Arons, 1960; Kawase, 1987; Johnson and Marshall, 2002, 2004; Pedlosky and Spall, 2005) and with wind forcing (*e.g.,* Ireley and Young, 1983; Luyten and Stommel, 1986; Huang, 1986; Huang and Flierl, 1987; Nonaka et al., 2006) have contributed to the understanding of the MOC in previous, similar studies. The VLOM solutions presented in this manuscript extend these solutions, as the surface-layer density varies horizontally. In particular, that allows for the model to be forced by a surface buoyancy flux, which is parameterized as a detrainment or entrainment velocity in some of the previous studies (*e.g.*, Luyten and Stommel, 1986; Pedlosky and Spall, 2005). Furthermore, it allows for a better understanding of the impact of the large-scale, surface-density gradient on wave-adjustment processes. Novel aspects discussed in this manuscript include:

- The consequences of the eastern-boundary density structure (47) on MOC solutions.
- A dynamical justification of the relation between the meridional pressure difference and the strength of the MOC (Eq. 1), and the role of horizontal mixing.
- The relations of the strength of deep-water formation $\mathcal{M}_n$ and the deep-water export $\mathcal{M}$ to the tropical thermocline thickness H_s and the strength of the westerlies τ_o.
- The baroclinic, Rossby-wave speed in VLOM, taking into account the effects of wind-driven circulation and the surface-layer density gradient (Eq. 27).

Results are discussed in more detail below.

Without wind forcing and mixing, VLOM adjusts to a steady state without an MOC (Chapter 3.2). Initially, Q generates a meridional density gradient in the surface layer, that drives an eastward flow. At the eastern boundary, Kelvin waves cancel that flow by adjusting the layer thickness to h_e (Eq. 47), so that the meridional, depth-integrated, upper-layer pressure gradient is canceled out. As a result, the upper layer thickens towards the pole, and eventually extends to the bottom slightly south of y_2. Subsequently, Rossby waves propagate

the eastern-boundary density structure across the basin, adjusting VLOM to a steady state with no zonal pressure gradient. Interestingly, the Rossby-wave speed (27) has an westward component proportional to the poleward, surface density gradient, which ensures that this adjustment is completed within finite time. Subsequently, the depth-integrated layer flow, the diapycnal flow, and the surface buoyancy flux all vanish. This response differs from solutions in idealized, isopycnal layer models (*e.g.*, Pedlosky and Spall, 2005), where surface cooling is implemented as a detrainment velocity (compare Section 1.1.4), and hence models always adjust to a state with an MOC. A possible explanation for this discrepancy is, that the detrainment velocity in the isopycnal models simulates additional processes, that are not directly related to the surface heat flux (As discussed below, a similar MOC develops in VLOM when a detrainment velocity w_d is included, which is related to horizontal mixing and advection.).

Although VLOM solutions are obtained for depth-integrated layer variables, they can be extended to include a thermal-wind-shear circulation in the upper layer (Chapter 3.4). In the no-MOC solutions, the thermal-wind shear is directed zonally in the region with a meridional, surface-temperature gradient, with eastward velocities near the surface and westward velocities at the bottom of the layer (compare Fig. 8). It follows, that water has to sink at the eastern and upwell at the western boundary to close the circulation, which is assumed to occur isothermally in thin boundary layers. In a similar solution for a conceptual OGCM (Chapter 4.1), that sinking and upwelling occurs in meridional Ekman layers. As the flow has a meridional component within these Ekman layers, meridional advection affects the density field and can potentially destabilize the solutions. On the other hand, the meridional flow (and hence the advection term) is proportional to the horizontal viscosity ν_h. As a result, the no-MOC state appears to be stable in the limit $\nu_h \to 0$ at the eastern boundary, where meridional advection is also counteracted by vertical advection. Furthermore, the eastern-boundary density field adjusts to a state similar to that in the no-MOC solution (Sumata and Kubokawa, 2001, and Eq. 40 in the present manuscript) even in the numerical MITgcm solutions with finite mixing parameters (compare Figs. 12 and 28).

When the models include finite mixing terms, they adjust to steady states *with* an MOC (Chapters 3.3 and 4.2). In VLOM, mixing is introduced as a detrainment velocity w_d,

that relaxes the upper-layer thickness to a prescribed mixing depth $h_{\max}$, when Rossby-waves attempt to deepen the layer interface any further in the interior ocean. Consequently, the interior-ocean solution changes only in a northern boundary layer, where the eastern-boundary layer thickness h_e exceeds $h_{\max}$. In this boundary layer, the Rossby-wave damping causes the upper layer to shoal away from the eastern-boundary, and the resulting pressure gradient drives a northeastward, upper-layer flow that converges towards y_2 and the northeastern corner, where most of the detrainment occurs. That flow is fed by a western boundary current, which connects the northern boundary layer with the southern sponge layer, where the circulation is closed by upwelling.

The velocity w_d in VLOM parameterizes horizontal mixing processes and advection in the MITgcm, which tend to restratify the water column (and hence to thin the upper layer) in a northern boundary layer. That boundary layer is more complex in MITgcm than in VLOM, however, and can be subdivided into an inner and an outer region (Chapter 4.3). The detrainment and downwelling occurs in the inner region right at y_2. Because thermal-wind shear exists only south of y_2 where $g'_y \neq 0$, velocities are smoothed in a zonal Ekman layer along y_2. Just south of y_2, the Ekman-layer flow has a southward component at depth. As a result, advection cools the deep ocean there, preventing the MITgcm to adjust to the no-MOC state. Furthermore, the region where the upper-layer extends to the bottom in the no-MOC state is extremely thin in the meridional direction. Consequently, that region is quickly damped away by horizontal diffusion away from the eastern boundary, where h_1 is adjusted by slow Rossby waves. The stratification generated by these two processes, and the pressure gradient and flow associated with it then serve as boundary condition for the outer region, which reveals some key properties of a zonal Munk layer: It has a cusp at the eastern boundary, and widens to the west according to the Munk-layer width scale $L_M \sim [\nu_h/\beta(x_e - x)]^{1/4}$. Furthermore, the detrainment within the outer region is small, and its role in the MOC is merely to channel water into the inner region of the boundary layer.

The strength of the MOC is measured by $\mathcal{M}_n$, the convergence of upper-layer water into the northern boundary layer, in both models. In VLOM, the flow convergence (61) can be calculated exactly. It is closely related to the MOC scaling for OGCMs (1), where $\mathcal{M}_n$ is proportional to the meridional, baroclinic pressure gradient. Furthermore, $\mathcal{M}_n$ depends on

the strength of Rossby-wave damping via the parameter $C_{\max}(h_{\max})$. In the MITgcm, where $\mathcal{M}_n$ is measured by the absolute maximum of the streamfunction $\psi^T(y,T)$, it increases with the thermocline thickness H_s in a set of experiments where all other parameters remain constant. On the other hand, $\mathcal{M}_n$ does not exactly follow curves proportional to H_s^2, *i.e.*, VLOM results with constant $C_{\max}$ (compare Fig. 9), as would be suggested by the MOC scaling (1) with a constant parameter C. A better correspondence between MITgcm and VLOM results can be obtained by keeping the northern-boundary-layer width constant in VLOM, as it is in MITgcm, where the width of the boundary layer is proportional to L_M. The mixing depth $h_{\max}$ is then given by (65) and increases linearly with H_s, and hence the strength of Rossby-wave damping and the parameter $C_{\max}$ are inversely proportional to the eastern-boundary thermocline depth. That the strength of the MOC depends on the horizontal viscosity (and eddy mixing in general) is potentially problematic with regard to simulating the real MOC in coarse resolution models. The choice for the value of horizontal viscosity ν_h in OGCMs is often based on numerical rather than on physical considerations (*i.e.*, ν_h is chosen such that the western boundary layer is resolved by the model). Furthermore, it is known that the simple, Laplacian mixing parameterizations used in the MITgcm do not well represent eddy-mixing processes in eddy-resolving models (or the real ocean). Introducing more comprehensive mixing parameterizations (*e.g.*, Gent and McWilliams, 1990; Visbeck et al., 1997; Eden, 2011) has generally improved the representation of the effect of eddies on the large-scale flow in coarse-resolution models; it is not clear, however, how well these parameterizations perform in extreme situations, such as the northern boundary layer.

When the models are forced by buoyancy forcing Q and westerly, zonal winds τ^x, they adjust to states with an MOC, even when mixing processes are excluded in VLOM (Chapter 5). When VLOM is started, the depth-integrated circulation quickly forms a subtropical and a subpolar gyre. At the eastern boundary, Kelvin wave adjustments still maintain the coastal structure h_e, as in solutions without τ^x, and baroclinic Rossby waves begin to propagate that structure westward. As indicated by (26) and the baroclinic, Rossby-wave speed (27), however, the adjustment of the interior ocean is strongly affected by the winds. The wave speed (27) has an additional component now, which is given by the depth-averaged, geostrophic part of the Sverdrup flow, and is identical to that in isopycnal, 2-layer models

(*e.g.,* Rhines, 1986). As a result, the zonal wave speed can become eastward in regions with strong, eastward gyre flow. Furthermore in (26), the Ekman pumping velocity w_{ek} modifies the upper-layer thickness until it is arrested by the Rossby wave front, or balanced by mixed-layer entrainment (in case $h_1 = h_{\min}$, see below).

For the reasons stated above, the interior ocean is subdivided into three dynamically distinguished regions (compare Fig. 20) in steady-state solutions with $\tau^x \neq 0$. In Region A, eastern-boundary Rossby waves adjust the layer interface such that the Sverdrup flow is entirely contained in the upper layer. In the subpolar ocean, where $w_{ek} > 0$, the upper layer consequently thins along Rossby-wave characteristics, and when τ^x is sufficiently strong, h_1 can reach $h_{\min}$. In that case, mixed-layer entrainment $w_m > 0$ arrests $h_1 = h_{\min}$, and prevents further thinning in a Region B_1. Finally, in Region B_2, Rossby-wave characteristics originate from the western boundary layer, and we have argued, that $h_1 = h_{\min}$ there, as in Region B_1. In Region B, the union of Regions B_1 and B_2, the geostrophic part of the Sverdrup flow is then depth independent, and hence mostly confined to the much thicker deep layer. Similar outcropping regions have been discussed previously in isopycnal, layer models (*e.g.*, Luyten and Stommel, 1986; Huang and Flierl, 1987; Nonaka et al., 2006), and including a variable temperature in the surface layer in VLOM does not essentially alter that part of the solution. In contrast to previous solutions, however, the upper layer also outcrops along $y = y_2$. At this latitude, the upper-layer Sverdrup transport in Region A constitutes a detrainment w_c, as water crossing y_2 to the north is cooled to T_n and joins layer 2. In Region B, where the upper-layer flow is dominated by the Ekman transport on the other hand, entrainment w_m occurs along y_2 as water crosses y_2 to the south and is heated to $T^* > T_n$ in the mixed layer.

As for the case without winds, solutions are closed in a western boundary layer. Interestingly, however, western-boundary entrainment can be much stronger than in solutions without winds, essentially for two reasons: The northward convergence of upper-layer water (and hence the total, meridional upper-layer transport $\mathcal{V}_1$) tends to be stronger in solutions with winds for a given H_s, and the Ekman transport is southward. It follows, that the zonal pressure difference, which drives the northward, geostrophic part of $\mathcal{V}_1$, has to be larger in solutions with winds than without wind forcing. As the eastern-boundary pressure is determined by h_e in all solutions, the western-boundary layer thickness h_w has to be smaller in

solutions with τ^x and consequently, it is more likely that h_w has to thin further than $h_{\min}$ in oder to maintain $\mathcal{V}_1$; in that case entrainment w_m reduces $\mathcal{V}_1$ to $\tilde{\mathcal{V}}_1(y)$, the total, meridional, upper-layer transport with $h_w = h_{\min}$. Consistently, the western boundary entrainment occurs most prominently just north of the latitude y_W, which separates the two gyres and is close to where the Ekman transport is maximal.

When mixing is included in VLOM (Chapter 5.3), particular solutions can still be derived by integration along Rossby-wave characteristics. As in solutions without winds, w_d is only active in a northern boundary layer, where the undamped layer thickness exceeds the prescribed mixing thickness $h_{\max}$, and the Rossby-wave damping tends to generate (additional) upper-layer flow convergence into the boundary layer. Because the wind forcing affects the Rossby-wave adjustment, however, characteristics are no longer zonal as in the case without winds, and a general, analytical solution within the boundary layer cannot be found. To explore the effect of the northern boundary layer on the large-scale MOC, the northern boundary layer is therefore included in an approximate way, which allows for a simple and general calculation of upper-layer flow convergence.

MITgcm solutions with buoyancy forcing and zonal winds (Chapter 6) also have Regions A and B, very similar as those in VLOM solutions. Furthermore, there is also a region near $y_2 = 50°$N, where mixing tends to raise isotherms, as in the northern boundary layer in the solution without winds. A difference to the VLOM solutions outside the northern boundary layer, however, is that diffusion tends to deepen the upper-layer away from the eastern boundary in MITgcm solutions relative to their VLOM counterparts. As a result, Region B tends to be (slightly) smaller, because its eastern boundary $\hat{x}$, where h_1 reaches $h_{\min}$ first, is shifted to the west in MITgcm.

Because the eastern boundary structure is the same in solutions with and without winds the eastern-boundary sinking W_e (63) is the same in all solutions. Almost all deep sinking occurs at the eastern boundary near y_2, although some weaker sinking also occurs in the northern boundary layer. This is in agreement with the results of (*e.g.*, Spall and Pickart, 2001), who argued that the interior sinking has to be relatively small, because it follows from the Sverdrup relation ($fw = \beta V$) that interior sinking is small compared to the horizontal transports. Furthermore, they found that the eastern boundary sinking is a good

measure for the strength of the MOC, when measured as the absolute maximum of $\psi(y, z)$. Interestingly, the latter is not the case in the solutions presented within this manuscript. As we have shown, the eastern-boundary sinking only depends on the eastern-boundary structure h_e, whereas the strength of the (diapycnal) MOC also depends on interior-ocean processes. As a consequence, the eastern-boundary sinking for a given H_s does not even change in the solutions without an MOC, where the eastern sinking is exactly balanced by western-boundary upwelling at the same latitude. In more "realistic" solutions, on the other hand, where the eastern- and northern-boundary temperatures are affected (increased) by advection, so that h_e is shifted to the north, the sinking at these boundaries cannot be balanced by upwelling at the same latitude. Consequently, W_e must then also contribute to the overturning $\psi(y, z)$, although it is not clear how that is related to the diapycnal MOC. Hence, the fact that we do not find W_e to be a good measure for the MOC does not really contradict the results of Spall and Pickart (2001), but merely reflects that different measures for its strength are used. It does raise the question, however, how valuable as a metric the strength of the MOC really is. Regarding the issue of interior vs. eastern-boundary sinking, the relation of eastern-boundary sinking and h_e further suggests that interior sinking may be important in general, albeit being small in the solutions discussed above. Consider a solution with $T^*(x, y)$, where the coldest region is confined to the interior ocean, and hence the upper layer does not extend to the bottom at the eastern and northern boundaries [$\max(h_e) < D$]. As the eastern-boundary sinking only extends to the bottom of the upper layer, it follows that all sinking to larger depths must then occur in the interior ocean. Such solutions have not been considered in this manuscript, however, and this process will be explored in more detail in future studies.

To characterize (VLOM) solutions, we have introduced the nondimensional parameters γ_α, ($\alpha = a, b, c$), which indicate whether entrainment occurs in the western-boundary layer (γ_a), a Region B exists in the subpolar gyre (γ_b), and whether Region B extends towards the northern, homogenous part of the ocean (γ_c). These processes also have consequences for the strength and structure of the MOC, which is measured by $\mathcal{M}_n$ and $\mathcal{M}$. The former represents the total detrainment in the northern boundary layer and across y_2, and hence the deep-water formation rate, whereas the latter measures the deep-water export from the

subpolar ocean.

The strength of $\mathcal{M}_n$ in VLOM depends on whether Region B extends to y_2 or not. If it does not ($\gamma_c \leq 1$), water detrains across the entire width of the basin, and the total detrainment by the velocity w_c, $\mathcal{W}_c$, is given by the integrated Sverdrup transport across y_2. Because $\mathcal{W}_c$ does not depend on H_s in that case, $\mathcal{M}_n$ is only sensitive to the thermocline thickness when a northern boundary layer is included in the solution ($w_d \neq 0$). As in the solution without winds, w_d decreases the upper-layer thickness to $h_1 = h_{\max}$ in a latitude band $y''_w \leq y \leq y_2$ just east of the western boundary, and the modified, meridional pressure gradient than drives an eastward flow. This additional convergence and detrainment, $\mathcal{W}_d$ (115), also takes a similar form as in the solutions without winds. When Region B extends to y_2 ($\gamma_c \geq 1$), on the other hand, $\mathcal{M}_n$ is completely insensitive to the mixing w_d. As $h_1 = h_{\min}$ in Region B in between the western and northern boundary layers, Rossby-wave damping by w_d cannot further thin the upper-layer near western boundary layer. Hence the convergence of upper layer flow near y_2 remains unchanged. Furthermore, detrainment w_c occurs along y_2 only to the east of $\hat{x}(y_2)$ in case $\gamma_c \geq 1$, and $\mathcal{M}_n$ is then given by (113b). Interestingly, (113b) is proportional to the eastern-boundary pressure, and has a similar form as the MOC scaling (1). Furthermore, the constant C_τ in (113b), depends on the geometry of the wind forcing τ^x, but not its amplitude τ_o. The dynamical explanation for this similarity to the scaling is, that $\mathcal{M}_n$ is given by the Sverdrup transport/width times the distance of $\hat{x}(y_2)$ to the eastern boundary, and that this distance linearly depends on the eastern boundary pressure, but is inversely proportional to the strength of the winds (compare Eqn. 89).

In solutions without a Region B ($\gamma_b \leq 1$), and without strong, western-boundary entrainment near the gyre boundary y_W ($\gamma_a \leq 1$), the deep-water export and formation rate are (almost) the same, $\mathcal{M} \approx \mathcal{M}_n$ in VLOM (compare Eq. 120). Because the deep-water export is the sum of all detrainment and entrainment processes in subpolar ocean, however, $\mathcal{M}$ is reduced by the entrainment in the interior, subpolar ocean, $\mathcal{W}_{in}$, in solutions with a Region B ($\gamma_b > 1$). Furthermore, when western-boundary entrainment occurs at y_W, the deep-water export is given by the local, maximal, meridional, upper-layer transport that can be maintained by the model, $\mathcal{M} = \tilde{\mathcal{V}}_1(y_W)$, and hence the deep-water export is essentially decoupled from its formation rate. As $\tilde{\mathcal{V}}_1(y_W)$ is inversely proportional to the strength

of the winds τ_o, an interesting consequence of the decoupling is, that $\mathcal{M}$ is then inversely proportional to τ_o, even when $\mathcal{M}$ increases with τ_o (in case $\gamma_c < 1$).

In the MITgcm, $\mathcal{M}$ is the absolute maximum of $\psi^T(y,T)$, as in the solutions without winds, and $\mathcal{M}$ is defined as the maximum of $\psi^T(y_W,T)$, at the gyre boundary. Both measures for the strength of the MOC are generally in fair agreement with the VLOM results. In particular, $\mathcal{M}$ in MITgcm is also inversely proportional to τ_o, when the prescribed H_s is small, and proportional to τ_o for larger H_s. Furthermore, the model results show the best correspondence in the strength of the MOC, when results do not depend (much) on mixing, that is when $\gamma_c > 1$ for $\mathcal{M}_n$ and $\gamma_a > 1$ for $\mathcal{M}$. As results depend on mixing otherwise, however, differences in the strength of the MOC can then be explained by the fact, that our 2-layer version of VLOM is too simple to precisely simulate the effect mixing processes in the MITgcm.

The results for the VLOM response to buoyancy forcing and zonal winds with a prescribed, tropical, upper-layer thickness H_s (Chapter 5) are (among other things) useful to explore the response in a more realistic system, where H_s is internally determined by model processes. For that purpose, VLOM is merged with the Gnanadesikan (1999) model in Chapter 7. In that model hybrid, the deep-water export from the subpolar ocean, $\mathcal{M}(H_s)$, is given by the VLOM result (120). The layer thickness H_s adjusts, however, such that $\mathcal{M}(H_s)$ is balanced by entrainment transports outside the subpolar North Atlantic, which depend on H_s as in the Gnanadesikan (1999) model.

Three solutions, each with a different set of entrainment and detrainment transports outside the subpolar North Atlantic, are discussed in Chapter 7. The results illustrate that the qualitative response to the westerly winds importantly depends on whether the γ_α, $(\alpha = a, b, c)$, are smaller or larger than one. Independent of the setting outside the subpolar gyre, the strength of the MOC $\mathcal{M}$ is proportional, and H_s is inversely proportional to the strength of the westerlies τ_o, when all $\gamma_\alpha < 1$. When $\gamma_\alpha > 1$, on the other hand, the response is opposite, that is $\mathcal{M}$ decreases, and H_s increases with an increasing τ_o. For all solutions exist different sets of critical τ_α (the τ_o for which $\gamma_\alpha = 1$, respectively), and their values vary strongly with the different parameterizations of the upwelling branch. These findings suggest, that it might be difficult to infer the response of the (real) MOC to changes in the

wind forcing from idealized models, when the corresponding τ_α are not known. On the other hand, simple models, as that in Chapter 7, may provide a useful metric to understand, and to gain confidence into the response in more complex, or even realistic models.

8.2 Conclusions and outlook

In conclusion, we have obtained and analyzed MOC solutions forced by a buoyancy flux and zonal wind stress. These solutions, together with those obtained in previous studies, can be arranged into a hierarchy of solutions with increasing complexity with regard to the physical mechanisms that generate detrainment and flow convergence into the North Atlantic (compare Figure 34). At the bottom of the hierarchy are solutions where the detrainment is prescribed as a mass flux near the western boundary (*e.g.*, Stommel and Arons, 1960; Kawase, 1987; Johnson and Marshall, 2002, 2004, left panels of Figure 34). In more sophisticated models, the detrainment occurs in regions with Rossby wave damping, and its strength is internally determined by model processes (*e.g.*, Pedlosky and Spall, 2005; Nonaka et al., 2006, solutions in Chapter 3, middle panels of Figure 34). As a precondition for the Rossby-wave damping in the solutions in Chapter 3, coastal processes thicken the upper layer along the eastern-boundary in response to the poleward, surface-density gradient. When Rossby waves propagate this eastern-boundary density structure across the basin, horizontal mixing processes and advection effectively thin the upper layer in a narrow, northern region, where the upper-layer is extremely thick at the eastern boundary. When westerly winds are included in that model, water converges into the regions where it is transformed to deep water with the northward, subpolar-gyre flow (solutions in Chapter 5, right panel). Because of the barotropic circulation, the deep limb no longer mirrors the upper branch of the MOC, *i.e.*, the southward flow in the deep branch is confined to the western boundary current, whereas the upper branch separates from the western boundary in the southern part of the subpolar gyre.

Interestingly, the strength of the MOC is proportional to the meridional pressure difference in the two more complex kinds of solutions (middle and right panels in Figure 34), as it has been previously reported in idealized OGCM solutions (*e.g.*, Bryan, 1987; Marotzke,

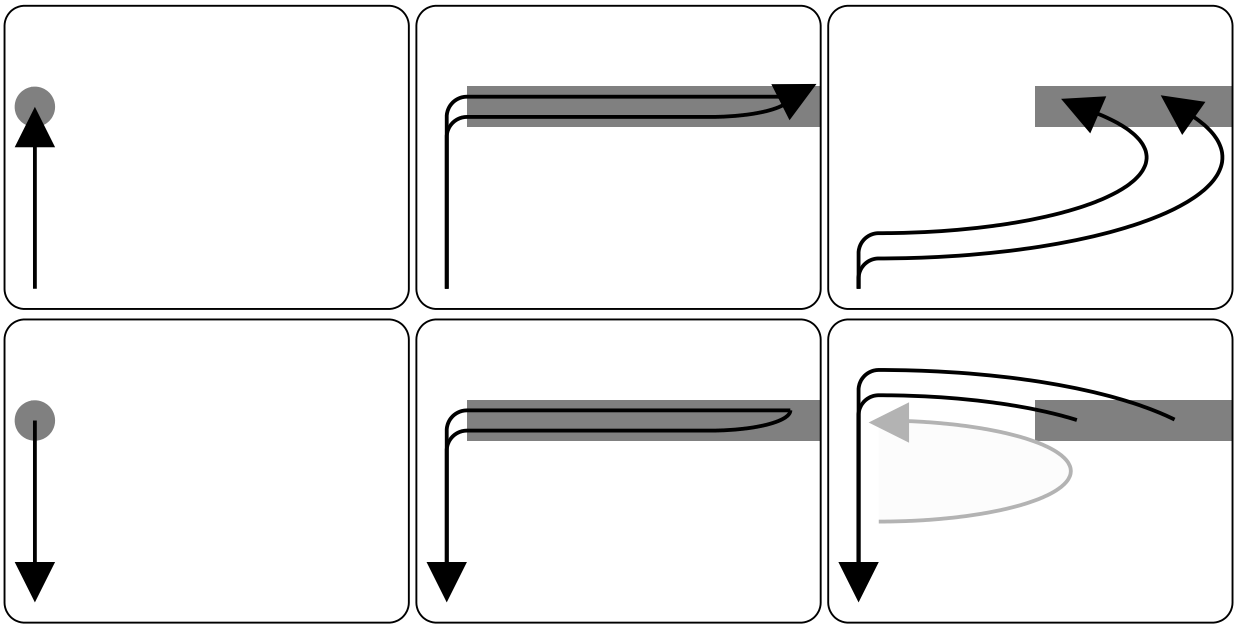

Figure 34: Schematics of the horizontal circulation in the upper (upper panels) and lower layers (lower panels) in a hierarchy of 2-layer model solutions, focussing on detrainment processes in the subpolar ocean. In the simplest solutions (left panels) detrainment is prescribed as a mass source near the western boundary (*e.g.*, Stommel and Arons, 1960; Kawase, 1987). The middle panels represent solutions with detrainment in a northern boundary layer (*e.g.*, Pedlosky and Spall, 2005, solutions in Chapter 3), and right panels show solutions with winds, where northward, upper-layer flow convergence occurs in the subpolar-gyre (Chapter 5). Black arrows indicate the main pathways of the flow, grey shapes the regions where water is transfered from the upper to the deep layer, and the light grey arrow in the lower right panel indicates a recirculation in the deep, subpolar gyre.

1997; Park and Bryan, 2000). Moreover, the strength of the MOC is related to the detrainment processes in each model, that is the strength of Rossby-wave damping in solutions with a northern boundary layer, and the subpolar gyre circulation in the case with winds.

All solutions discussed in this manuscript are highly idealized, and the hierarchy of solutions illustrated in Figure 34 is far from being complete. It will be interesting to explore how the results hold up in more complex physical situations. Given the dynamical importance of the eastern-boundary density structure in all solutions, considering the impact of continental slopes on the coastal adjustment may be a consequential next step to extend the hierarchy.

References

Bender, C. M. and S. A. Orszag, 1978: *Advanced Mathematical Methods for Scientists and Engineers*. McGraw-Hill.

Bryan, F., 1986: High-latitude salinity effects and interhemispheric thermohaline circulations. *Nature*, **323**, 301–304.

Bryan, F., 1987: On the parameter sensitivity of primitive equation ocean general circulation models. *J. Phys. Oceanogr.*, **17**, 970–985.

Bryan, K., 1984: Accelerating the convergence to equilibrium of ocean-climate models. *J. Phys. Oceanogr.*, **14**, 666–673.

Bryan, K., 1991: Poleward heat transport in the ocean: a review of a hierarchy of models with increasing resolution. *Tellus*, **43AB**, 104 – 115.

Bryan, K. and M. D. Cox, 1967: A numerical investigation of the oceanic general circulation. *Tellus*, **19**, 54–80.

Bryan, K. and M. D. Cox, 1968: A nonlinear model of an ocean driven by winds and differiential heating: Part I. Description of the three-dimensional velocity and density field. *J. Atmos. Sci.*

Cessi, P. and C. L. Wolfe, 2009: Eddy-driven buoyancy gradients on eastern boundaries and their role in the thermocline. *J. Phys. Oceanogr.*, **39**, 1596 – 1614.

Colin de Verdière, A., 1988: Buoyancy driven planetary flows. *J. Mar. Res.*, **46**, 215–265.

Colin de Verdière, A., 1989: On the interaction of wind and buoyancy driven gyres. *J. Mar. Res.*, **47**, 595 – 633.

Cox, M. D., 1987: Isopycnal diffusion in a z-coordinate ocean model. *Ocean Modelling*, **74**, 1–5.

Curry, R. and C. Mauritzen, 2005: Dilution of the northern North Atlantic ocean in recent decades. *Science*, **308**, 1772 – 1774.

Eden, C., 2011: A closure for meso-scale eddy fluxes based on linear instability theory. *Ocean Modelling*, in press.

Ganachaud, A. and C. Wunsch, 2000: Improved estimates of global ocean circulation, heat transport and mixing from hydrographic data. *Nature*, **408**, 453–456.

Gargett, A. E., 1984: Vertical eddy diffusivity in the ocean interior. *J. Mar. Res.*, **42**, 359–393.

Gargett, A. E. and G. Holloway, 1984: Dissipation and diffusion by internal wave breaking. *J. Mar. Res.*, **42**, 15–27.

Gent, P. R. and J. C. McWilliams, 1990: Isopycnal mixing in ocean general circulation models. *J. Phys. Oceanogr.*, **20**, 150–155.

Gill, A. E., 1982: *Atmosphere-Ocean Dynamics*. Academic Press, San Diego, 662 pp.

Gnanadesikan, A., 1999: A simple predictive model for the structure of the oceanic pycnocline. *Science*, **283**, 2077–2079.

Greatbatch, R. and J. Lu, 2003: Reconciling the Stommel box model with the Stommel-Arons model: A possible role for southern hemisphere wind forcing? *J. Phys. Oceanogr.*, **33**, 1618–1632.

Hall, M. M. and H. L. Bryden, 1982: Direct estimates and mechanisms of ocean heat transport. *Deep-Sea Res. Part A.*, **29**, 339 – 359.

Hasselmann, K., 1982: An ocean model for climate variability studies. *Progress in Oceanography*, **11**, 69–92.

Held, I. M., 2005: The gap between simulation and understanding in climate modeling. *BAMS*, 1609 – 1614.

Hill, C. and J. Marshall, 1995: Application of a parallel Navier-Stokes model to ocean circulation in parallel computational fluid dynamics. *In Proceedings of Parallel Computational Fluid Dynamics: Implementations and Results Using Parallel Computers*, 545 – 552.

Huang, R. X., 1986: Numerical simulation of a wind-driven circulation in a subtropical/subpolar basin. *J. Phys. Oceanogr.*, **16**, 1636 – 1650.

Huang, R. X., M. A. Cane, N. Naik, and P. Goodman, 2000: Global adjustment of the thermocline in response to deepwater formation. *Geophys. Res. Lett.*, **27**, 759–762.

Huang, R. X. and G. R. Flierl, 1987: Two-layer models for the thermocline and current structure in subtropical/subpolar gyres. *J. Phys. Oceanogr.*, **17**, 872 – 884.

Ireley, G. R. and W. R. Young, 1983: Can the western boundary layer affect the potential vorticity distribution in the Sverdrup interior of a wind gyre. *J. Phys. Oceanogr.*, **13**, 1753–1763.

Jensen, T. G., 1998: Description of a thermodynamic ocean modelling system (toms). Technical report: Atmospheric science paper, Colorado State University, Fort Collins.

Johnson, H. L. and D. P. Marshall, 2002: A theory for the surface Atlantic response to thermohaline variability. *J. Phys. Oceanogr.*, **32**, 1121–1132.

Johnson, H. L. and D. P. Marshall, 2004: Global teleconnections of meridional overturning circulation anomalies. *J. Phys. Oceanogr.*, **34**, 1702–1722.

Kawase, M., 1987: Establishment of deep ocean circulation driven by deep water production. *J. Phys. Oceanogr.*, **17**, 2294–2317.

Klinger, B. A., S. Drijfhout, J. Marotzke, and J. R. Scott, 2004: Remote wind-driven overturning in the absence of the Drake Passage effect. *J. Phys. Oceanogr.*, **34**, 1036–1049.

Kuhlbrodt, T., A. Griesel, M. Montoya, A. Levermann, M. Hofmann, and S. Rahmstorf, 2007: On the driving processes of the Atlantic meridional overturning circulation. *Rev. Geophys.*, **45**.

Luyten, J. R., J. Pedlosky, and H. Stommel, 1983: The ventilated thermocline. *J. Phys. Oceanogr.*, **13**, 292–309.

Luyten, J. R. and H. Stommel, 1986: Gyres driven by combined wind and buoyancy flux. *J. Phys. Oceanogr.*, **16**, 1551–1560.

Maier-Reimer, E. and K. Hasselmann, 1987: Transport and storage of CO_2 in the ocean: An inorganic ocean-circulation carbon cycle model. *Climate Dyn.*, **2**, 63–90.

Maier-Reimer, E., U. Mikolajewicz, and K. Hasselmann, 1993: Mean circulation of the Hamburg LSG OGCM and its sensitivity to the thermohaline surface forcing. *J. Phys. Oceanogr.*, **23**, 731–757.

Marotzke, J., 1997: Boundary mixing and the dynamics of three-dimensional thermohaline circulations. *J. Phys. Oceanogr.*, **27**, 1713–1728.

Marotzke, J., P. Welander, and J. Willebrand, 1988: Instability and multiple equilibria in a meridional-plane model of the thermohaline circulation. *Tellus*, **40A**, 162 – 172.

Marotzke, J. and J. Willebrand, 1991: Multiple equilibria of the global thermohaline circulation. *J. Phys. Oceanogr.*, **21**, 1372 – 1385.

Marshall, J., A. Adcroft, C. Hill, L. Perelman, and C. Heisey, 1997: A finite-volume, incompressible Navier Stokes model for studies of the ocean on parallel computers. *J. Geophysical Res.*, 5753–5766.

McCreary, J. P. and P. Lu, 1994: Interaction between the subtropical and the equatorial ocean circulations: The subtropical cell. *J. Phys. Oceanogr.*, **24**, 466–497.

McDermott, D. A., 1996: The regulation of northern overturning by southern hemisphere winds. *J. Phys. Oceanogr.*, **26**, 1234–1255.

McManus, J. F., R. Francois, J. M. Gherardi, L. D. Keigwin, and S. Brown-Leger, 2004: Collapse and rapid resumption of Atlantic meridional circulation linked to deglacial climate changes. *Nature*, **428**, 834–837.

Munk, W. H., 1950: On the wind-driven ocean circulation. *J. Meteor.*, **7 (2)**, 79 – 93.

Nakano, H. and N. Suginohara, 2002: Effects of bottom boundary layer parameterization on reproducing deep and bottom waters in a world ocean model. *J. Phys. Oceanogr.*, **32**, 1209–1227.

Nilsson, J., G. Broström, and G. Walin, 2003: The thermohaline circulation and vertical mixing: Does weaker density stratification give stronger overturning? *J. Phys. Oceanogr.*, **33**, 2781–2795.

Nonaka, M., J. P. McCreary, and S.-P. Xie, 2006: Influence of midlatitude winds on the stratification of the equatorial thermocline. *J. Phys. Oceanogr.*, **36**, 222–237.

Okazaki, Y., A. Timmermann, L. Menviel, N. Harada, A. Abe-Ouchi, M. O. Chikamoto, A. Mouchet, and H. Asahi, 2010: Deepwater formation in the North Pacific during the last glacial termination. *Science*, **329**, 200 – 204.

Park, Y.-G., 2006: Dependence of an eastern boundary current on the horizontal resolution in thermally driven circulations. *J. Geophysical Res.*, **111 (C09005)**.

Park, Y.-G. and K. Bryan, 2000: Comparison of thermally driven circulations from a depth coordinate model and an isopycnal model, Part I: A scaling law and sensitivity to vertical diffusivity. *J. Phys. Oceanogr.*, **30**, 590–605.

Pedlosky, J. and M. A. Spall, 2005: Boundary intensification of vertical velocity in a β-plane basin. *J. Phys. Oceanogr.*, **35**, 2487–2500.

Polzin, K. L., J. M. Toole, and R. W. Schmitt, 1995: Finescale parameterizations of turbulent dissipation. *J. Phys. Oceanogr.*, **25**, 306–328.

Radko, T. and J. Marshall, 2010: The leaky thermocline. *J. Phys. Oceanogr.*, **34**, 1648 – 1662.

Rahmstorf, S., 1996: On the freshwater forcing and transport of the Atlantic thermohaline circulation. *Clim. Dyn.*, **12**, 799–811.

Redi, M. H., 1982: Oceanic isopycnal mixing by coordinate rotation. *J. Phys. Oceanogr.*, **12**, 1154–1158.

Rhines, P. B., 1986: Vorticity dynamics of the ocean general circulation. *Ann. Rev. Fluid Mech.*, **18**, 433–497.

Rhines, P. B. and W. R. Young, 1982: Homogenization of potential vorticity in planetary gyres. *J. Fluid Mech.*, **122**, 347–367.

Robinson, A. and H. Stommel, 1959: The oceanic thermocline and the associated thermohaline circulation. *Tellus*, **11**, 295 – 308.

Rooth, C., 1982: Hydrology and ocean circulation. *Progress in Oceanography*, **11**, 131–149.

Ru, H., 2000: A $2\frac{1}{2}$ dimensional thermohaline circulation model with boundary mixing. M.S. thesis, Massachusetts Institute of Technology and Woods Hole Oceanographic Institution.

Samelson, R. M. and G. K. Vallis, 1997: Large-scale circulation with small diapycnal diffusion: The two-thermocline limit. *J. Mar. Res.*, **55**, 223–275.

Schloesser, F., R. Furue, J. P. McCreary, and A. Timmermann, 2011: Dynamics of the Atlantic meridional overturning circulation. Part 1: buoyancy-forced response. *Progress in Oceanography, submitted*.

Scott, J. R., J. Marotzke, and P. H. Stone, 1999: Interhemispheric thermohaline circulation in a coupled box model. *J. Phys. Oceanogr.*, **29**, 351–365.

Spall, M. A. and R. S. Pickart, 2001: Where does dense water sink? a subpolar gyre example. *J. Phys. Oceanogr.*, **31**, 810–826.

Stommel, H., 1948: The westward intensification of wind-driven ocean currents. *Am. Geophys. Union Trans.*, **29**, 202 – 206.

Stommel, H. and A. B. Arons, 1960: On the abyssal circulation of the world ocean—I. Stationary planetary flow pattern on a sphere. *Deep-Sea Res.*, **6**, 140–154.

Stommel, H. M., 1961: Thermohaline convection with two stable regimes of flow. *Tellus*, **13**, 224–230.

Straub, D. N., 1996: An inconsistency in between two classical models of the ocean buoyancy driven circulation. *Tellus*, **48A**, 477 – 481.

Suginohara, N. and S. Aoki, 1991: Buoyancy-driven circulation as horizontal convection on β plane. *J. Mar. Res.*, **49**, 295–320.

Sumata, H. and A. Kubokawa, 2001: Numerical study of eastern boundary ventilation and its effects on the thermocline structure. *J. Phys. Oceanogr.*, **31**, 3002–3019.

Sverdrup, H. U., 1947: Wind-driven currents in a baroclinic ocean; with application to the equatorial currents of the eastern Pacific. *Proc. Nat. Acad. Sci., Wash.*, **33**, 318 – 326.

Toggweiler, J. R. and B. Samuels, 1995: Effect of Drake Passage on the global thermohaline circulation. *Deep-Sea Res.*, **42**, 477–500.

Trenberth, K. E. and J. M. Caron, 2001: Estimates of meridional atmosphere and ocean heat transports. *J. Clim.*, **14**, 3433 – 3443.

Tsujino, H. and N. Suginohara, 1999: Thermohaline circulation enhanced by wind forcing. *J. Phys. Oceanogr.*, **29**, 1506–1516.

Vallis, G. K., 2006: *Atmospheric and Oceanic Fluid Dynamics*. Cambridge University Press, 745 pp.

Visbeck, M., J. Marshall, T. Haine, and M. A. Spall, 1997: Specification of eddy transfer coefficients in coarse-resolution ocean circulation models. *J. Phys. Oceanogr*, **27**, 381 – 402.

Welander, P., 1986: Thermohaline effects in the ocean circulation and related simple models. *Large-scale transport processes in the oceans and atmosphere*, J. Willebrand and D. L. T. Anderson, Eds., D. Reidel Publishing Company, 163–200.

Winton, 1996: The role of horizontal boundaries in parameter sensitivity and decadal-scale variability of coarse-resolution ocean general circulation models. *J. Phys. Oceanogr.*, **26**, 289–304.

Wright, D. G. and T. F. Stocker, 1991: A zonally averaged model for the thermhaline circulation. Part I: Model development and flow dynamics. *J. Phys. Oceanogr.*, **21**, 1713 – 1724.

Wright, D. G., T. F. Stocker, and D. Mercer, 1998: Closures used in zonally averaged ocean models. *J. Phys. Oceanogr.*, **28**, 791–804.

Wright, D. G., C. B. Vreugdenhil, and T. M. Hughes, 1995: Vorticity dynamics and zonally averaged ocean circulation models. *J. Phys. Oceanogr.*, **25**, 2141–2154.

Wyrtki, K., 1961: The thermohaline circulation in relation to general circulation in the oceans. *Deep-Sea Res.*, **8**, 39–64.

Zhang, J., R. W. Schmitt, and R. X. Huang, 1999: The relative influence of diapycnal mixing and hydrological forcing on the stability of the thermohaline circulation. *J. Phys. Oceanogr.*, **29**, 1096–1108.